AD-A053 185 PENNSYLVANIA STATE UNIV UNIVERSITY PARK DEPT OF ENGI--ETC F/G 13/13
SHOCK ANALYSIS OF TUBULAR VISCOPLASTIC BEAMS.(U)
JUL 77 S G GATCHEL, V H NEUBERT N00014-75-C-0759

UNCLASSIFIED NL

1 OF 2
AD
A053185

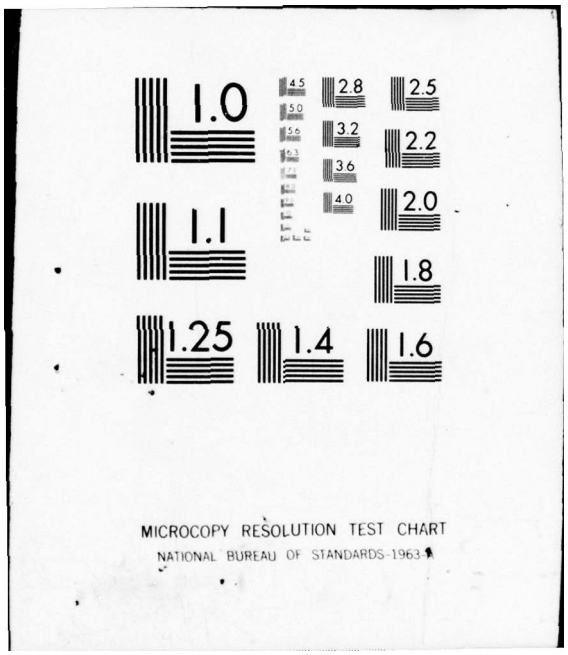
1.0
4.5
5.0
5.6
6.3
2.8
3.2
3.6
4.0
2.5
2.2
2.0
1.8
1.1
1.25
1.4
1.6
MICROCOPY RESOLUTION TEST CHART
NATIONAL BUREAU OF STANDARDS-1963-A

Report N00014-75-C-0759. Report No. 2 (Final Report)

SHOCK ANALYSIS OF TUBULAR VISCOPLASTIC BEAMS

Stanley G. Gatchel and V. H. Neubert
Department of Engineering Science and Mechanics
The Pennsylvania State University
University Park, PA 16802

July 1977

Report for Period 1 January 1976 - 31 December 1976
Contract No. N00014-75-C-0759

Qualified requestors may obtain copies of this report from DDC.

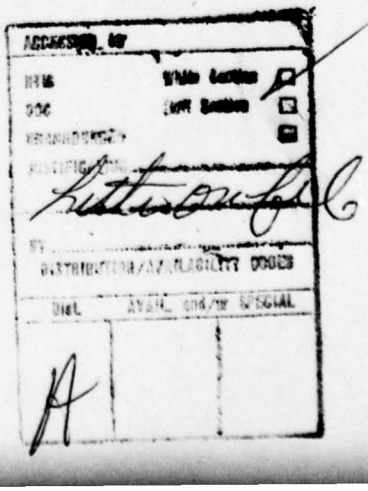

Prepared for

Naval Research Laboratory
Washington, D.C. 20375

Unclassified

SECURITY CLASSIFICATION OF THIS PAGE (When Data Entered)

REPORT DOCUMENTATION PAGE

READ INSTRUCTIONS BEFORE COMPLETING FORM

1. REPORT NUMBER: ~~N00014-75-C-0759~~ Report No. 2 ~~(Final Report)~~
2. GOVT ACCESSION NO.
3. RECIPIENT'S CATALOG NUMBER: Rept. no. 2
4. TITLE (and Subtitle): Shock Analysis of Tubular Viscoplastic Beams
5. TYPE OF REPORT & PERIOD COVERED: Final, 1 Jan [illegible]-31 Dec 1976
6. PERFORMING ORG. REPORT NUMBER
7. AUTHOR(s): Stanley G. Gatchel [illegible] V. H. Neubert
8. CONTRACT OR GRANT NUMBER(s): N00014-75-C-0759
9. PERFORMING ORGANIZATION NAME AND ADDRESS: Dept. of Engng. Sci. & Mechanics, The Pennsylvania State University, University Park, PA 16802
10. PROGRAM ELEMENT, PROJECT, TASK AREA & WORK UNIT NUMBERS
11. CONTROLLING OFFICE NAME AND ADDRESS: Naval Research Laboratory, Washington, D.C. 20375
12. REPORT DATE: July 1977
13. NUMBER OF PAGES: 109 (12) 112 p.
14. MONITORING AGENCY NAME & ADDRESS (if different from Controlling Office)
15. SECURITY CLASS. (of this report): Unclassified
15a. DECLASSIFICATION/DOWNGRADING SCHEDULE

DISTRIBUTION STATEMENT A
Approved for public release
Distribution Unlimited

16. DISTRIBUTION STATEMENT (of this Report)

~~Qualified requestors may obtain copies of this report from DDC.~~

17. DISTRIBUTION STATEMENT (of the abstract entered in Block 20, if different from Report)

APPROVED FOR PUBLIC RELEASE
DISTRIBUTION UNLIMITED

18. SUPPLEMENTARY NOTES

DDC RECEIVED APR 25 1978 A

19. KEY WORDS (Continue on reverse side if necessary and identify by block number)

Shock, Viscoplastic, Beams, Bending, Material Behavior, Piping.

20. ABSTRACT (Continue on reverse side if necessary and identify by block number)

An analytical method is outlined, and a related computer program (VPBA) is discussed, for prediction of response of a viscoplastic cantilever beam to ground shock. Some beams, which could be built using standard piping, are designed and analyzed using inputs typical of those on the floating shock barge.

Viscoplastic Beam Analysis

DD FORM 1 JAN 73 1473 EDITION OF 1 NOV 65 IS OBSOLETE
S/N 0102-014-6601

Unclassified
SECURITY CLASSIFICATION OF THIS PAGE (When Data Entered)

AUTHORIZATION

This work was performed under ONR Contract No. N00014-75-C-0759, under the technical supervision, sponsorship, and funding of the Naval Research Laboratory.

ACKNOWLEDGMENTS

The benefit of discussions with Dr. R. O. Belsheim and Mr. Henry C. Pusey of the Naval Research Laboratory is gratefully acknowledged. The cooperation of Dr. E. Palmer and Mr. L. T. Butt of the Naval Ship Research and Development Center in supplying information regarding the floating shock barge is also appreciated.

SUMMARY

The two year study of viscoplastic beam bending consisted of two closely related phases:

Phase I: to develop procedures for analysis of viscoplastic beams of rectangular cross-section under combined tension and bending.

Phase II: to develop procedures for analysis of viscoplastic beams of more complex, tubular cross-section, but considering only bending deformations.

The analytical method for Phase I was developed and demonstrated in a detailed technical report, reference [26]. Predictions were included of elastic-plastic response of a symmetrical beam in combined bending and tension, under loading typical of the local shock machine. The method consisted of analytically dividing the beam cross-section into strips, a procedure presented in reference [24]. Subsequently

shock machine tests have been conducted. Agreement between predicted and measured responses was good only after the elastic flexibility of the supports was included in the analysis. The computer program now performs the analysis of a symmetrical viscoplastic beam on elastic supports. For the analytical method, along with the rate-dependent constitutive equations used, the reader is referred to reference [26].

The primary effort the second year was on Phase II which was different from Phase I as follows:

1) the input used was that of the floating shock barge.

2) the cross-sections considered were standard piping.

3) bending deformations only were included.

First, computer program VPBA was developed to predict the bending response of a viscoplastic cantilever beam carrying a tip mass. The program was checked by comparing with the solutions of Vogel [15,17] and Weiss [18]. Then beams and tip masses were sized-using experience of others and some approximate analysis, as outlined herein in Chapter IV - for use on the floating shock barge. The following parameters were considered: beam cross-sectional elastic stiffness, fundamental natural frequency, practical dimensions, and amount of desired penetration into the plastic range. These beams were then analyzed more precisely using VPBA and the shock barge input. A next logical step would be to carry out barge tests of these beams for comparison with predictions.

TABLE OF CONTENTS

TABLE OF CONTENTS (Continued)

LIST OF TABLES

LIST OF FIGURES

LIST OF FIGURES (Continued)

LIST OF FIGURES (Continued)

CHAPTER 1

INTRODUCTION

1.1 Discussion

The need for dynamic analysis of structures which undergo plastic deformation has long been acknowledged. Achieving a general analysis to predict the dynamic response of any structure, however, has yet to be accomplished. Only computer-based methods have produced solutions to the most simple of structures such as straight beams, single shells, rings and plates. Until such analyses are available, the design of structures which experience impact must rely on experimentation.

Much of the work in viscoplastic structures has occurred since World War II and most of the computer analyses were developed in the last decade. An early investigation by Duwez, Clark, and Bohnenblust (6) involved the plastic deformation of long beams which are subjected to a transverse constant velocity impact. The results showed that strain does not propagate at a constant velocity along the beam, but depended on the distance along the beam at which the deflection curve was zero. The analysis used bilinear stress strain relation and neglected strain rate effects.

An analysis of the transverse impact of long beams was also made by Conroy (5). Elastic strains were neglected to simplify the boundary value problem. However, in the case of a work-hardening material, the analysis failed to achieve a satisfactory solution.

Malvern (10) proposed a constitutive equation to account for the strain rate effects in materials in which stress is a function of

instantaneous strain and strain rate.

$$\dot{\varepsilon} = \frac{\dot{\sigma}}{E} + K\,(\sigma-\sigma_{st}) \qquad (1.1)$$

where K is a material constant. This strain rate dependency tended to account for an increase in the yield stress at impact and the plastic stress after yield.

Mentel (11) extended the rigid-plastic assumption used by Conroy (5) to investigate the plastic deformation of a uniform cantilever beam with an attached tip mass. A simplified analysis based on a one dimensional model was found to give good results when corrections for strain rate and strain hardening effects were included.

Strain rate dependence of the yield stress was included in the rigid plastic theory of Bodner and Symonds (1). Experiments were conducted on steel and aluminum alloy cantilever beams subjected to a base velocity impulse. The results were compared and showed a significant improvement in correlation by including strain rate effects.

Witmer, et al. (24) constructed a beam model of straight massless links that included axial deformation as well as bending. The rectangular cross-section of the beam was divided into equal, evenly spaced layers on which the stress was considered constant. Two stress strain relations were examined: (a) an elastic perfectly strain hardening material with effects of strain rate ignored, and (b) an approximation employed by Ting (21) in which the change in yield stress was a function of strain rate. When compared with experimental results of a fixed-fixed beam experiencing an explosive impulse at midspan, this model agreed well with the measured midspan deflection.

The effects of strain rate sensitivity and strain hardening were investigated by Jones (8). Using a constitutive equation suggested by Perrone (15),

$$\frac{\sigma}{\sigma_o} = f(\dot{\varepsilon})g(\varepsilon) \tag{1.2}$$

he showed that it is important to include strain rate effects when estimating permanent deformations of impulsively loaded beams in most cases. However, the overall beam size affected the need for inclusion of these effects. For example, beams with small length to depth ratios (L/H) that included only strain hardening or physically small beams with only strain rate sensitivity compared favorably with beams that included both. In addition, neither effect was important in physically large beams with large L/H ratios.

Stanovsky (18) investigated a cantilever beam on which a sudden force was applied to the tip mass. Experimental results were compared with theory that uses different yield points and various amounts of strain hardening.

Fully clamped beams under impact were investigated by Symonds and Jones (20). Solutions derived from rigid-plastic analysis which include strain rate dependence and transverse displacement compared favorably with experimental results. Strain rate sensitivity was included by use of an emperical equation

$$\frac{\sigma(\dot{\varepsilon})}{\sigma_o} = 1 + \left(\frac{\dot{\varepsilon}}{D}\right)^{1/p} \tag{1.3}$$

where p and D are material constants.

Vogel (22) compared experimental data of beams made with annealed mild steel and high strength tempered steel. Correlation with a finite difference type analysis showed good results. Also, the constitutive equation of Malvern (10) was rewritten for bending and verified. The time delay observed in experiments between the maximum moment and maximum curvature was adequately predicted by this equation.

Neubert and Yang (13) developed a stiffness matrix for a visco-plastic beam element based on a bilinear moment curvature relation and the constitutive equation of Malvern (10). Some examples showed that the rate of loading determined which slope dominated in the moment curvature relation.

Brown (2) presented experimental data on the dynamic effects of cold-rolling on steel specimens. The cantilever beams tested were designed with a natural frequency equal to that of the half sine wave impulse for maximum response. Using a simplified analysis and the constitutive equation of Malvern (10), comparisons with experimental results were good. He did suggest, however, that the constitutive equation may be limited to moderate strain rates of less than 10 in./in./sec.

Further analysis of cantilever beams with strain rate sensitivity was made by Ting (21). Equations of motion were developed in the form of two simultaneous non-linear integral equations. Approximate solutions were given and compared with experimental results.

Recently, R. C. Shieh (17) investigated the impact of a hexagonal mild steel frame which was dropped on to a pole obstacle at its center. In his analysis, Shieh used a fourth order Runge Kutta integration

technique to solve the non-linear system, and employed a power law variation to Malvern's constitutive equation. Material strain rate sensitivity effects were shown to be of primary importance, even at very low impact speeds. Correlation was shown to be good up to 2 percent of strain. However, correlation became increasingly poor for larger pole penetrations.

1.2 Scope of Report

This report is devoted to a theoretical study of viscoplastic beams with hollow circular cross sections that experience an impact load at the support. An analytical method is developed to determine the response of such beams. Results are then compared with other theoretical and analytical data to show the validity of the analysis. Finally, a set of beams having hollow circular cross sections is designed to undergo a prescribed amount of plastic deformation after an experimentally measured base velocity is applied. The beams are then analyzed and the results presented to see if the beams achieve the expected amount of deformation.

CHAPTER 2

MATHEMATIC MODEL OF AN ELASTIC-VISCOPLASTIC BEAM

2.1 Introduction

Over the past two decades several methods have been proposed to analyze plastic deformation of structures under dynamic loading. One of the most powerful methods in solving these highly non-linear problems has been the finite difference technique. It is also one of the most flexible methods in the analysis of beams because a variety of boundary conditions, input loadings, and special requirements can be easily included by the user. It is a computer-based method in which a series of equations, written in finite difference form, is solved in a sequential manner for a specified number of time increments. Unfortunately, an unstable response can result if the time increment is too large. Therefore, large computer run times are often necessary to complete the beam response.

The beams used in this study are long cantilever beams with large tip masses that undergo an impulse at the base as shown in Figure 1. The equations resulting from this type of beam are solved using a single grid finite difference scheme in space and time.

2.2 Derivation of Finite Difference Equations

The finite difference technique is based on knowing the displacement of each mass point at any instant of time. The initial displacement of all mass points is zero. The internal loads of the beam are determined from the displacements and from these the mass accelerations

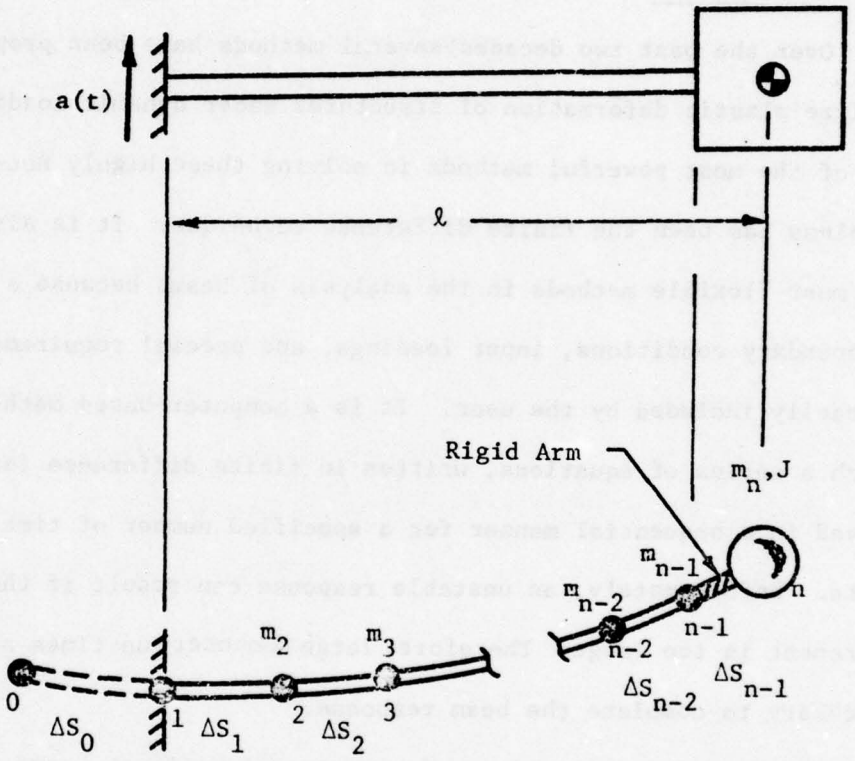

Figure 1. Mathematical Beam Model

are calculated. Using displacements at the previous time point and the mass accelerations, the displacements at the next time point are found.

In Figure 1 the mathematical model of the beam is composed of n-1 beam segments and n mass points beginning with point 1 at the support. A rigid arm is formed by clamping the tip mass on the end of the beam. The overall length of the beam is considered from the fixed end to the center of gravity of the tip mass.

In order to simplify the problem, the following assumptions are used to derive the necessary difference equations:

(1) Rotary inertias of the beam segments are negligible.

(2) No shear or extensional strains are considered.

(3) The tip mass is represented by a single mass and rotary inertia located at the center of gravity.

(4) The beam curvature is considered constant between mid-lengths of adjoining elements.

(5) All beam segments are equal in length except the rigid arm at the tip of the beam.

The equations developed hereafter are in the order used in the computer program.

2.3 Slopes and Mid-Slopes of the Beam

The slope, θ, and the mid-slope, θ^*, of each beam segment are determined geometrically from the known displacements at some time t.

$$\theta_i^* = \sin^{-1}\left(\frac{y_{i+1} - y_i}{\Delta S_i}\right), \quad i=0 \text{ to } n-2 \qquad (2.1)$$

where θ_i^* is the slope of the beam mid-way along the i^{th} segment. Since the curvature is assumed constant between mid-lengths, the slope of the i^{th} mass point is found by averaging the mid-slopes.

$$\theta_i = \left(\frac{\theta_i^* - \theta_{i-1}^*}{2}\right), \quad i=1 \text{ to } n-2 \tag{2.2}$$

From the boundary conditions of the beam it follows that

$$y_1, \theta_1 = 0 \tag{2.3}$$

Furthermore, the slopes at n and n-1 are equal because of the rigid element at the tip.

$$\theta_n, \theta_{n-1}, \theta_{n-1}^* = \sin^{-1}\left(\frac{y_n - y_{n-1}}{\Delta S_{n-1}}\right) \tag{2.4}$$

2.4 Curvatures and Curvature Rates

The exact curvature of the beam is given by

$$K(x) = \frac{\theta'}{(1+\theta^2)^{3/2}} \tag{2.5}$$

where $\theta' = d\theta/dx$. The slope is assumed to remain numerically small even though the analysis allows large displacements. Therefore, the denominator approaches unity and

$$K(x) \cong d\theta/dx \tag{2.6}$$

This approximation was shown to be valid by Vogel (22) and others.

Remembering assumption (4), the curvature is written in finite difference form as:

$$K_i = \frac{\theta_i^* - \theta_{i-1}^*}{\frac{1}{2}(\Delta S_i + \Delta S_{i-1})}, \quad i=1 \text{ to } n-2 \tag{2.7}$$

The curvature at the fixed end is found by using an image of the beam behind the support. Deflections of the imaginary point 0 are the same as point 2 on the actual beam. The base curvature is then given by Equation 2.7 where

$$\theta_o^* = -\theta_1^* \tag{2.8}$$

In order to calculate the curvature at n-1, an extrapolation of known curvatures near the end of the beam must be used. The curvature at n-2 is:

$$K_{n-2} = \frac{\theta^*_{n-2} - \theta^*_{n-3}}{\frac{1}{2}(\Delta S_{n-1} + \Delta S_{n-2})} \tag{2.9}$$

and the curvature at a point n-5/4 is

$$K_{n-5/4} = \frac{\theta_{n-1} - \theta^*_{n-2}}{\frac{1}{2}\Delta S_{n-1}} \tag{2.10}$$

From Figure 2, the curvature at n-1 can be written as

$$K_{n-1} = K_{n-2} + \Delta S_{n-2}\left(\frac{K_{n-5/4} - K_{n-2}}{\frac{3}{4}(\Delta S_{n-1})}\right) \tag{2.11}$$

or, rearranging

$$K_{n-1} = \frac{4}{3}K_{n-5/4} - \frac{1}{3}K_{n-2} \tag{2.12}$$

Of course, the curvature of the rigid arm is zero.

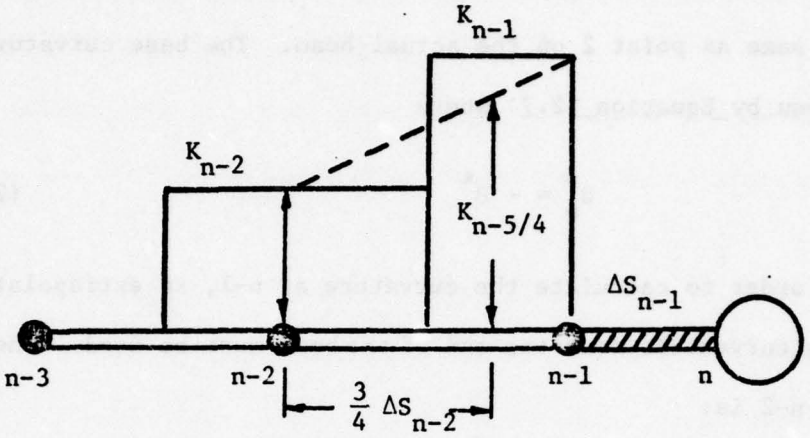

Figure 2. Determining K_{n-1}

Curvature rate is often important and is simply the backward timewise finite difference derivative of the curvature.

$$\dot{K}_i(t) = \frac{K_i(t) - K_i(t-\Delta t)}{\Delta t}, \quad i=1 \text{ to } n-1 \tag{2.13}$$

2.5 Static Internal Moment

By neglecting extensional and shear strains the beam is considered to be in a state of pure bending. Therefore, the curvature alone determines the value of internal static moment of the beam. Appendix A explains in detail the method used to obtain the static moment for points on the flexible portion of the beam. One of the end conditions of the beam, however, is

$$M_n = - J \ddot{\theta}_n \tag{2.14}$$

This moment can be written in terms of the known moments, M_{n-1} and M_{n-2}, as presented in Appendix B.

2.6 The Constitutive Equation

Of the many constitutive equations that have been proposed, essentially two have emerged as useful approximations to the visco-plastic phenomenon: the so-called power law, Equation 1.3, and Malvern's (10) equation. The latter is the one used in this study and has given good results when compared with experimental data (7,18,22)

For a brief explanation of this equation in terms of pure bending, consider a beam element that undergoes a constant curvature rate. The corresponding internal moment appears like that of Figure 3, somewhat higher than that obtained quasi-statically. Assume over some small time interval, Δt, that a change in curvature, Δk, occurs with a corresponding change in moment, ΔM. The total change in curvature is composed of an elastic part, $\Delta k'$, and a plastic part, $\Delta k''$, shown in Figure 4. The elastic part is expressed in terms of the change in moment.

$$\Delta k' = \frac{\Delta M}{EI} \tag{2.15}$$

and the plastic portion is proportional to the difference in the actual moment and the static moment.

$$\Delta k'' = \Delta t \; R \; (M - M_{st}) \tag{2.16}$$

Consequently, the total change in curvature is

$$\Delta k = \Delta k' + \Delta k'' \tag{2.17}$$

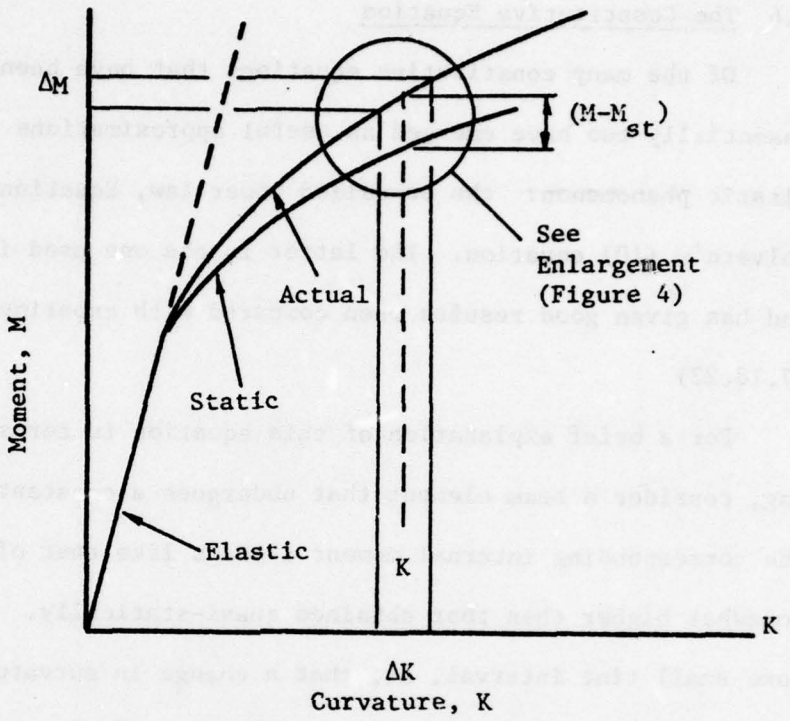

Figure 3. Effect of Curvature Rate on Viscoplastic Material

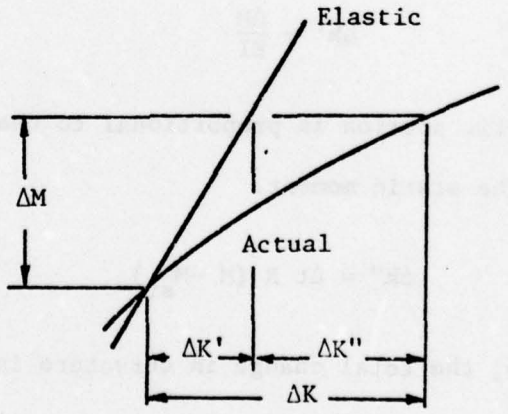

Figure 4. Change in Curvature

substituting,

$$\frac{\Delta k}{\Delta t} = \frac{\Delta M}{\Delta t} \frac{1}{EI} + R\,(M - M_{st}) \tag{2.18}$$

or in the limit

$$\dot{EI}\,k = \dot{M} + C\,(M - M_{st}) \tag{2.19}$$

where C = REI.

The equation, though derived for loading in the plastic range, is equally valid for loading in the elastic range or unloading from any point. Under these conditions the static and dynamic moments are equal, causing the term $C\,(M - M_{st})$ to vanish and leaving,

$$\dot{k} = \frac{\dot{M}}{EI} \tag{2.20}$$

The constant C in Equation 2.19 has been investigated by several researchers. Its effect on the resulting moment curvature relation was clearly presented by Neubert (14). A very small value of C will cause the constitutive equation to approach the elastic solution given by Equation 2.20 above. A large value of C, however, makes the equation approach that of the static moment curvature relation:

$$M = M_{st} \tag{2.21}$$

Some neutral value affects the time delay between the maximum moment and maximum curvature.

Determining an actual value to use for C was further complicated by the work of Frick (7) who presented evidence that the value of C

may not be a constant but may vary considerably with curvature and curvature rate. Vogel (22), however, showed that even large variations in C made little difference in the curvatures of the beam but some difference was obtained in the bending moments. Finally, Jones (8) suggested that viscoplastic effects became negligible in beams with large overall size. This is typical of a viscous phenomenon and means that the value of C should be increased when used in the analysis of such beams. The actual value of C used in this study is discussed in the next chapter, and is based on the values used by Vogel (22).

In order to include the constitutive equation in the analysis, it must be written in finite difference form,

$$EI\ \dot{K}_i(t) = \frac{M_i(t) - M_i(t - \Delta t)}{\Delta t} + C\ (M_i(t) - M_{st_i}(t)) \qquad (2.22)$$

solving for $M_i(t)$

$$M_i(t) = \frac{M_i(t - \Delta t) + \Delta t\ (EI\ \dot{k}_i(t) + C\ M_{st_i}(t))}{(1 + \Delta t\ C)} \qquad (2.23)$$

for i=1 to n-1.

Equation 2.23 allows the dynamic moment to be determined from the known quantities $\dot{K}_i(t)$, $M_{st_i}(t)$ and the dynamic moment from the previous time point, $M_i(t - \Delta t)$.

2.7 Mass Accelerations, $\ddot{y}_i(t)$

The mass accelerations are required before the last step can be completed, namely, finding the displacements at the next time

increment. Equations of motion for i^{th} mass point and the adjoining beam element can be written from the force diagram shown in Figure 5. Only two equations are significant: (1) sum of vertical forces on

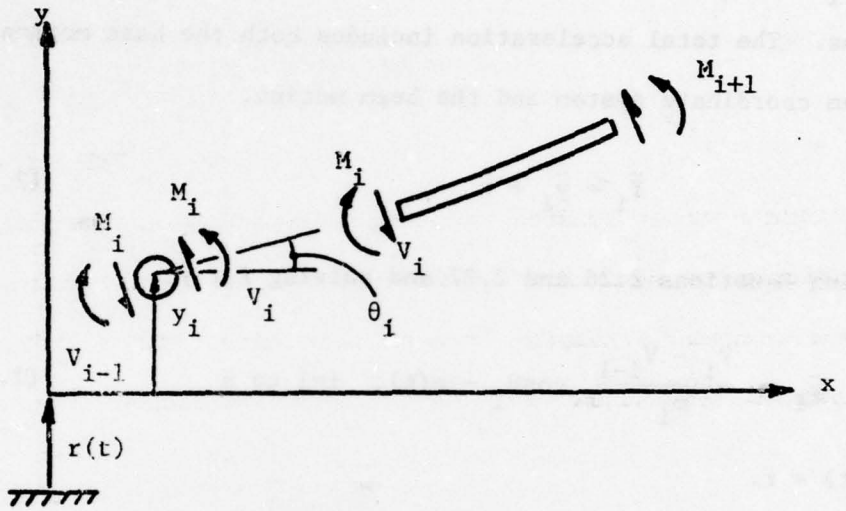

Figure 5. Force Diagram of Beam Element

the mass point, and (2) sum of moments on the beam elements. Remembering that the rotary inertia is neglected, the first equation gives,

$$V_i = - \frac{M_{i+1} - M_i}{\Delta S_i}, \quad i=1 \text{ to } n-1 \tag{2.24}$$

This is merely the equation from mechanics of materials in difference form that states V = -dM/dx. Note that

$$V_n = 0 \tag{2.25}$$

because no element exists beyond the $(i - 1)^{th}$ element.

The second equation is

$$(V_i - V_{i-1}) \cos\theta_i = m_i \ddot{Y}_i, \quad i=1 \text{ to } n \tag{2.26}$$

where $\ddot{Y}_i$ is the total acceleration of the i^{th} mass point and m_i is the mass. The total acceleration includes both the base motion of the beam coordinate system and the beam motion.

$$\ddot{Y}_i = \ddot{y}_i + \ddot{r} \tag{2.27}$$

Combining Equations 2.26 and 2.27 and solving for $\ddot{y}_i$,

$$\ddot{y}_i = \frac{V_i - V_{i-1}}{m_i} \cos\theta_i - a(t), \quad i=1 \text{ to } n \tag{2.28}$$

and $a(t) = \ddot{r}$.

Equation 2.28 includes the inertia effect of the tip mass from the calculation of M_n. Consequently, V_{n-1} is the correct force applied to the tip mass.

2.8 Deflections at $t + \Delta t$

The acceleration of the i^{th} beam mass can be written in the form of the central difference equation,

$$y_i(t) = \frac{y_i(t + \Delta t) - 2y_i(t) + y_i(t - \Delta t)}{(\Delta t)^2} \tag{2.29}$$

for i=1 to n.

Solving for $y_i(t + \Delta t)$

$$y_i(t + \Delta t) = 2y_i(t) - y_i(t - \Delta t) + \Delta t^2 \, y_i(t) \tag{2.30}$$

for i=1 to n.

The new displacements are in terms of the present and past displacements, $y_i(t)$ and $y_i(t - \Delta t)$; and the beam acceleration $\ddot{y}_i(t)$.

The series of equations developed in this chapter are used for each time in the solution until some final time, t_f, is reached. The time increment used in the calculations is 20 microseconds, which is based on the experience of Vogel (22).

CHAPTER 3

CORRELATION WITH OTHER DATA

3.1 Introduction

Much experimental data on viscoplastic beams has become available over the past 15 years and varied approaches have been used to predict these data. This chapter is included to present a sampling of comparisons with experimental and other theoretical methods. In addition, such comparisons add to the validity of the results presented later in Chapter 4.

Two references were chosen for correlation to supply an adequate test of the methods used in this study. Vogel (22) offers experimental data; while Weiss (23) presents a different theoretical point of view. Both are concerned with cantilevered beams with large tip masses which undergo some sort of base impact.

3.2 Correlation with Vogel

This reference was chosen because the theoretical method presented in Chapter 2 is similar to Vogel's. Furthermore, experimental data is available for comparison.

The beam tested was made of high carbon steel with the trade name 'Warplis'. The beam had a rectangular cross section with dimensions 1/8" x 1". Other physical parameters are listed below.

$$\ell = 5 \text{ in.}$$
$$m_n = .00762 \text{ lb sec}^2 \text{ in.}$$
$$J = .00894 \text{ lb sec}^2 \text{ in.}$$
$$EI = 4720 \text{ lb in.}^2$$
$$\mu = .916 \times 10^{-4} \text{ lb sec}^2/\text{in.}^2$$

Vogel also used the constitutive equation of Malvern (10), where the value of the constant is

$$C = 2000/\text{sec.}$$

These parameters were used in the computer program VPBA (Viscoplastic Beam Analysis) and they are compared with Vogel's in Figures 7 and 8.

The beam experiences an acceleration impulse shown in Figure 6 from a shock machine. During the test, the beam was fully instrumented with accelerometers at the support and on the tip mass. Strain measurements were also made along the beam.

In Figure 7 the curvature shows good correlation with experimental data. It should be pointed out that the difference between the two theoretical curves is that the curvature from Vogel (22) is calculated at a point 3/16" from the fixed end of the beam at the strain gage location, whereas, the curve from VPBA represents the curvature directly at the support.

The dynamic moment curvature curve in Figure 8 does not agree as well with experimental results. As observed by Vogel, the experimental dynamic moment is less than the static moment, a condition that cannot occur using this constitutive equation. The results however do show similar trends. In fact, one can observe that theoretical and experimental internal moments often differ significantly while such physical parameters as displacements, slopes and curvatures compare favorably. This suggests that the beam displacements are not especially sensitive to fluctuations in internal loads.

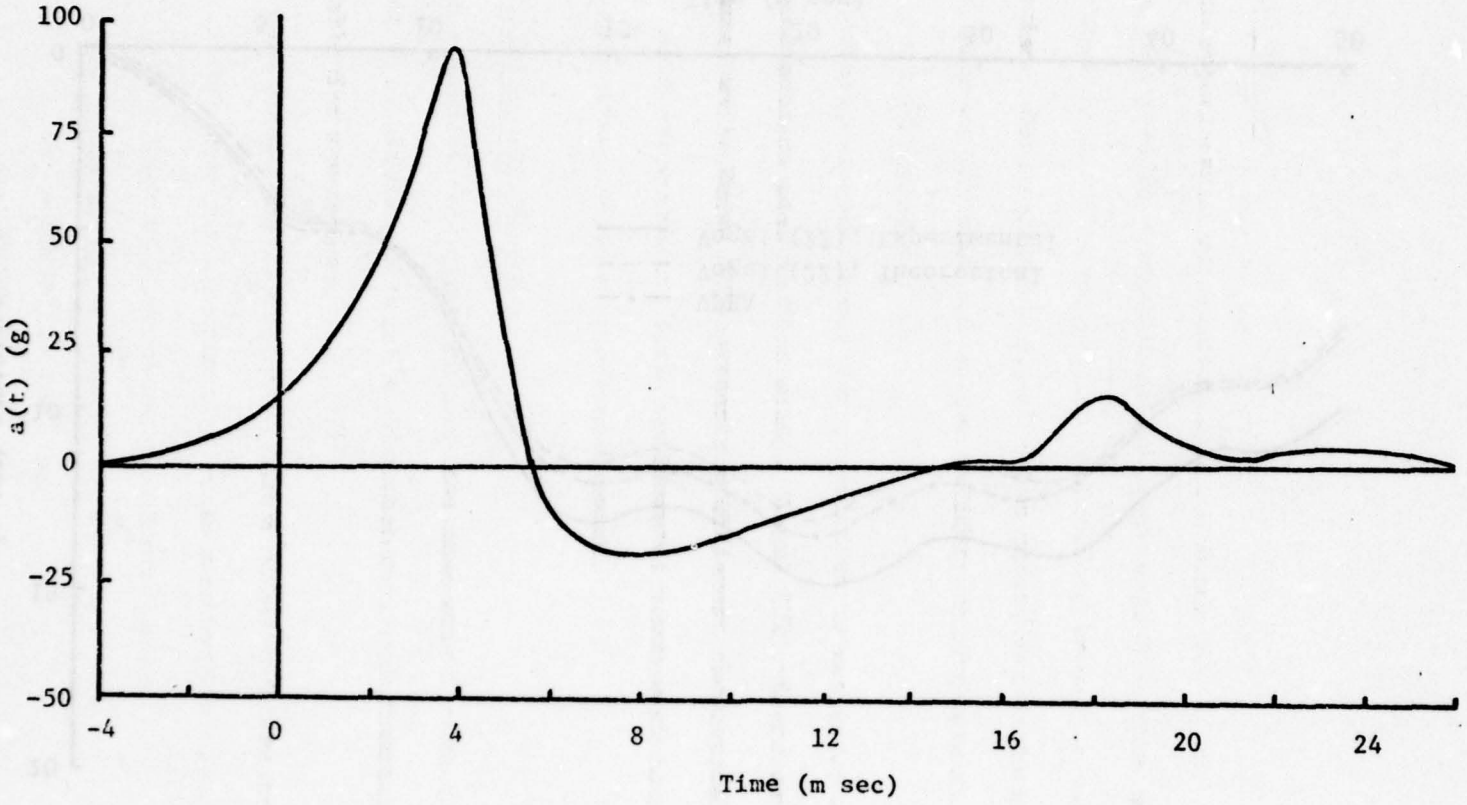

Figure 6. Experimental Base Acceleration from Reference 22

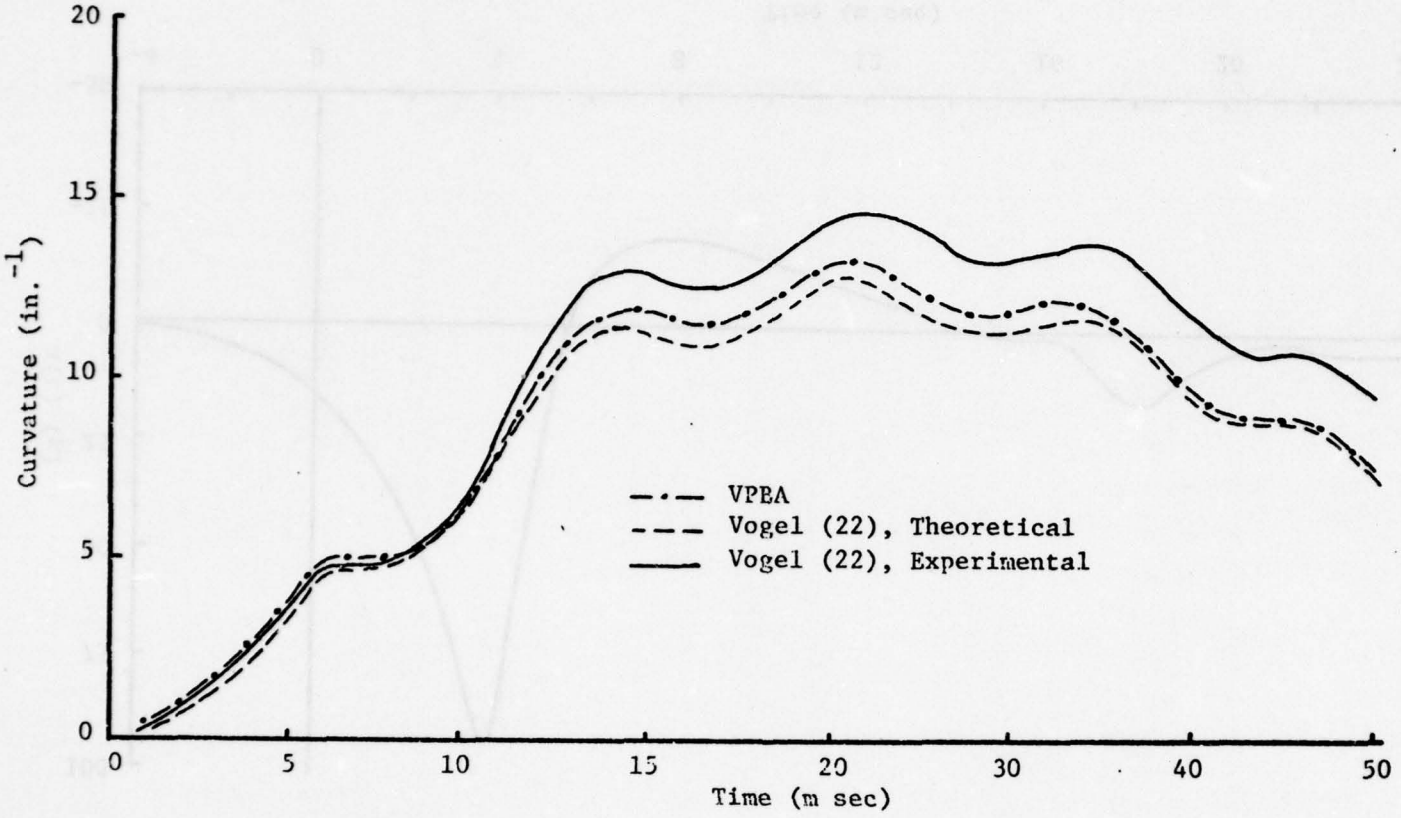

Figure 7. Comparison of Base Curvature with Reference 22

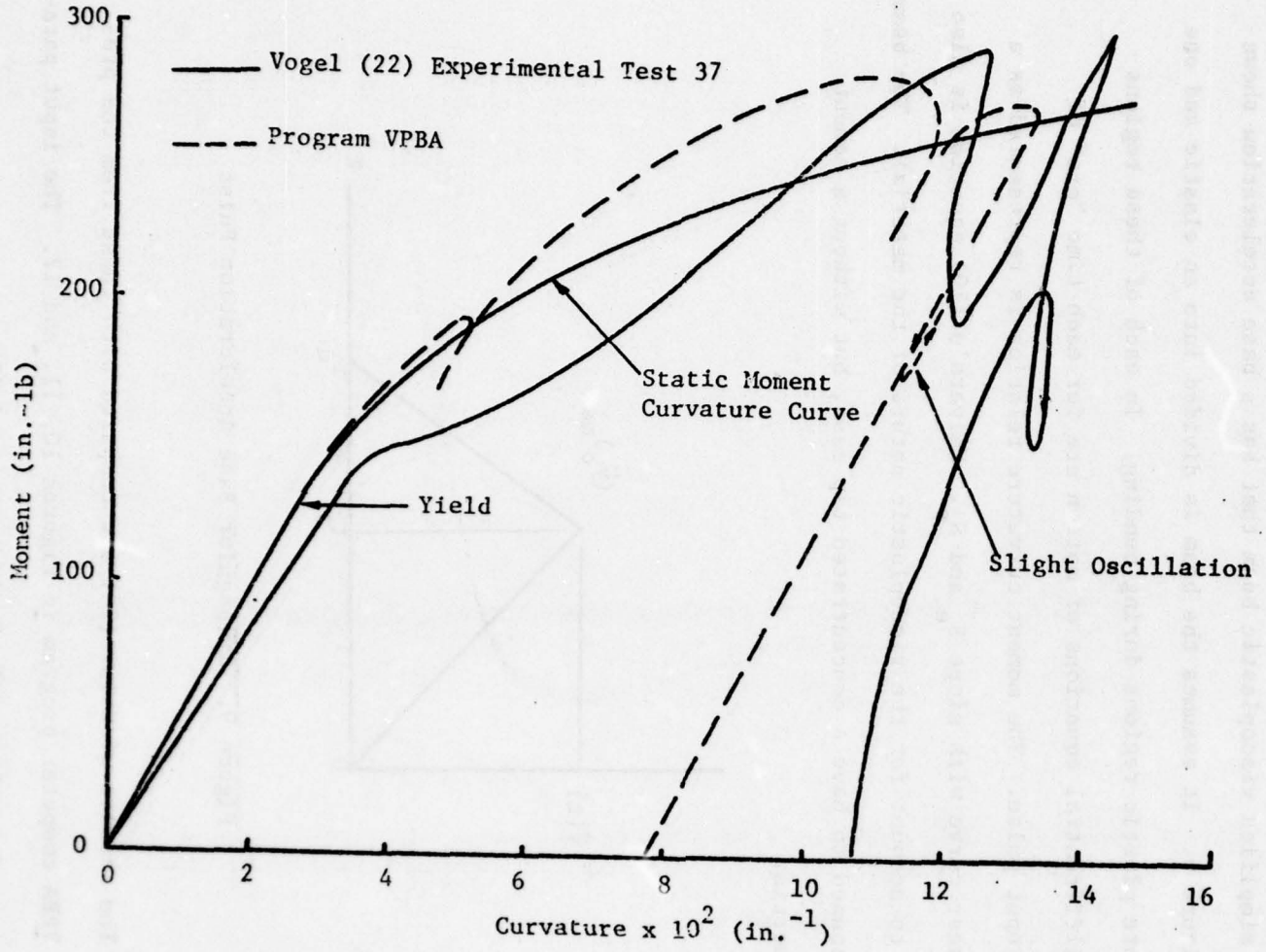

Figure 8. Comparison of Dynamic Moment Curvature Curves with Reference 22

3.3 Correlation with Weiss

The theoretical study of Weiss (23) presents the exact solution of a simplfied viscoplastic beam that has a base acceleration shown in Figure 9. It assumes the beam is divided into an elastic and one or more plastic regions during bending. In each of these regions the differential equations of motion are for each time "era" of the input pulse. The moment curvature relation is represented as a bilinear curve with slope S_e and S_p. Malvern's (10) equation is also used to account for the viscoplastic nature of the material. The beam is assumed to have a concentrated tip mass, but without a moment of inertia.

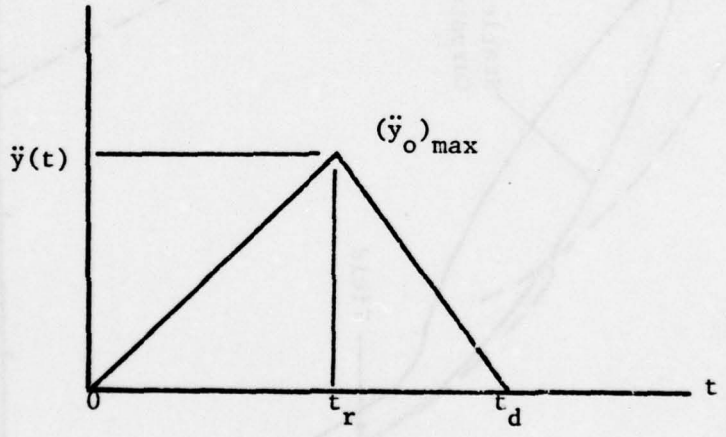

Figure 9. Triangular Base Acceleration Pulse

The results of Weiss (23) are compared with those from the present VPBA computer program in Figures 10, 11, and 12. The input parameters used in these calculations are as follows:

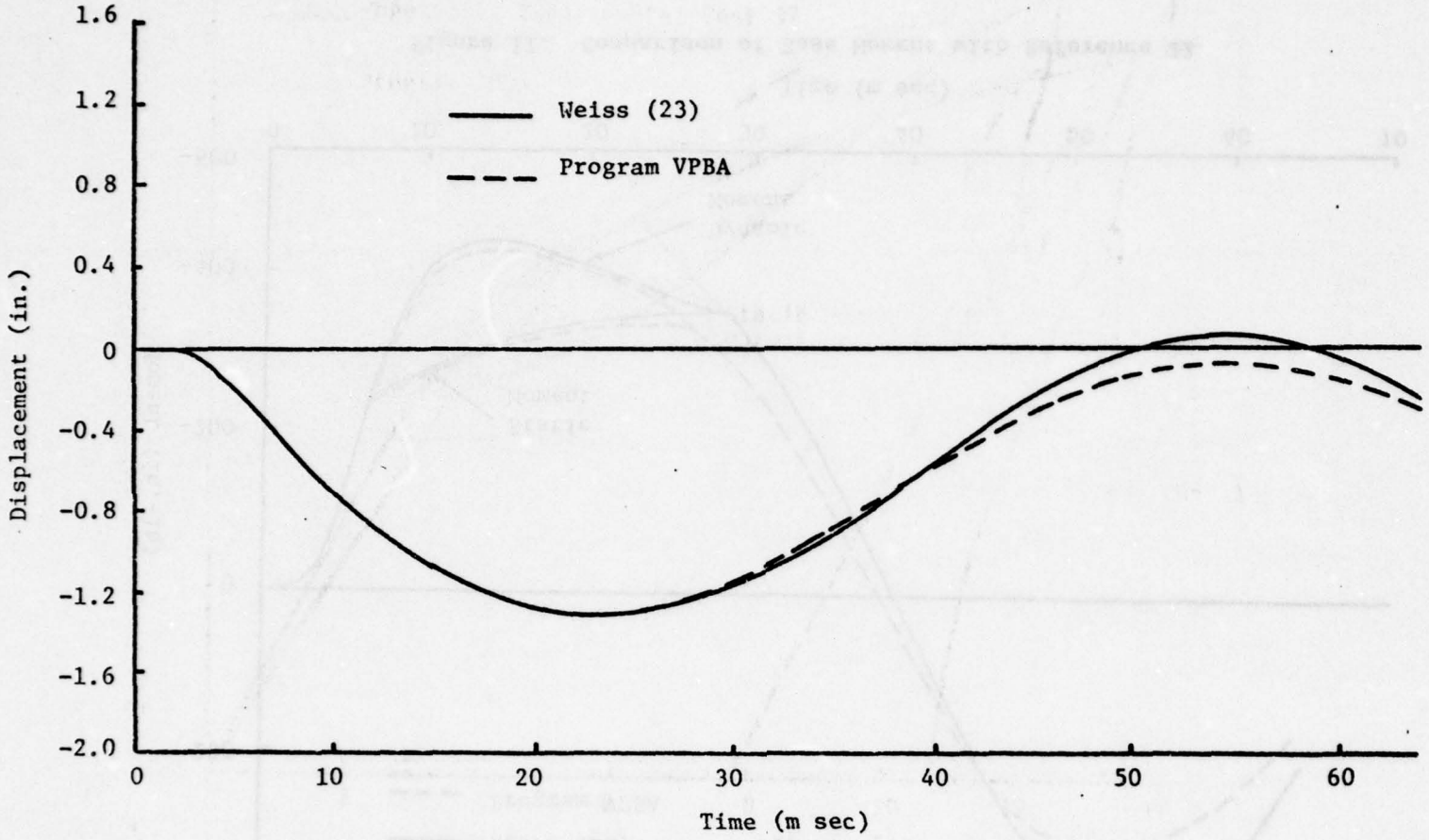

Figure 10. Comparison of Tip Mass Displacement with Reference 22

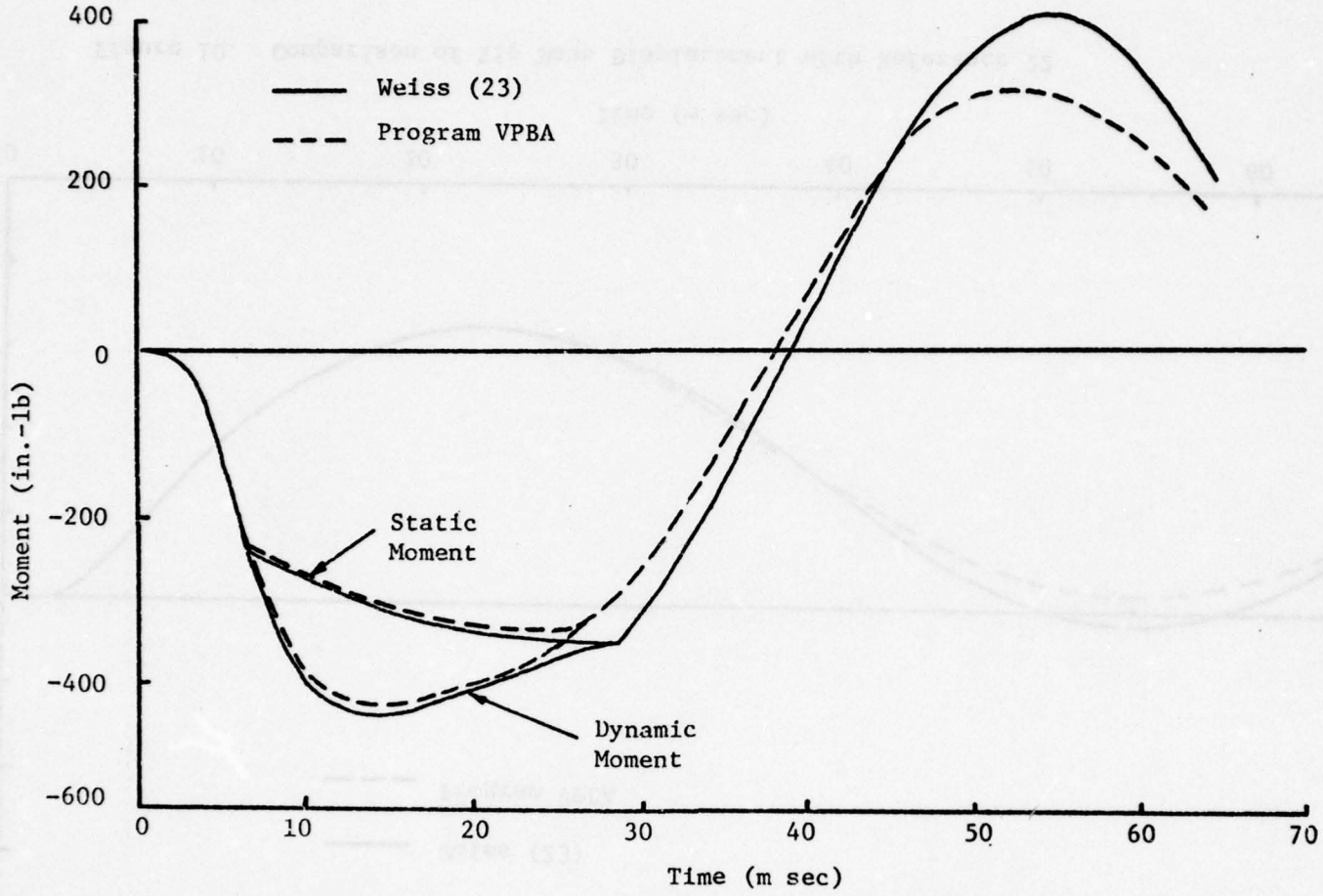

Figure 11. Comparison of Base Moment with Reference 22

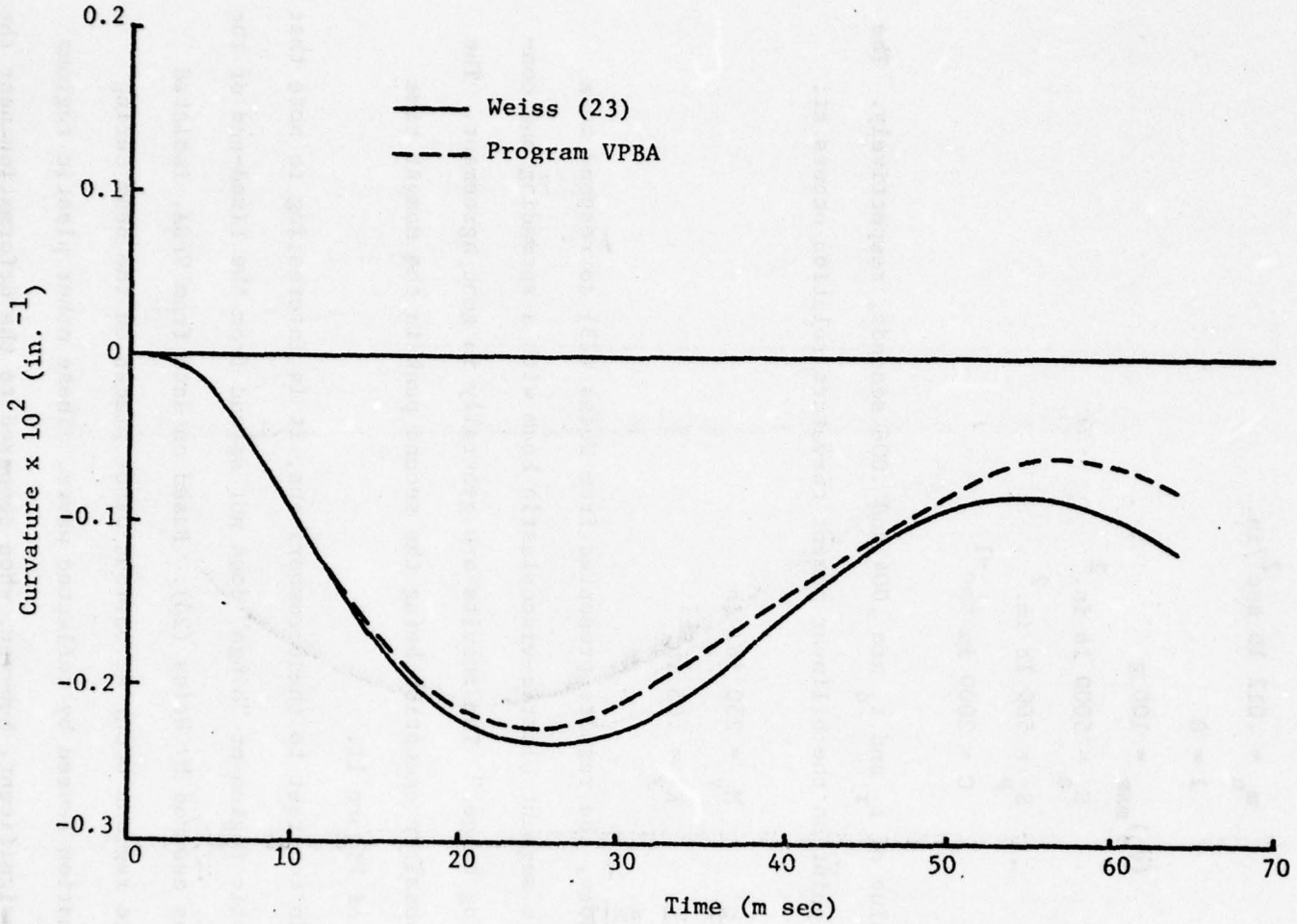

Figure 12. Comparison of Base Curvature with Reference 23

$$\ell = 5 \text{ in.}$$

$$m_n = .012 \text{ lb sec}^2/\text{in.}$$

$$J = 0$$

$$(\ddot{y}_o)_{max} = 100 \text{ g}$$

$$S_e = 5000 \text{ lb in.}^2$$

$$S_p = 500 \text{ lb in.}^2$$

$$C = 2000 \text{ in. sec}^{-1}$$

The value of t_r and t_d are .004 and .006 seconds, respectively. The yield point on the bilinear moment curvature relation occurs at:

$$M_y = 250 \text{ in. lb}$$

$$K_y = .05 \text{ in.}^{-1}$$

Note, the results presented from Weiss (23) correspond to a "double segment elastic-viscoplastic beam with a spreading and contracting hinge." The results are generally in good agreement. The only possible exception being the second peak in the moment time curve of Figure 11.

In contrast to these comparisons, it is interesting to note that a plastic region or "hinge" does not spread from the fixed-end of the beam as assumed by Weiss (23). Based on data from VPBA, isolated plastic regions occur at various other places on the beam during deformation caused by reflected waves. These other plastic regions are insignificant, however, when compared to the deformation near the base as verified by the results presented here.

CHAPTER 4

DESIGN AND ANALYSIS OF BEAMS OF CIRCULAR CROSS SECTION

4.1 Introduction

Many experiments have been done with impulsively loaded cantilever beams of various cross-section, size and material. In this chapter the results from some of these tests are unified, and used to design and investigate a set of cantilever beams with hollow circular cross-sections.

The basis of the beam design is a comparison of tests using data collected from references 1, 2, 3, and 22, and presented in Figure 13. All of these data are for steel beams each having a large tip mass. Furthermore, all of the beams are of rectangular cross section with the exception of those from reference 3 which are I-beams.

Figure 13 is an attempt to provide some means of determining the extent of plastic deformation a beam will experience during loading. For each of the references mentioned the non-dimensional parameter χ is plotted versus a "penetration factor," η. The parameter χ includes two quantities that effect the maximum deformation of a beam: the peak acceleration of the base, a_p, and the natural frequency, ω. It should be mentioned that other factors such as the relative size of the tip mass, the shape of the applied impulse and the material properties also effect the amount of plastic deformation. These were not included because of the limited available information from each of the references.

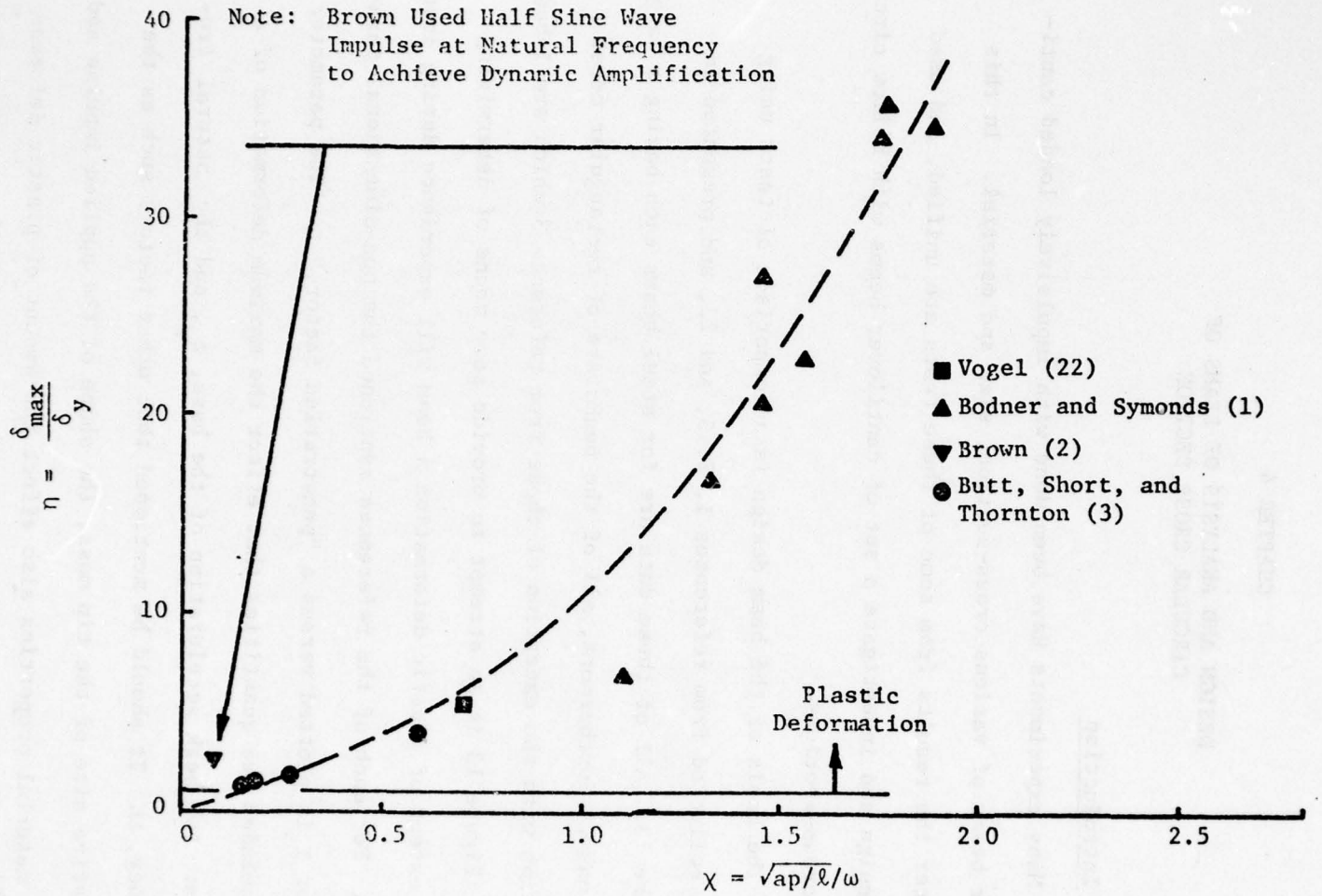

Figure 13. Comparison of Deformations from Experiments on the Impact of Steel Beams

The penetration factor, η, is an indication of how much plastic deformation occurs and is defined as,

$$\eta = \frac{\delta_{max}}{\delta_y} \tag{4.1}$$

where δ_{max} is the maximum deformation and δ_y is the deformation required to yield the material at any point on the beam. For each reference the value of η was determined differently because of the variety of data available. For instance, in reference 1 the deformation is the tip mass rotation, in reference 3 it is the displacement of the tip mass, while in reference 2 the base curvature is used. The results, however, do show a definite trend represented by the dashed line. This curve is only intended to give an approximate measure of beam deformation. Other test results may produce more scatter in the data.

4.2 Beam Selection

The beams selected for use in this study are similar in size to those used by Butt, Short, and Thornton (3). Furthermore, the base input shown in Figure 14 is used for all beams in this chapter. This base velocity measurement was made by attaching a velocity meter to the base of one of the I-beams used in the test. The beams were fixed to the floor of the Floating Shock Platform and shock tested using an underwater explosion. The result shown in Figure 14 produced rapid oscillations in velocity which did not allow the beam time to respond, therefore, the approximate velocity input was found to be adequate.

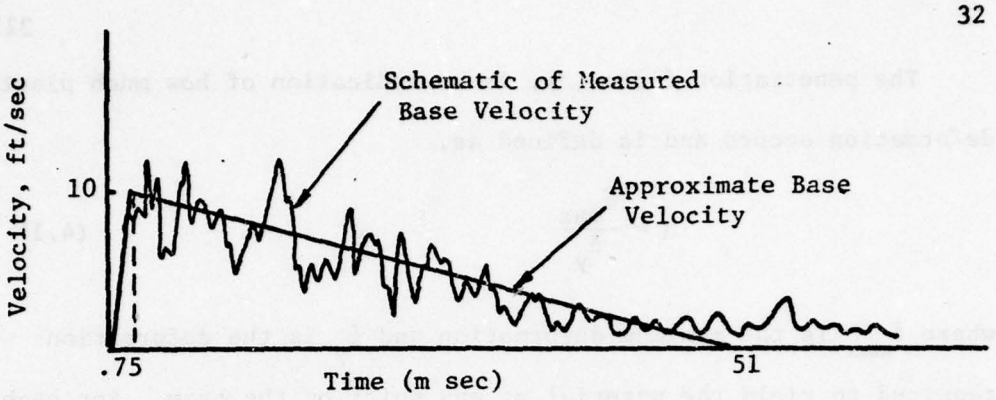

Figure 14. Velocity Input of Reference 3

Two sets of four beams constructed of standard steel pipe are studied with the dimensions given in Table 1. One set of beams uses pipe with a 2-1/2-inch inner diameter which compares closely with the 3-inch I-beam of reference 3. The other set is designed with 1-1/2-pipe and used for comparison of size effects.

Standard pipes made of mild steel are formed by several different processes which effect their stress properties. The type used in this study is seamless with an ASTM specification of A53, Grade B. The properties of this steel are listed below:

.2 percent offset yield:	σ_y	= 35,000 psi
Ultimate stress:	σ_u	= 60,000 psi
Modulus of Elasticity:	E	= 29×10^6 psi
Yield Strain:	ε_y	= .001207 in./in.
Weight density:	ρ	= .283 lb/in.^{3}

Table 1. Cross-Sectional Dimensions

Inner Diameter (in.)	Outer Diameter (in.)	Wall Thickness (in.)	Metal Area ($in.^2$)	Weight per Inch (lb/in.)	Moment of Inertia ($in.^4$)
2-1/2	2.875	.276	2.254	.638	1.925
1-1/2	1.900	.200	1.068	.303	0.391

Hollow circular cross sections under the action of bending are capable of buckling. The analysis of such a problem in the plastic regions would present a formidable problem. The experimental results of Frick (7), however, presents some evidence on how to present collapse of the cross section. These tests were made with simply supported, pinned-pinned beams: one made of steel tubing and the other made with a copper-nickel tubing. The copper-nickel tubing had a thickness to radius ratio of 0.21, while the steel had a thickness to radius ratio of only 0.10. Maximum curvatures occurred at the edge of the large center mass.

The steel tubing exhibited rippling on the compression side because of the thin wall. However, the cross section did not collapse, probably because it was stabilized by the weight block clamped around the center. A cantilever pipe is supported in a similar manner near the base.

The copper-nickel tubing showed no effect of buckling because the wall thickness was larger. As a result, both steel pipes used in the study were selected to have a wall thickness of approximately 20 percent of their outer radii.

The static moment curvature relations for these pipes are shown in Figure 15. These curves are determined from the computer program MCURVE based on the procedure outlined in Appendix C. An elastic-perfectly plastic material is assumed and the cross section remains undistorted during loading. The yield point for the 2-1/2 inch pipe is

$$K_y = .000839 \text{ in.}^{-1}$$

$$M_y = 46{,}860 \text{ in. lb}$$

and for the 1-1/2 inch pipe

$$K_y = .001270 \text{ in.}^{-1}$$

$$M_y = 14{,}400 \text{ in. lb}$$

4.3 Natural Frequency

It is necessary to know the natural frequency of the beam in terms of its physical parameters before an effective set of beams can be designed. The important beam parameters are shown in Figure 16. The first natural mode can be approximated by superposing two solutions:

(1) A two degree-of-freedom massless beam with a tip mass and moment of inertia.

(2) A continuous beam without a tip mass.

In the first case, the frequency equation is written from the equations of motion of tip mass displacement and rotation:

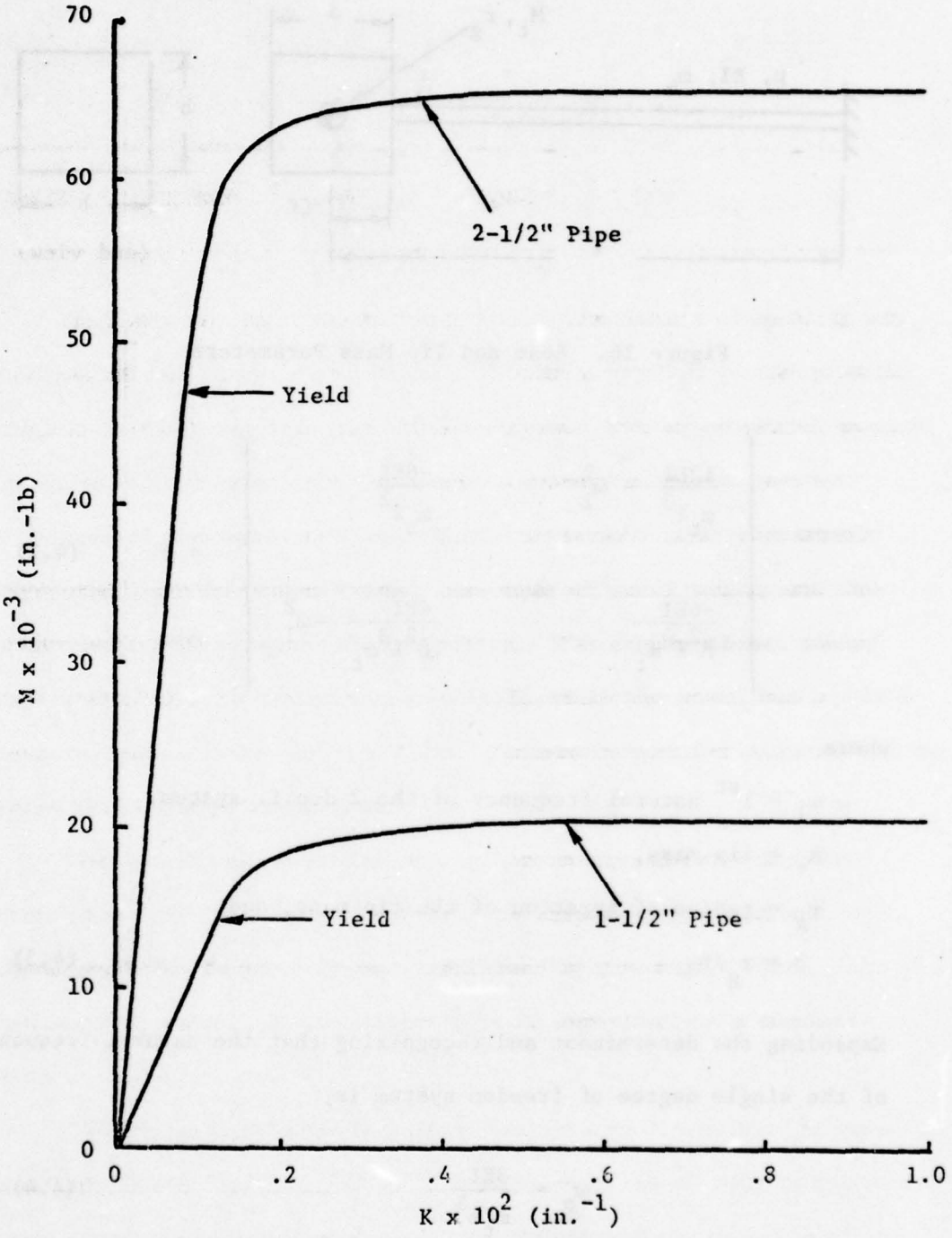

Figure 15. Static Moment Curvature Curve for Selected Steel Pipes

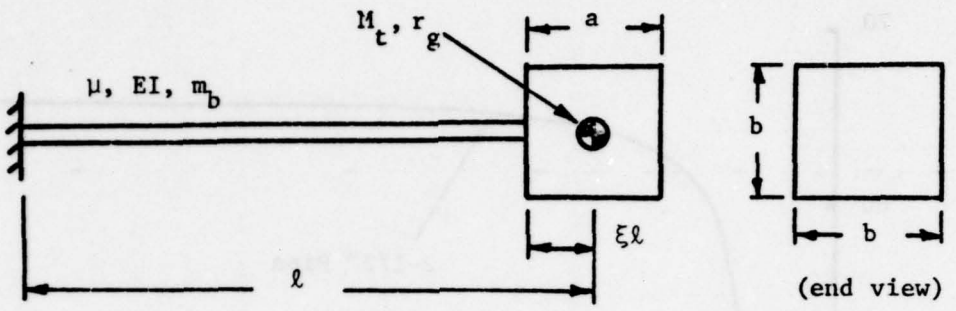

Figure 16. Beam and Tip Mass Parameters

$$\begin{vmatrix} \frac{12EI}{m_t\ell^3} - \omega_1^2 & \frac{-6EI}{m_t\ell^2} \\ \frac{-6EI}{\beta^2\ell^4 m_t} & \frac{4EI}{\beta^2\ell^3 m_t} - \omega_1^2 \end{vmatrix} = 0 \qquad (4.2)$$

where

ω_1 = 1st natural frequency of the 2 d.o.f. system,

m_t = tip mass,

r_g = radius of gyration of the tip mass, and

$\beta = r_g/\ell$ (4.3)

Expanding the determinant and recognizing that the natural frequency of the single degree of freedom system is

$$\omega_o = \frac{3EI}{m_t\ell^3} \qquad (4.4)$$

the frequency equation becomes:

$$\omega_1^4 - \frac{4}{3}\left(3 + \frac{1}{\beta}\right)\ \omega_o^2\ \omega_1^2 + \frac{4}{3}\ \frac{1}{\beta^2}\ \omega_o^4 = 0 \qquad (4.5)$$

This quadratic in ω_1 is solved for the lowest natural frequency.

$$\omega_1^2 = C_\beta\ \omega_o^2 \qquad (4.6)$$

where

$$C_\beta = \frac{2}{3}\left(3 + \frac{1}{\beta^2}\right) - \sqrt{\frac{4}{9}\left(3 + \frac{1}{\beta^2}\right)^2 - \frac{4}{3}\ \frac{1}{\beta^2}} \qquad (4.7)$$

For the case of a continuous beam without a tip mass, the frequency of the first mode is

$$\omega_2 = 3.52\ \sqrt{\frac{EI}{\mu\ell^4}} \qquad (4.8)$$

Assuming the beam mass is a certain fraction of the tip mass, then

$$\lambda = m_b/m_t \qquad (4.9)$$

or

$$m_b = \mu\ell = \lambda\ m_t$$

Substituting this into Equation 4.7 the natural frequency is

$$\omega_2^2 = C_\lambda\ \omega_o^2 \qquad (4.10)$$

where

$$C_\lambda = 4.13/\lambda \qquad (4.11)$$

The effects of these solutions are combined in the following manner to approximate the first mode frequency:

$$\frac{1}{\omega^2} = \frac{1}{\omega_1^2} + \frac{1}{\omega_2^2} \tag{4.12}$$

Substituting Equations 4.6 and 4.10 and solving

$$\omega^2 = C_f(\beta,\lambda)\ \omega_o^2 \tag{4.13}$$

where

$$C_f = \frac{C_\beta\ C_\lambda}{C_\beta + C_\lambda} \tag{4.14}$$

This solution will be slightly different than the exact solution because the mode shape of the beam is not the same as the mode shape assumed for solution 2. For beams with relatively large tip masses, however, the difference is small.

4.4 Effect of Tip Mass

The shape of the tip mass must be incorporated in the design analysis. This is done by considering the tip mass attached to the end of the beam at some distance $\xi\ell$. Furthermore, assume the tip mass is rectangular with dimensions a x b x b as shown in Figure 16. The portion of the beam which is attached to the mass is therefore,

$$a = 2\xi\ell \tag{4.15}$$

Recalling

$$\lambda = \frac{m_b}{m_t} = \frac{\rho A_s \ell}{\rho a b^2} \tag{4.16}$$

and assuming the tip weight is also made of steel, the dimension b is then

$$b = \sqrt{\frac{A_s}{2\xi\lambda}} \tag{4.17}$$

where A_s is the cross sectional area of the beam.

An additional relation can be written from the definition of β in Equation 4.3. The radius of gyration by definition is $\sqrt{J/m_t}$ where J is the tip mass moment of inertia. Therefore,

$$\beta^2 = \frac{J/m_t}{\ell^2} = \frac{\frac{1}{2} m_t (a^2 + b^2)}{m_t \ell^2} \tag{4.18}$$

Substituting for a and b and rearranging

$$\beta = \sqrt{\frac{\xi^2}{3} + \frac{a_r}{24\xi\lambda}} \tag{4.19}$$

and a_r is the area ratio, A_s/ℓ^2. Equation 4.19 relates the non-dimensional radius of gyration β in terms of the non-dimensional parameters ξ, λ and a_r.

It is interesting to see a plot of β versus a_r for various values of λ. In Figure 17, ξ is 0.1 for all curves. β varies considerably if the ratio of beam mass to tip mass, λ remains constant.

In Figure 18 some experimental values of λ and β are presented for comparison. These data show a practical design range for β is between 0.09 and 0.14, and that a reasonable value of λ is 0.13 if a large tip mass is to be considered. On three of the four beams used by reference 3, the value of λ is 0.13.

Retaining a constant beam to tip mass ratio for all beams is advantagenous in that the range in length of the beams tends to be small for a wide variation in penetration factor. For example, a small beam with a constant λ would have a small tip mass and thereby a small penetration factor. To increase the penetration, the beam must be made longer resulting in a large tip mass. Similarly, a large beam with a large tip mass must be made smaller to avoid excessive penetration under impact. As a result, the beams used for both sets of pipe are designed with a constant λ of 0.13.

4.3 Beam Design

The elastic beams described in reference 3 were designed to have a range of natural frequencies from 20 to 200 hz. in order to determine a shock spectrum and achieve a wide response to the applied impulse. From the results shown in Figure 13, three of the four beams exhibited small plastic deformations during the dynamic tests. Only the low frequency beam at 20 hz. had a penetration above two. In order to avoid this problem, the beams in this study are designed to have appreciable plastic deformation by investigating a lower frequency range.

The actual design of the beams begins with Figure 13. The basic criterion is that each set of beams is required to achieve approximate

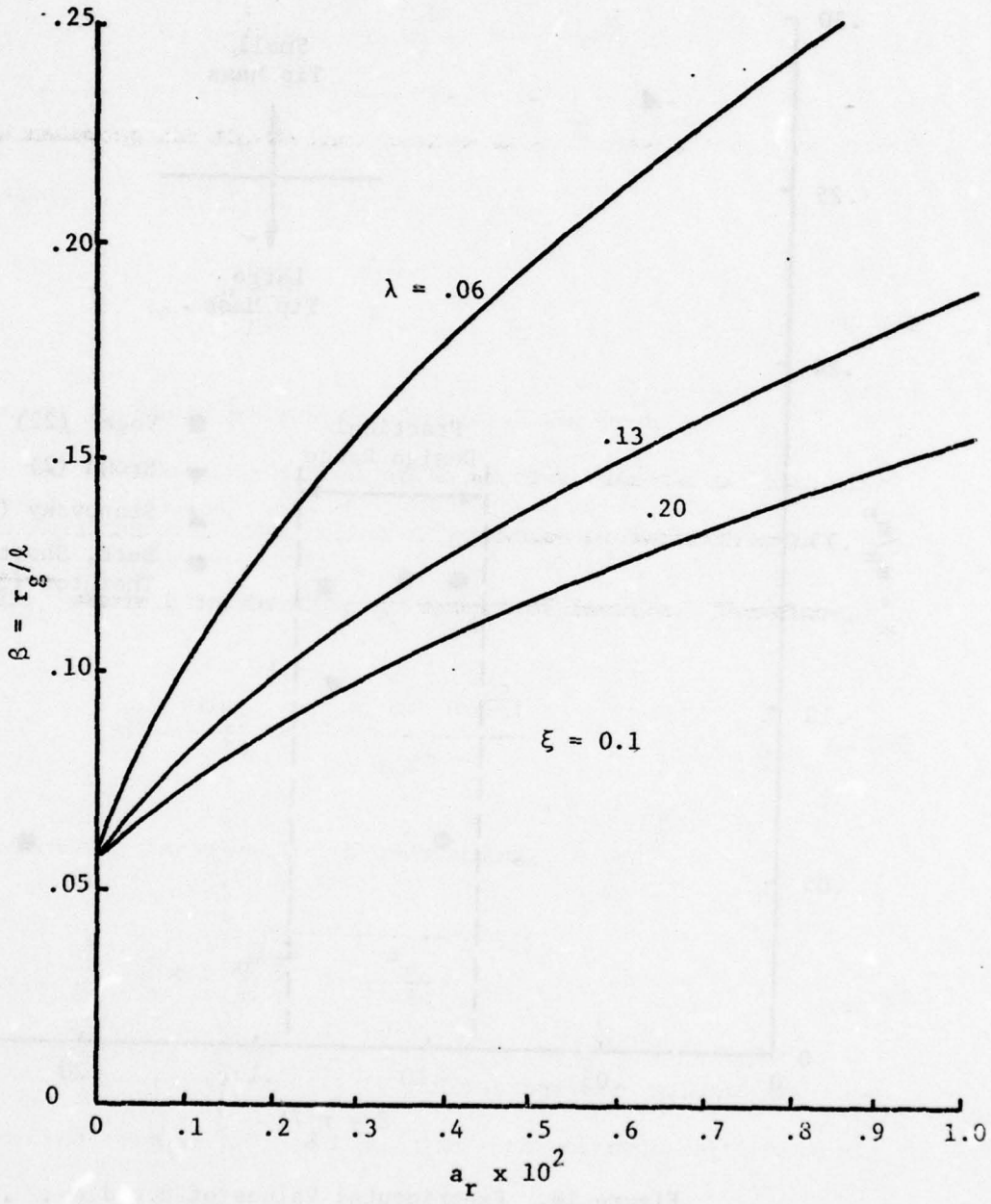

Figure 17. Variations in Tip Mass Parameters

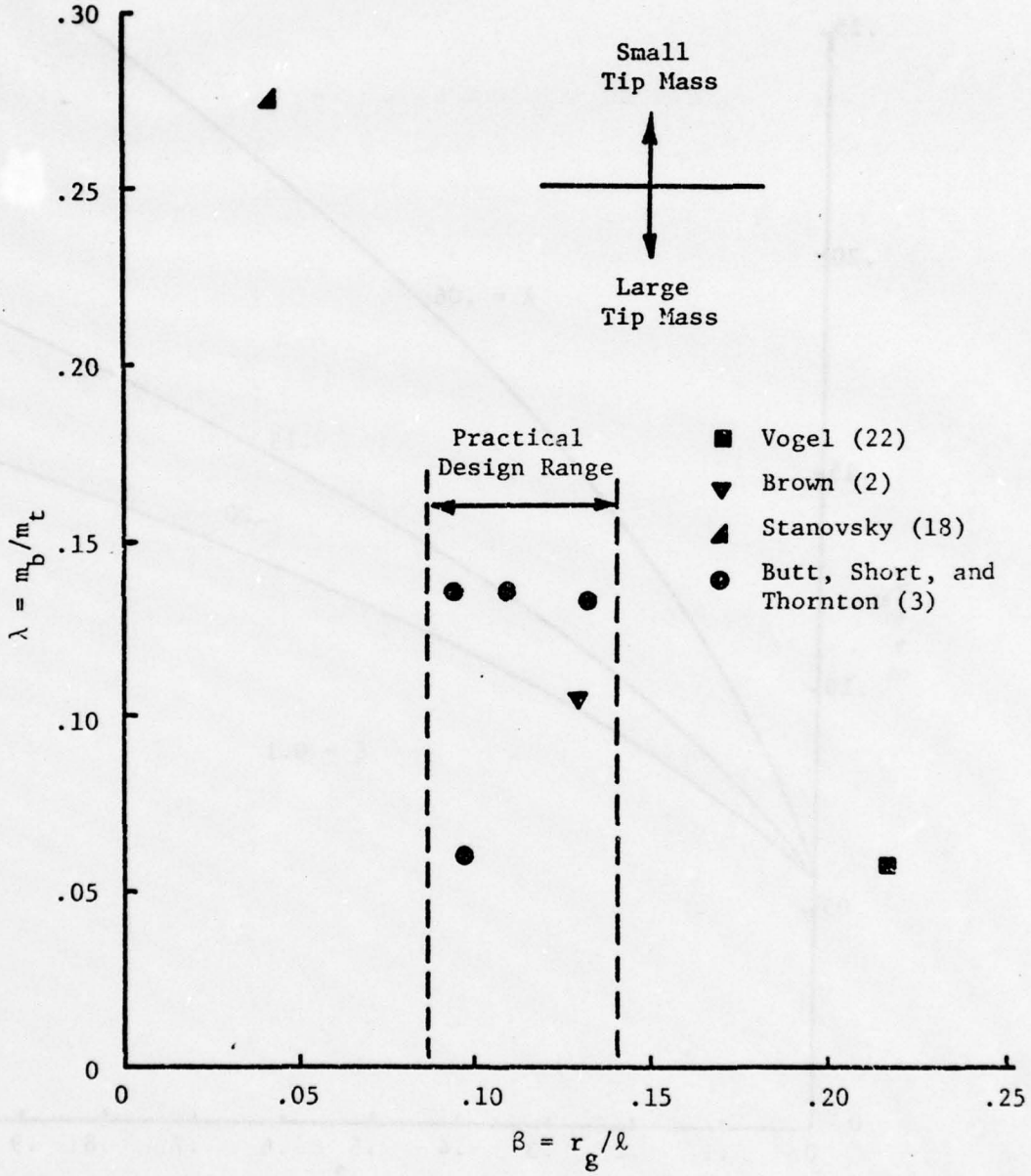

Figure 18. Experimental Values of β and λ

penetrations of .8, 6, 4, and 2. These correspond to values of χ at 0.85, 0.70, 0.50, and 0.30. To determine the corresponding length of each beam consider

$$\chi^2 = \frac{a_p/\ell}{\omega^2} \tag{4.20}$$

substituting Equations 4.4 and 4.13

$$\chi = \sqrt{\frac{a_p\, m_t \ell^2\, (C_\lambda + C_\beta)}{3EI\; C_\lambda\; C_\beta}} \tag{4.21}$$

The value of a_p is 1.6×10^5 in./sec^2 as determined from Figure 14. The parameter C_β, however, is a function of length as is the tip mass.

$$m_t = \mu\ell/\lambda \tag{4.22}$$

Therefore, the length cannot be determined directly from Equation 4.21. Instead, values of length are substituted until the necessary values of χ result. This procedure is used for both the 1-1/2 and 2-1/2 inch pipe and the final design data presented in Table 2. The tip mass moment of inertia is found from the value of β obtained from Equation 4.19.

$$J = m_t\, r_g^2 = \beta^2 \ell^2\, m_t \tag{4.23}$$

From Table 2, notice the range of natural frequencies is much smaller than that of reference 3 which ranged from 20 hz. to 200 hz. The values of C_f are near one, indicating the moment of inertia and beam mass have little effect on natural frequency compared to that

Table 2. Beam Parameters

ℓ (in.)	β (--)	$a_r x10^2$ (--)	C_β (--)	C_f (--)	m_t (lbs)	ω_0 (hz.)	ω (hz.)	χ (--)	η (--)
				(2-1/2 Inch Pipe)					
39.0	.0899	.1482	.9820	.9526	191.5	12.0	11.7	.87	8
34.0	.0979	.1950	.9788	.9495	167.0	15.8	15.4	.71	6
27.0	.1151	.3092	.9708	.9420	132.6	25.1	24.3	.50	4
19.0	.1528	.6244	.9493	.9218	93.3	50.6	48.6	.30	2
				(1-1/2 Inch Pipe)					
29.0	.0860	.1270	.9835	.9540	67.6	14.2	13.9	.85	8
25.0	.0939	.1709	.9804	.9511	58.2	19.1	18.7	.68	6
20.0	.1090	.2670	.9737	.9447	46.6	29.9	29.1	.49	4
14.0	.1442	.5449	.9547	.9268	32.6	61.1	58.8	.29	2

of the tip weight. None of the beams is extremely short, thus validating the assumption of pure bending. The longest beam is 39 inches, which is not too long for a test beam of this size.

4.6 Results

The beam parameters developed in the preceding section were entered in the response program VPBA (Viscoplastic Beam Analysis) listed in Appendix D. In Table 3, these parameters are listed in the form needed by the computer program and given designation for identification in the results that follow. The segment lengths of the beam are ΔS_i except for the rigid element which has a length ΔS_{n-1}. Beam mass at each point is m_i and the tip mass and moment of inertia are m_n and J, respectively. The total number of points on the beam is n, beginning with the support at point 1.

Choosing an exact value of C analytically is difficult. Instead, the value used to obtain the results in this chapter is based on the value used by Vogel (22) and corrected for the larger overall cross section. Vogel (22) used a value of 2,000/sec whereas a value of 10,000/sec is used in this study. The effect of the difference is shown in Figures 26 and 29. The response is considerably different for the results using the larger value of C. However, the major effect is to reduce the moment in areas of high curvature rate making the curve more closely approach that of the static moment curvature relation. This is mentioned by Jones (8) and discussed in Chapter 2. In addition, the maximum curvature is larger using the larger value of C--an effect also observed by Vogel (22).

Table 3. Beam Designation and Design Values

Desig-nation	Pipe	ρ (in.)	n	ΔS_i (in.)	ΔS_{n-1} (in.)	$m_i \times 10^2$ (lb sec^2 in.)	m_n (lb sec^2 in.)	J (lb sec^2 in.)
A1	2-1/2	39.0	11	3.900	3.90	.6444	.4957	6.095
A2	2-1/2	34.0	9	4.371	3.40	.7222	.4321	4.797
A3	2-1/2	27.0	8	4.050	2.70	.6691	.3432	3.315
A4	2-1/2	19.0	6	4.275	1.90	.7063	.2415	2.034
B1	1-1/2	29.0	11	2.900	2.90	.2271	.1747	1.080
B2	1-1/2	25.0	9	3.214	2.50	.2517	.1506	.829
B3	1-1/2	20.0	7	3.600	2.00	.2819	.1204	.572
B4	1-1/2	14.0	6	3.150	1.40	.2467	.0843	.344

Results of the beams made with the 2-1/2 inch pipe are presented in Figures 19 through 32, followed by data of beams made with the 1-1/2 inch pipe in Figures 33 through 37.

In Figure 19, the tip displacements of beams A1, A2, A3, and A4 are shown. The design method does give an even distribution of maximum displacement. Furthermore, secondary peaks occur in decreasing magnitude with increasing frequency among the beams. The maximum displacement is shown to be a strong function of natural frequency because the first peak occurs between 1.15 and 1.6 quarter periods from initial impulse.

Figure 20 shows the tip mass rotation for each beam of set A. The maximum tip mass rotation is also well spread like the displacements. However, small oscillations resulting from the initial wave front being reflected back and forth along the beam are eventually dissipated.

The tip mass acceleration, $\ddot{y}_n$, is presented in Figure 21 for the longest and shortest beams A1 and A4 respectively. The peak acceleration of A1 is much smaller because of its large inertia. The transient responses of both masses are quickly damped through plastic deformation and they begin to oscillate at their natural frequencies.

Figure 22 presents the curvature at the support versus time. Two things are interesting about these data:

(1) the maximum curvature is nearly the same for all beams except A4, and

(2) an initial plastic deformation occurs at approximately two milliseconds.

The initial permanent set at the base is probably due to the sharp rise time of the base velocity since this was not observed by Vogel (22).

The moment-time relations at the fixed end are presented in Figure 23. Corresponding to the curvature, an initial large moment is observed. The moment then oscillates about the yield point, then changes sign when the tip mass nears the second peak displacement. The moment is higher for the smallest beam, A4.

Figures 24 and 25 are presented in order to show all the loads that act on the support. Only data for beams A1 and A2 are given, however, a complete tabulation of maximum loads and displacements are given in Table 4. Sharp initial shear forces are observed and are quickly damped.

Next, moment curvature curves at station 1 are presented for beams A1, A2, A3, and A4. Figures 26, 27, 28, and 29 show an initial unloading followed by several periodic unloadings. The curvature finally reverses sign when the tip mass changes direction. Notice the small time delay between the maximum moment and maximum curvature caused by the large value of C.

All of the above curves are timewise views of the output. Figures 30 and 31 show a spanwise view of beam A2. In Figure 30, the curvature at the support is seen to dominate the total beam deformation. Even though some permanent deformation does occur at other points on the beam, it is small compared to the deformation near the support. Figure 31 shows the curvature rate at the fixed end

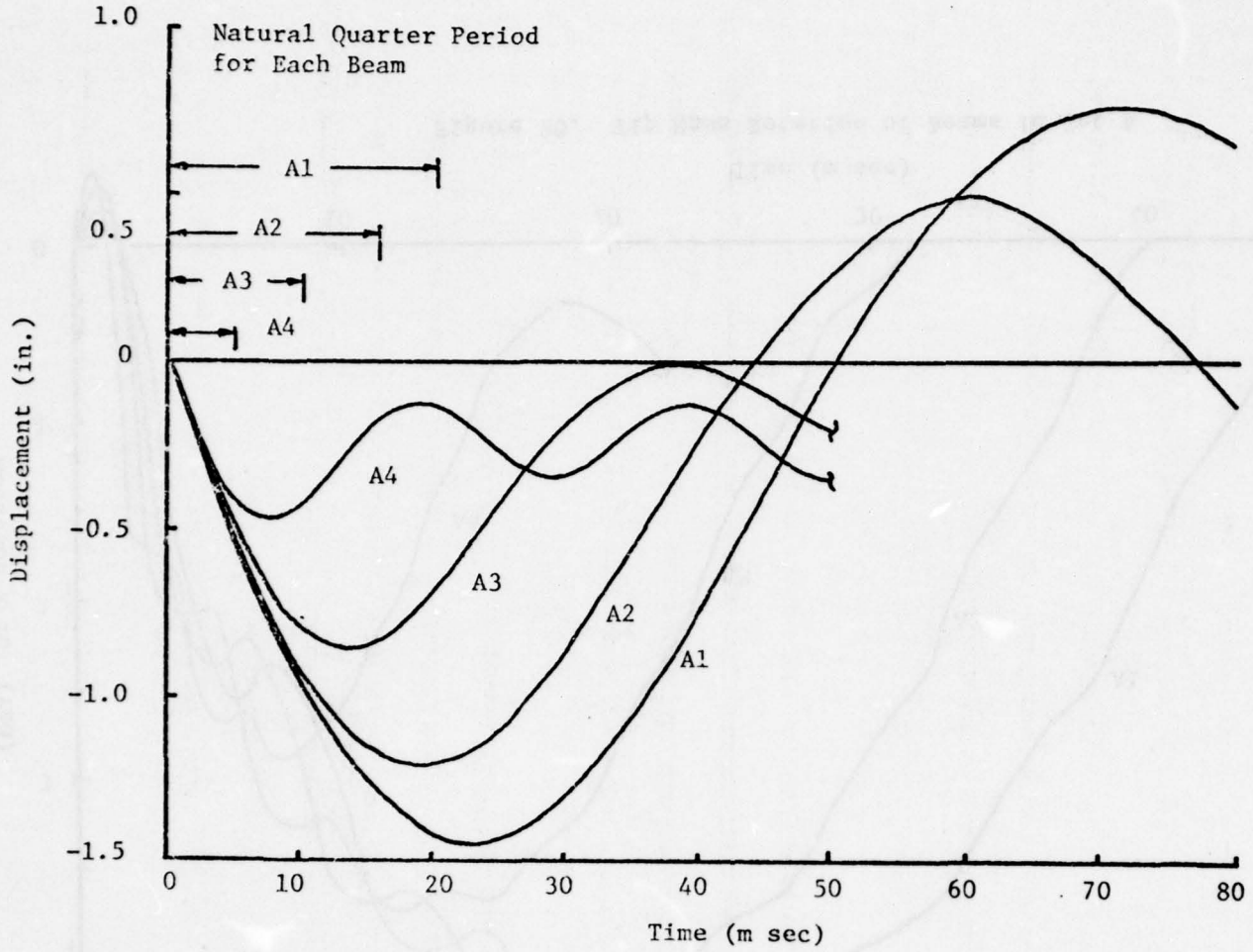

Figure 19. Tip Mass Displacements of Beams in Set A

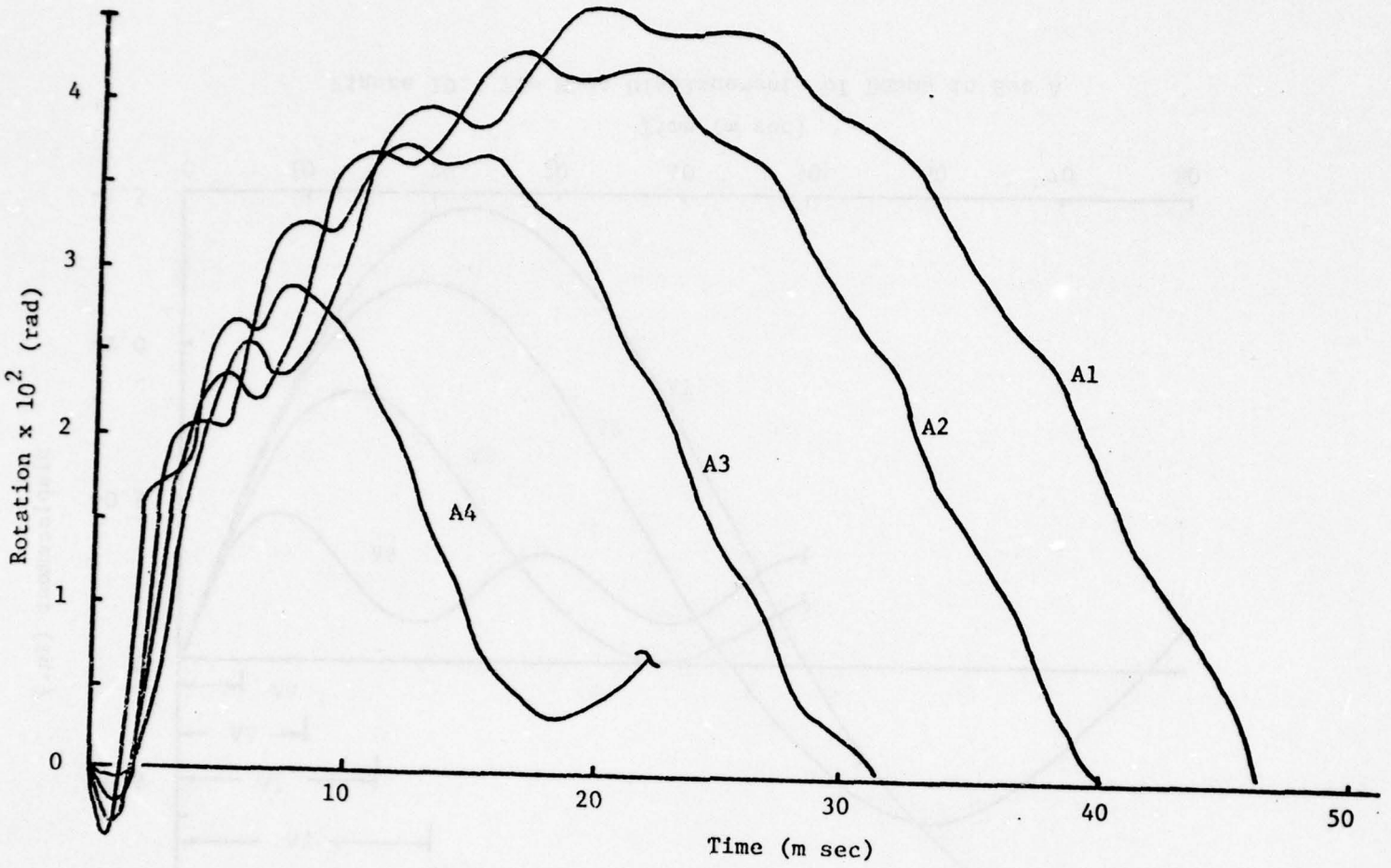

Figure 20. Tip Mass Rotation of Beams in Set A

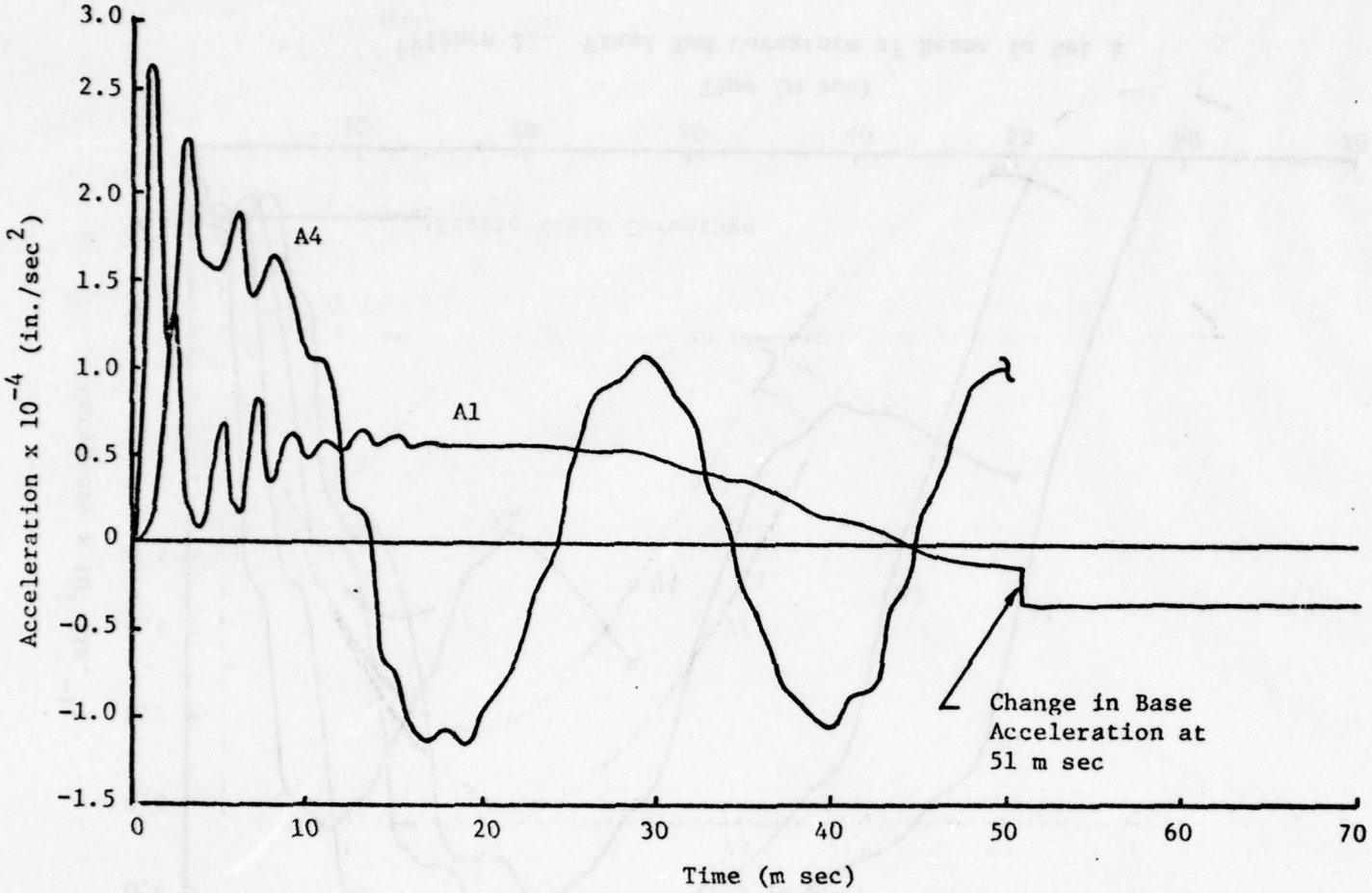

Figure 21. Tip Mass Acceleration of Beams A1 and A4

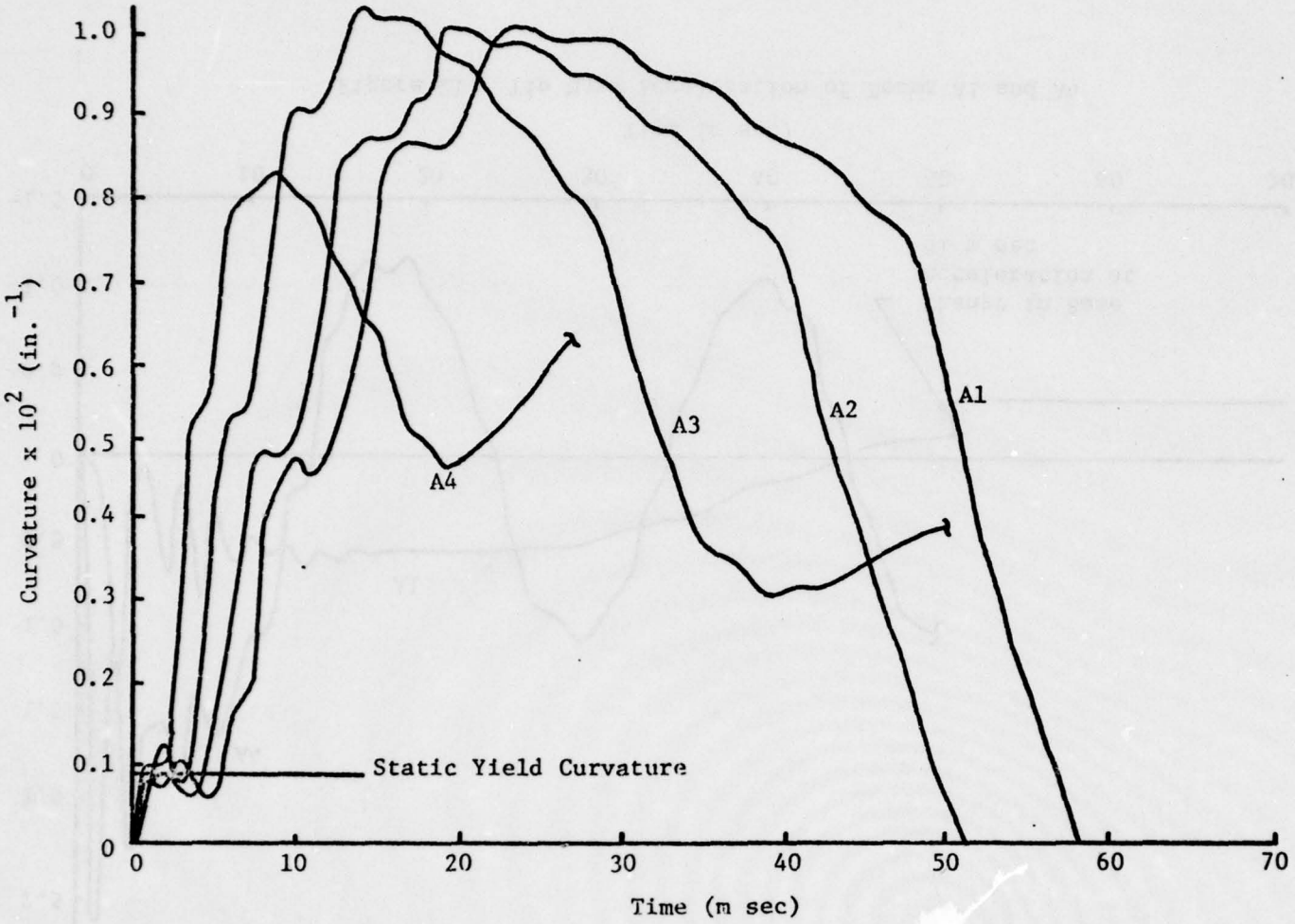

Figure 22. Fixed End Curvature of Beams in Set A

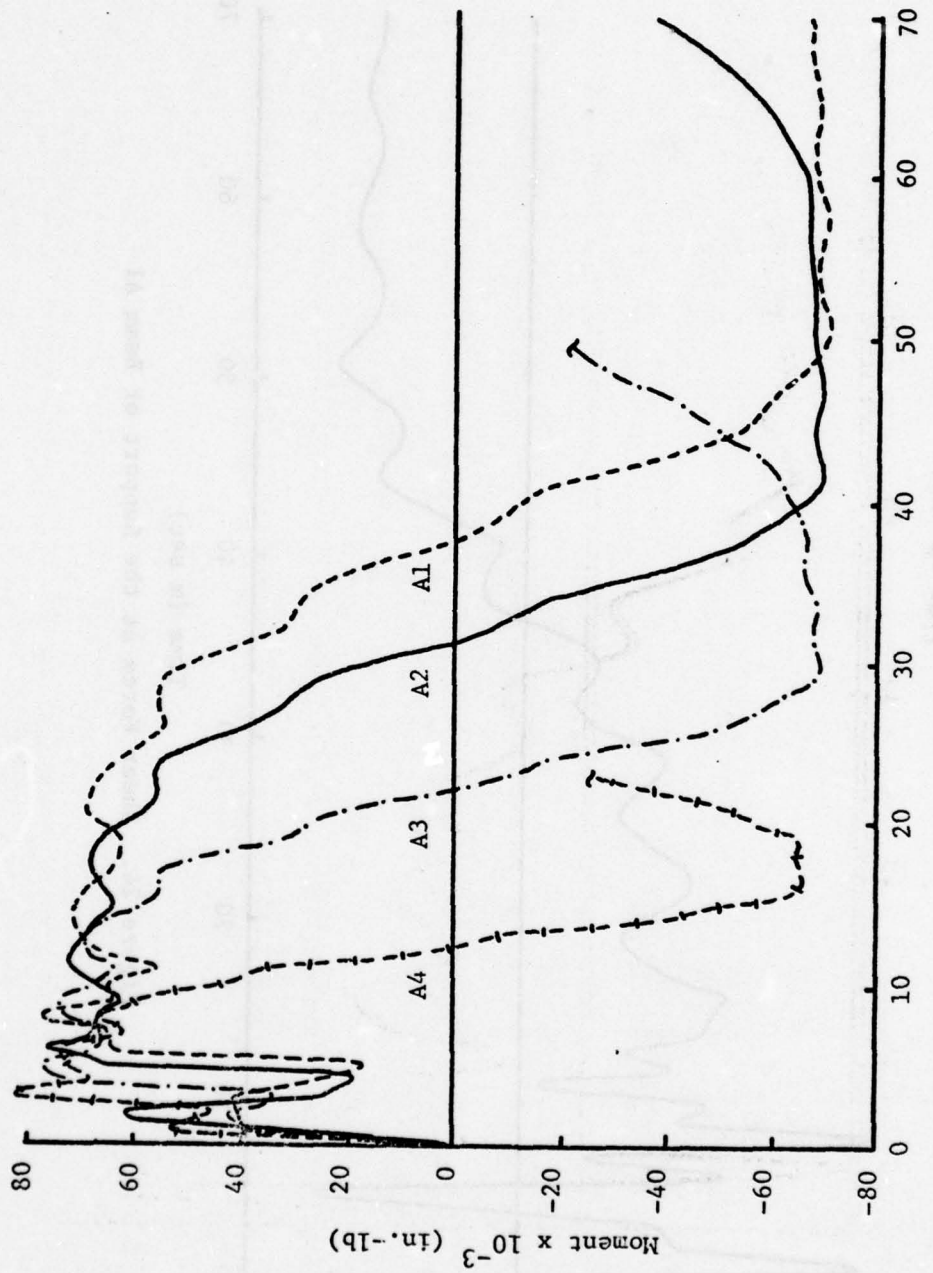

Figure 23. Fixed End Dynamic Moment of Beams in Set A

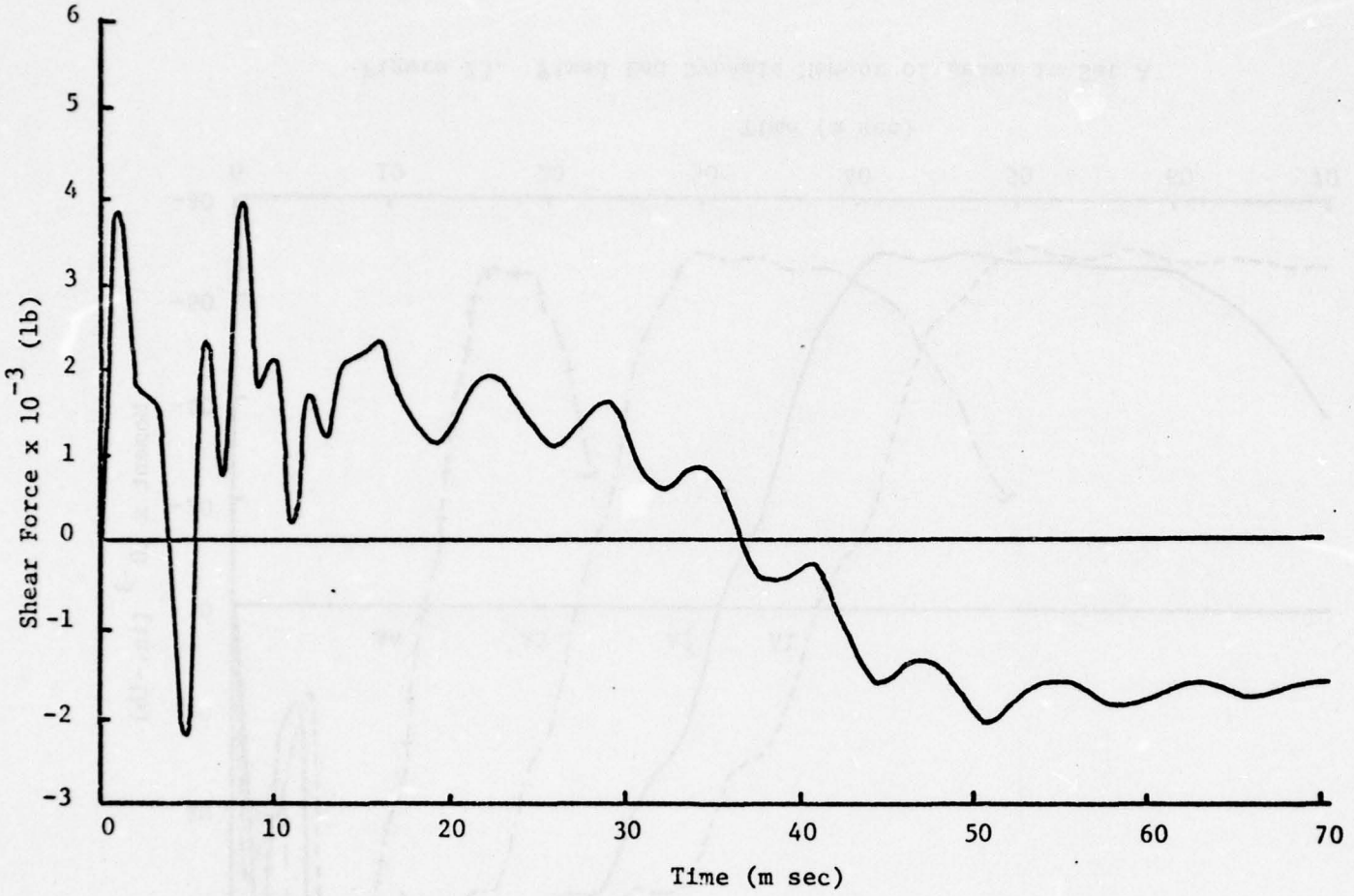

Figure 24. Shear Force at the Support of Beam A1

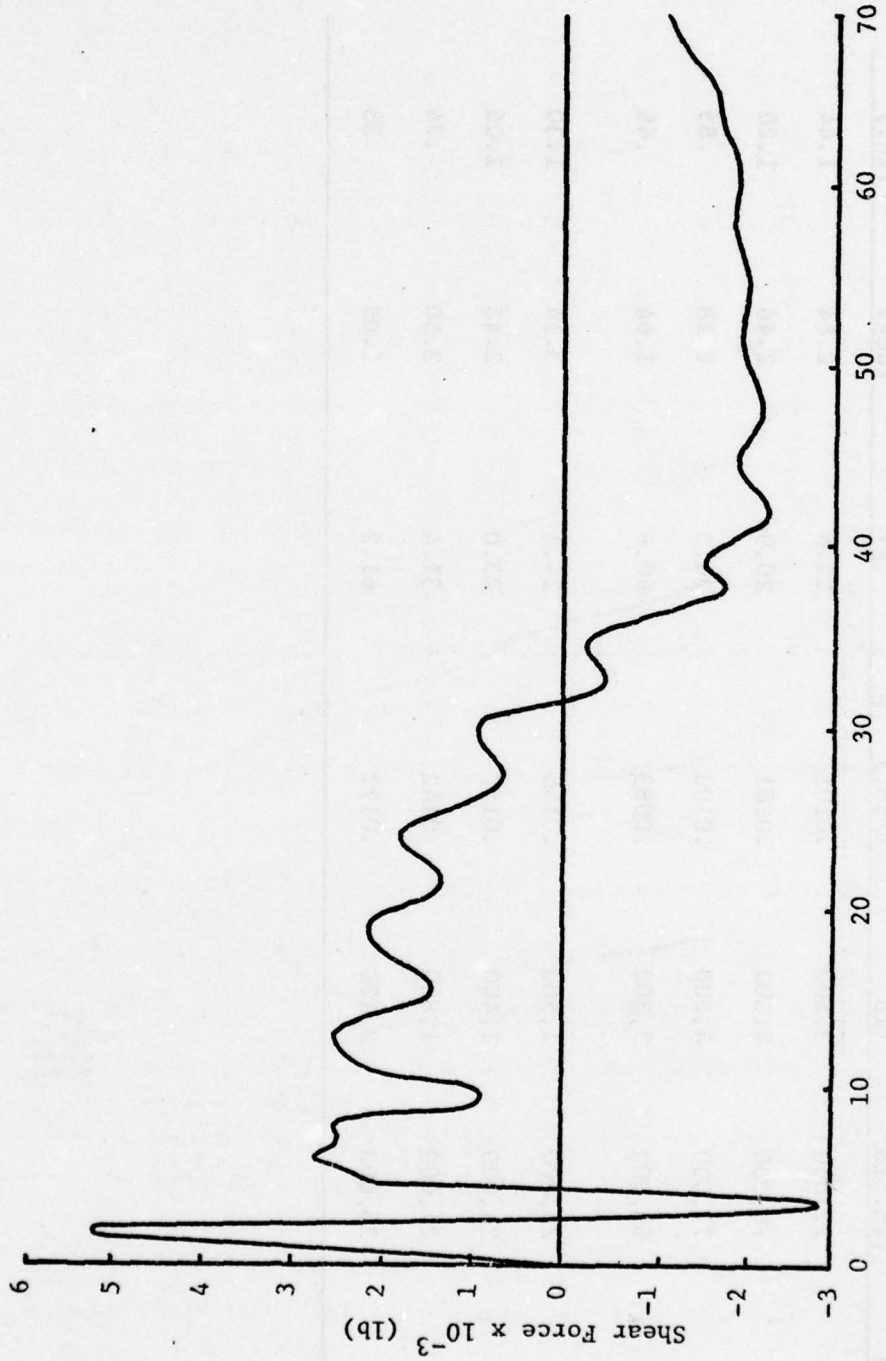

Figure 25. Shear Force at the Support of Beam A2

Table 4. Maximum Values

Beam	Maximums at Support			Maximums at Tip		
	Moment (in. lb)	Shear (lb)	Curvature (1/in.)	Acceleration (g)	Rotation (deg)	Deflection (in.)
A1	77,000	3,800	.0101	21.6	2.64	1.44
A2	76,000	5,300	.0101	20.9	2.46	1.20
A3	77,000	4,200	.0103	30.3	2.18	.85
A4	83,000	5,300	.0083	60.6	1.64	.46
B1	22,000	1,500	.0156	24.1	3.14	1.30
B2	24,000	1,400	.0157	23.0	2.46	1.06
B3	24,000	1,800	.0142	31.4	2.50	.74
B4	23,000	2,100	.0127	61.2	1.89	.38

and at a point near the mid-span. A phase shift in the two curves is evidence of reflected waves in the beam.

A comparison of the beam design with the actual results is made in Figure 32. A shock spectrum is presented for the relatively small frequency range for which the beams were designed. The solid line represents the values of penetration, η, expected from the design of the beams. If the value of η is based on the static yield displacement, the results are considerably different as given by the dashed line. As shown in Figure 22, however, the beam does not deform under the action of an impulse as it would if a static load were applied. In fact, an initial plastic deformation occurs at nearly the same tip displacement for all the beams. Therefore, basing the value of η on a dynamic yield displacement (i.e., the tip deflection at which initial plastic deformation occurs anywhere on the beam) causes the results to compare favorably with the initial design value as indicated by the broken line.

In Figures 33 through 37, data from the beams made with 1-1/2 inch pipe is presented for comparison. The tip mass displacements of Figure 33 are similar to those in Figure 19 for the 2-1/2 inch pipe. The magnitude of the maximum displacements, in fact, are quite close for beams with the same design value of η.

The maximum curvatures in Figure 34 are approximately 1.5 times those for the 2-1/2 inch pipe. A direct comparison is made in Figure 35. The quicker return of the curve for beam B2 is due to its slightly higher frequency.

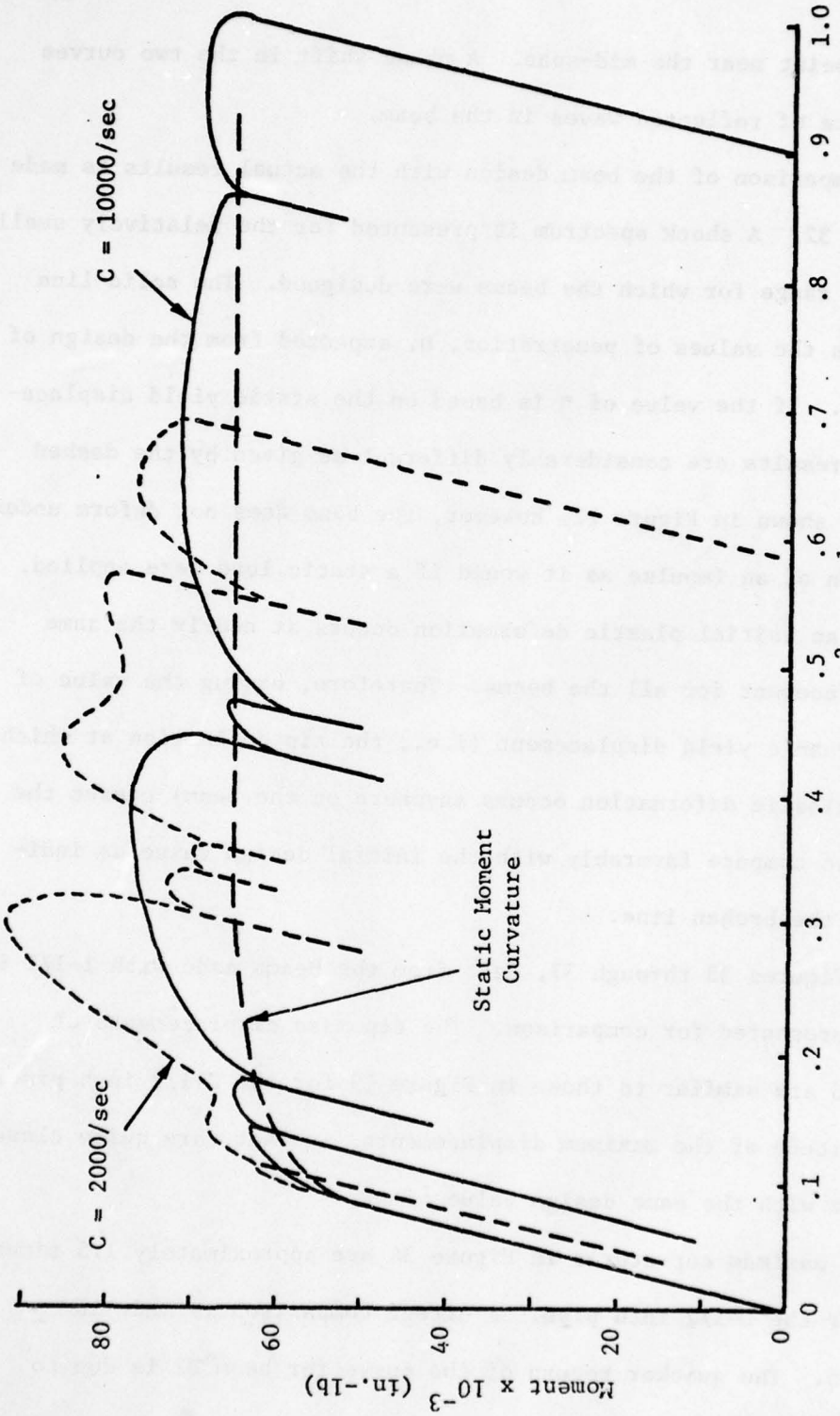

Figure 26. Moment Curvature Relation of Beam A1

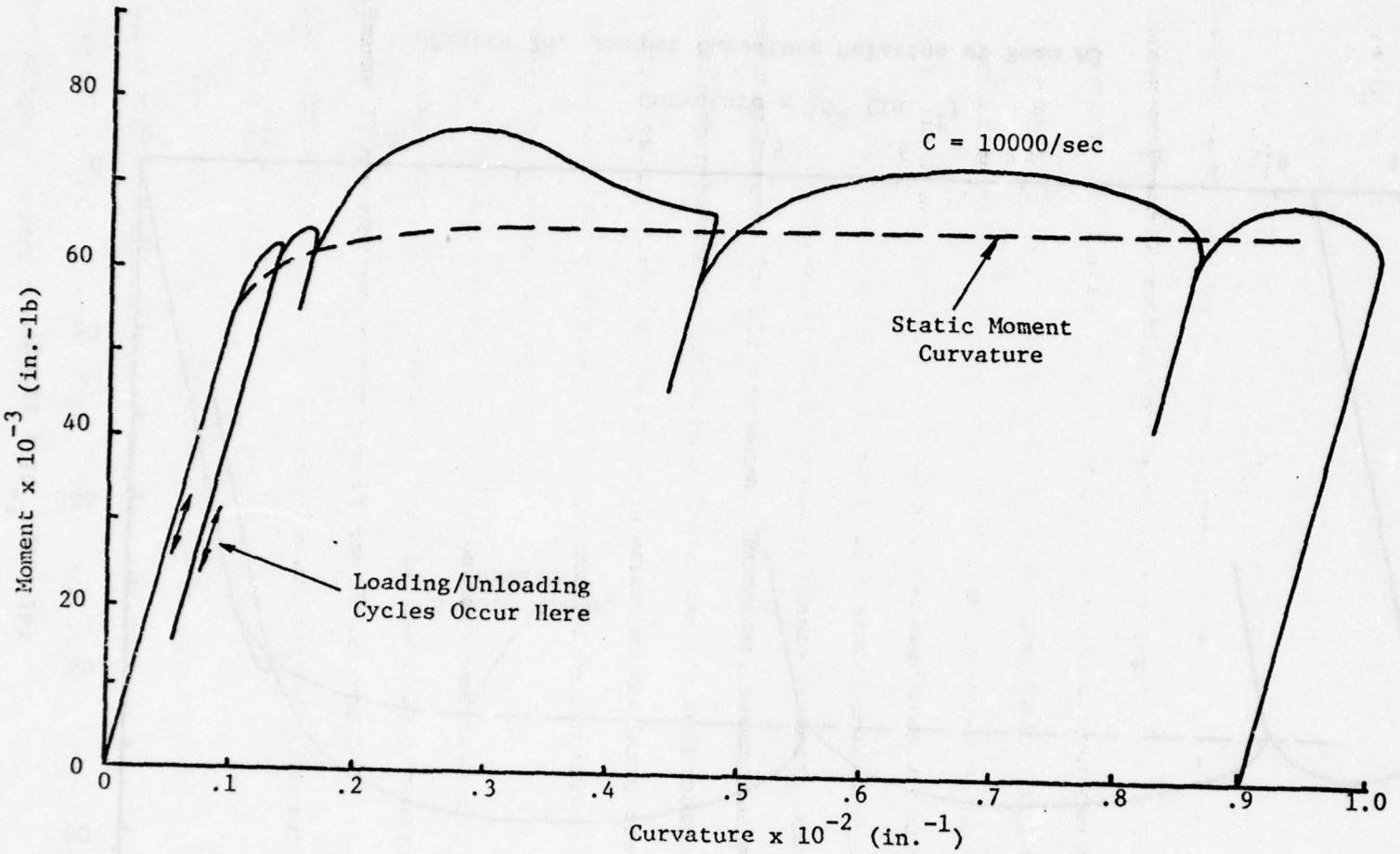

Figure 27. Moment Curvature Relation of Beam A2

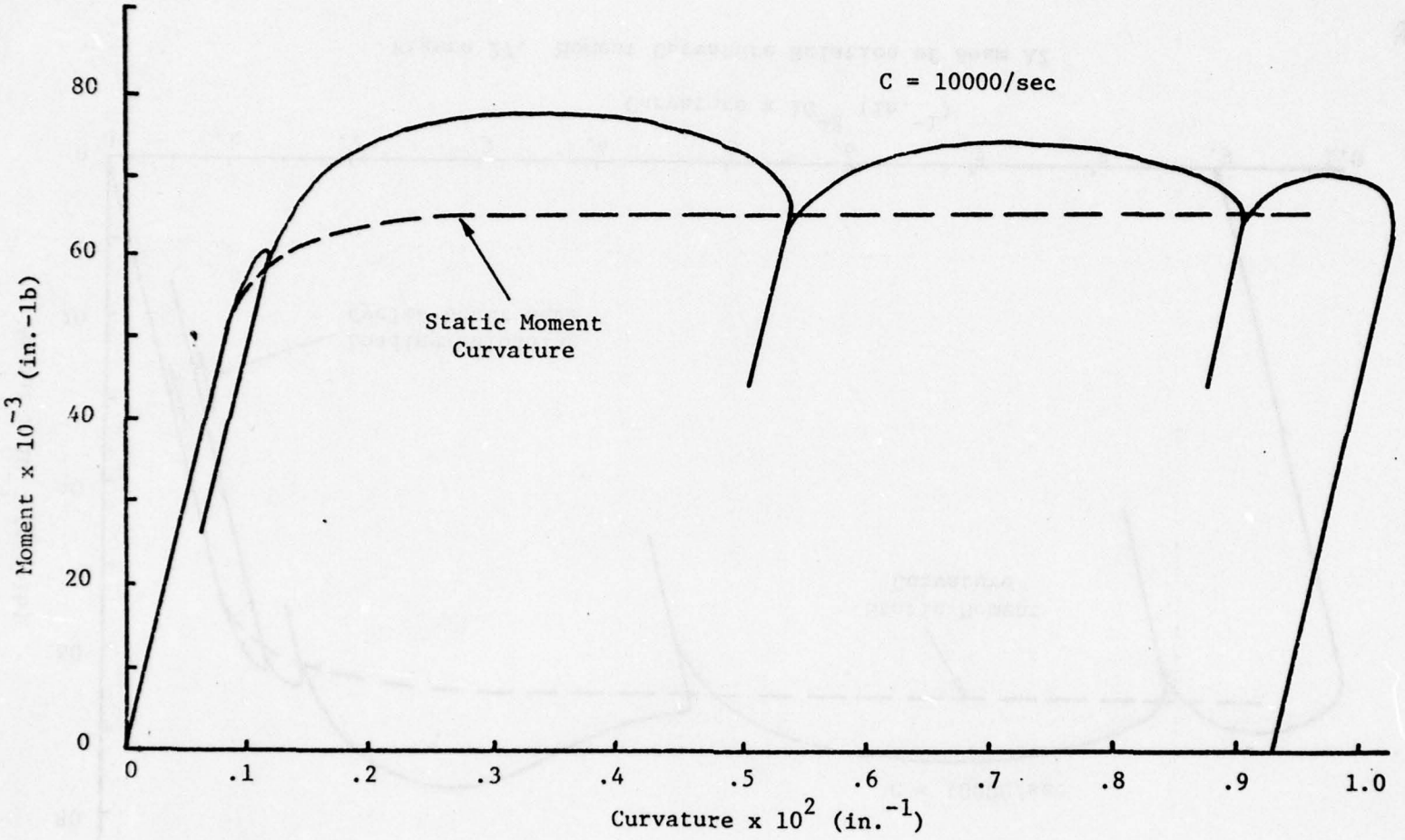

Figure 28. Moment Curvature Relation of Beam A3

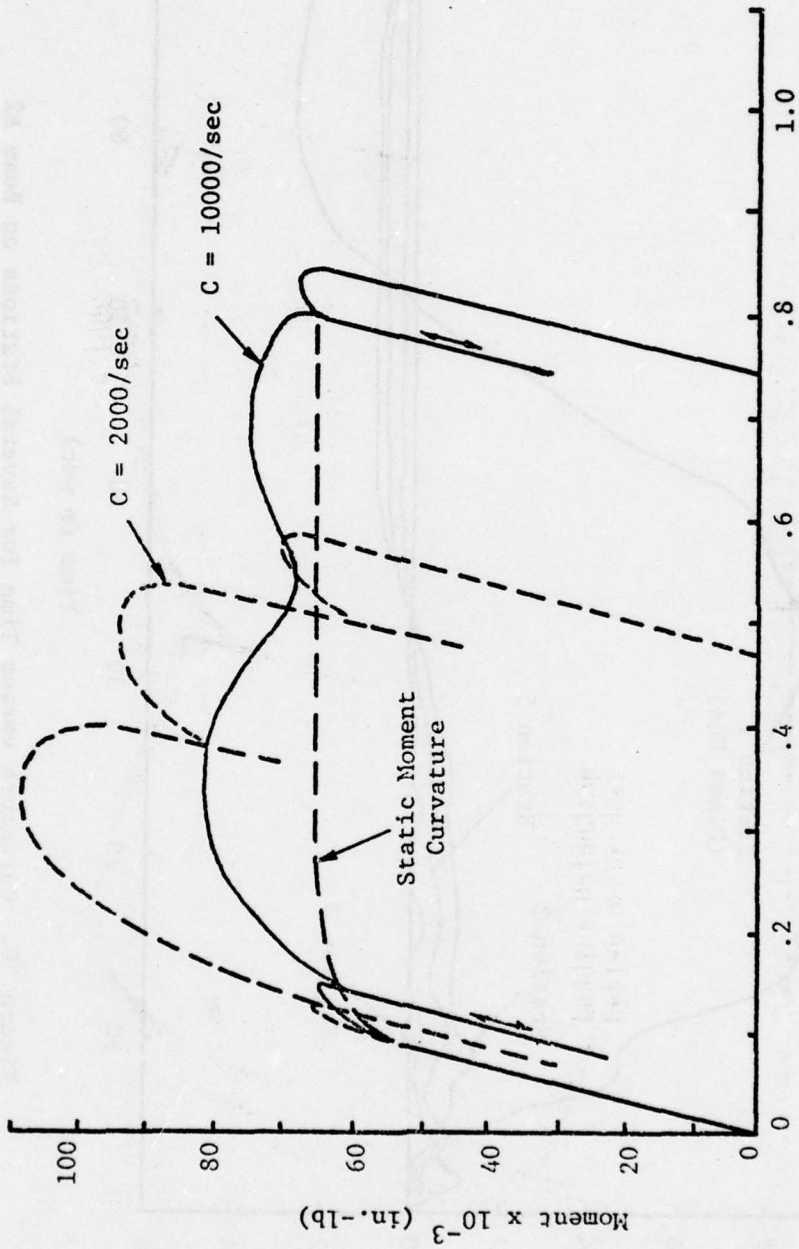

Figure 29. Moment Curvature Relation of Beam A4

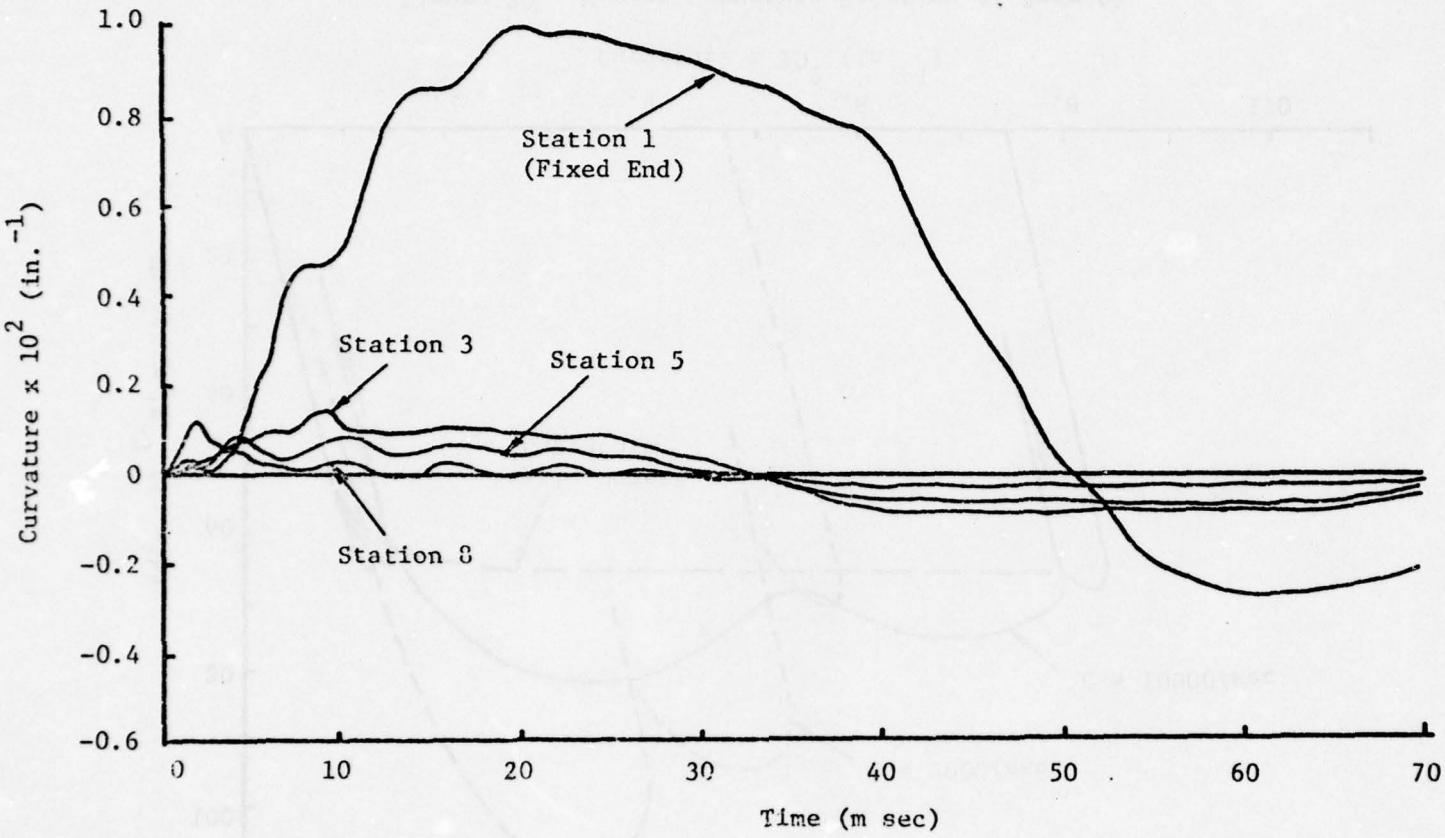

Figure 30. Curvature versus Time for Several Stations on Beam A2

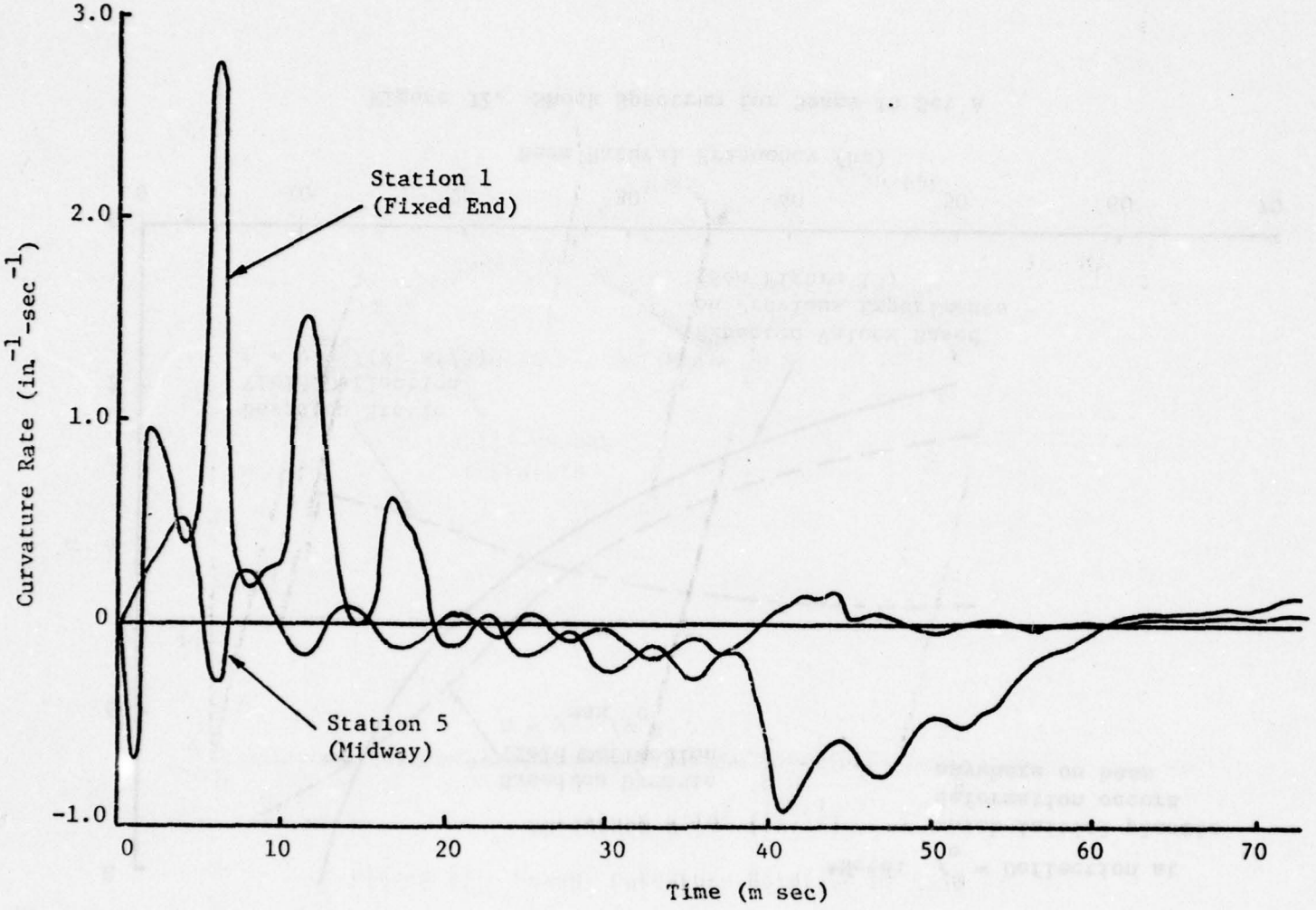

Figure 31. Curvature Rates for Stations 1 and 5 on Beam A2

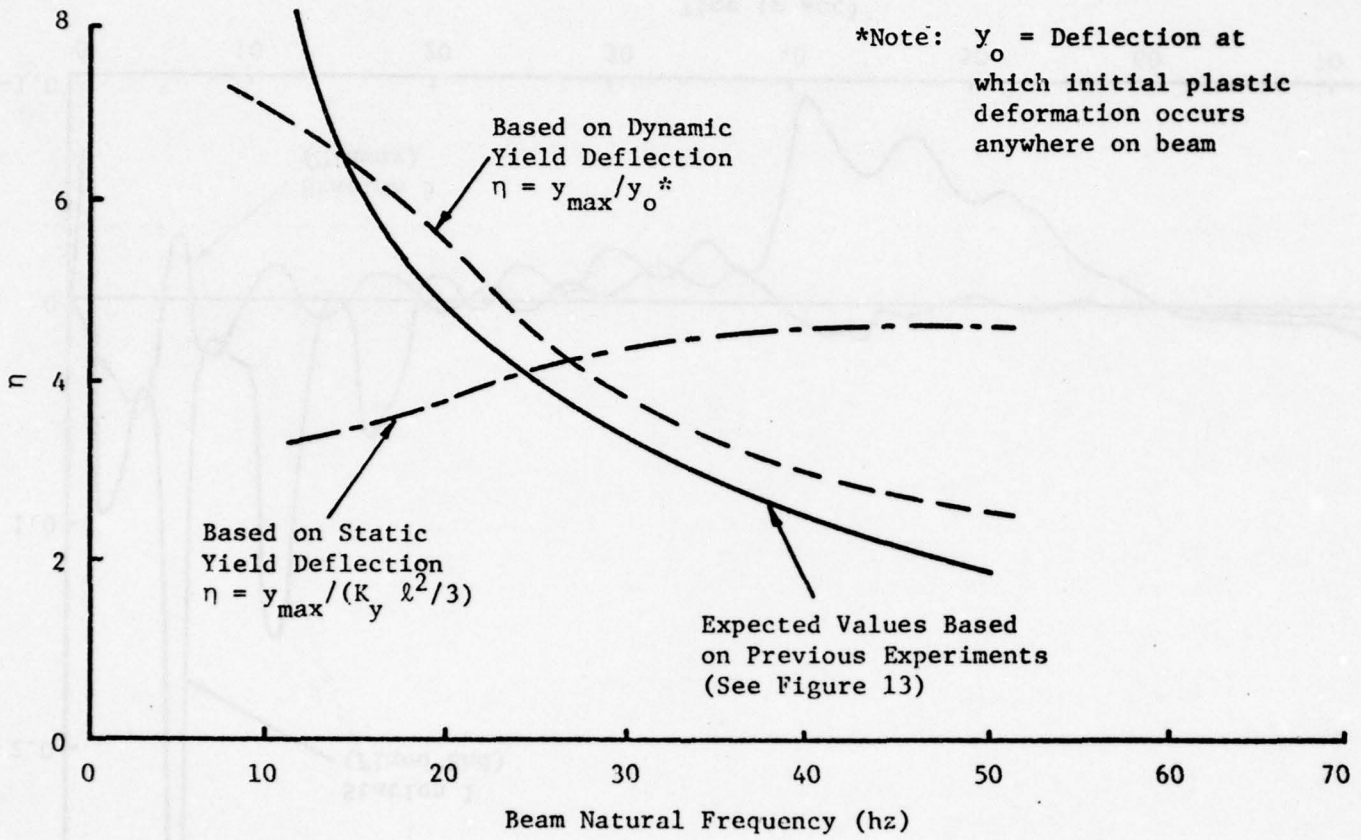

Figure 32. Shock Spectrum for Beams in Set A

The base moments for beams A2 and B2 are shown in Figure 36. Although the waveforms are similar, the moment in beam B2 is always smaller because of the smaller cross section.

Finally in Figure 37, the tip mass rotations for beam A2 and B2 are shown to be similar. The small reverse rotation exhibited by both beams is caused by the initial wave reaching the tip mass. Beam B2 shows slightly larger maximum rotation because of the smaller rotational flexibility of the tip and a smaller moment of inertia.

The beams of sets A and B are quite different in length, cross sectional size, and tip mass; yet the results show a close similarity. Only small frequency and stiffness effects affect the comparison of the results. These results seem to verify the intention of the design: to predict a significant plastic deformation of these beams before a detailed analysis is made.

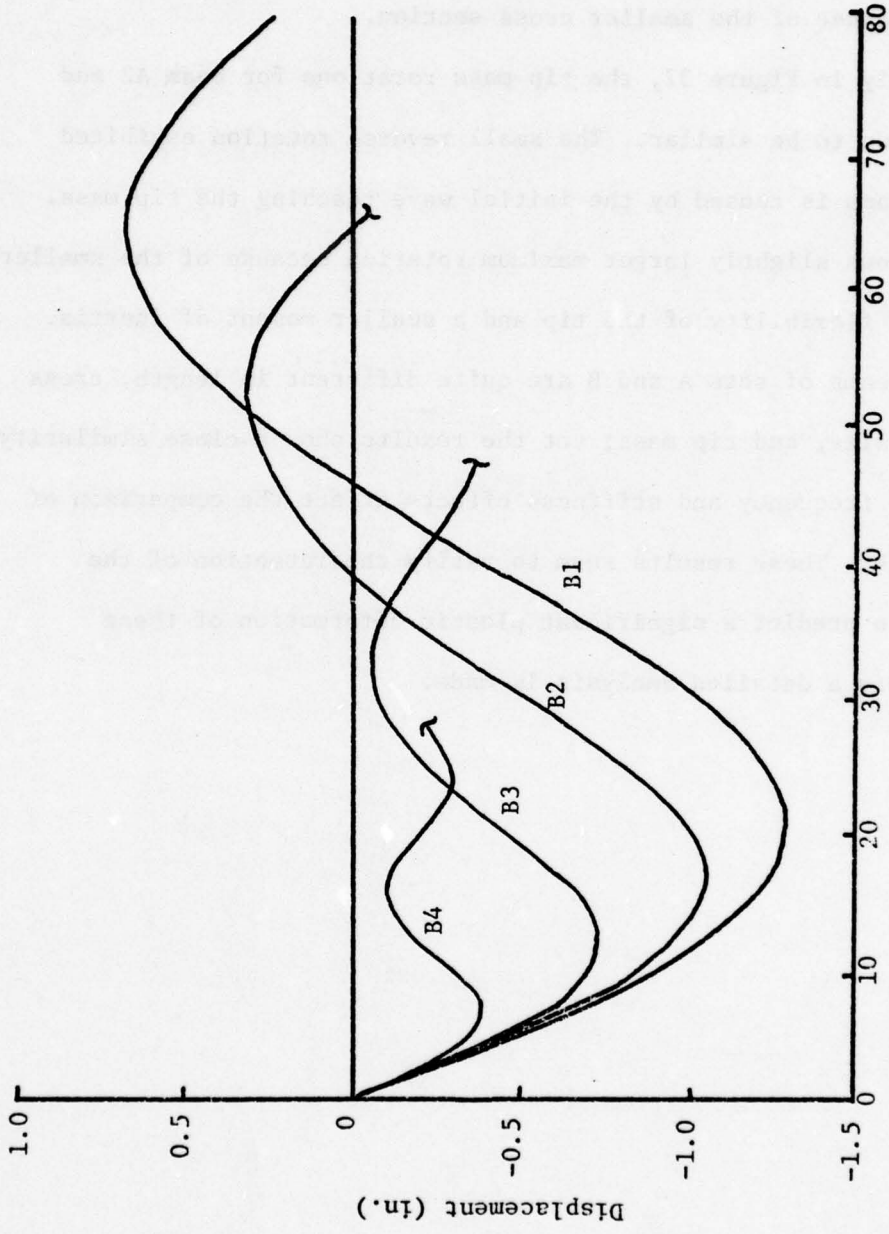

Figure 33. Tip Mass Displacements for Beam in Set B

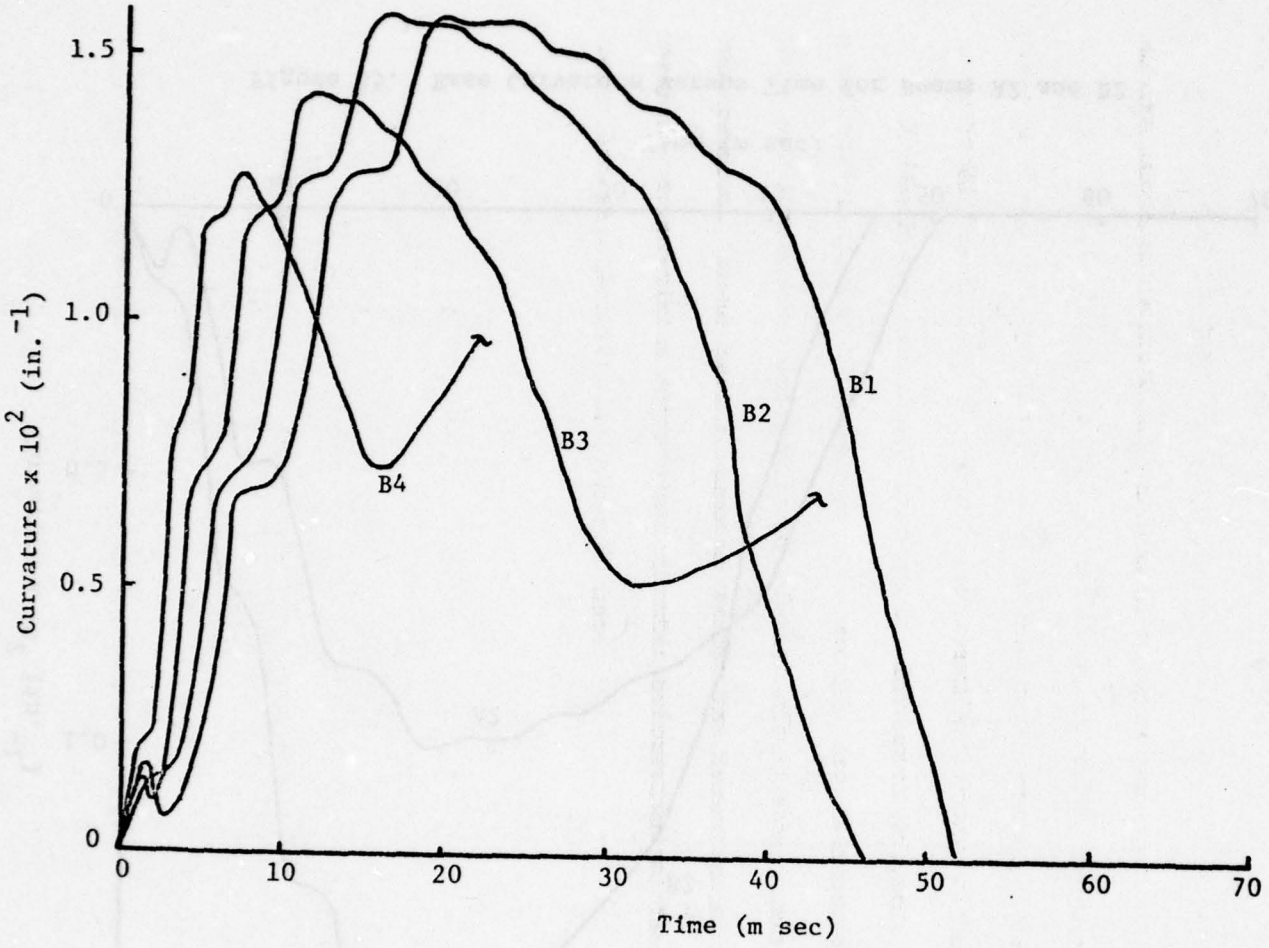

Figure 34. Fixed End Curvature for Beams in Set B

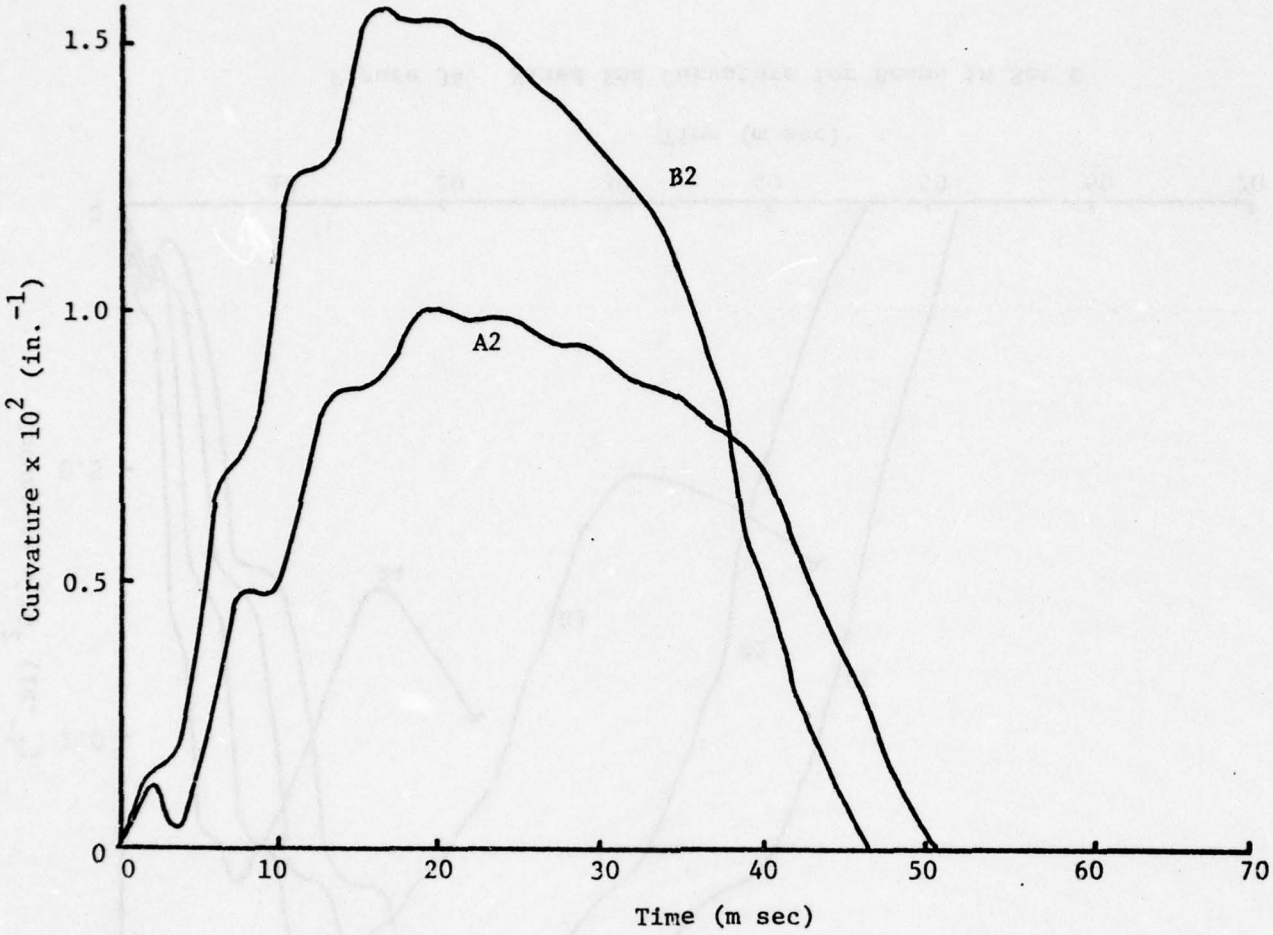

Figure 35. Base Curvature versus Time for Beams A2 and B2

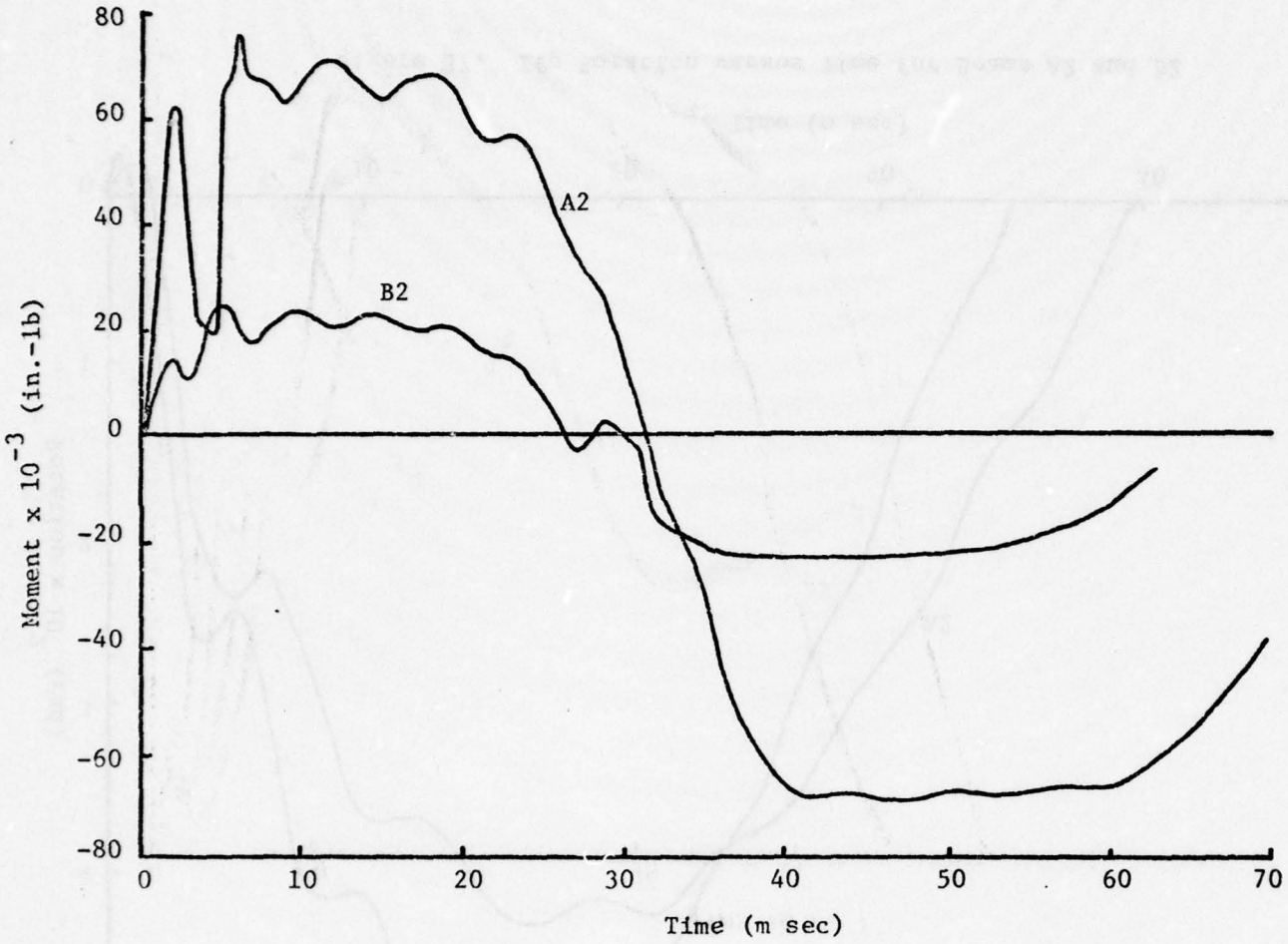

Figure 36. Base Moment versus Time for Beams A2 and B2

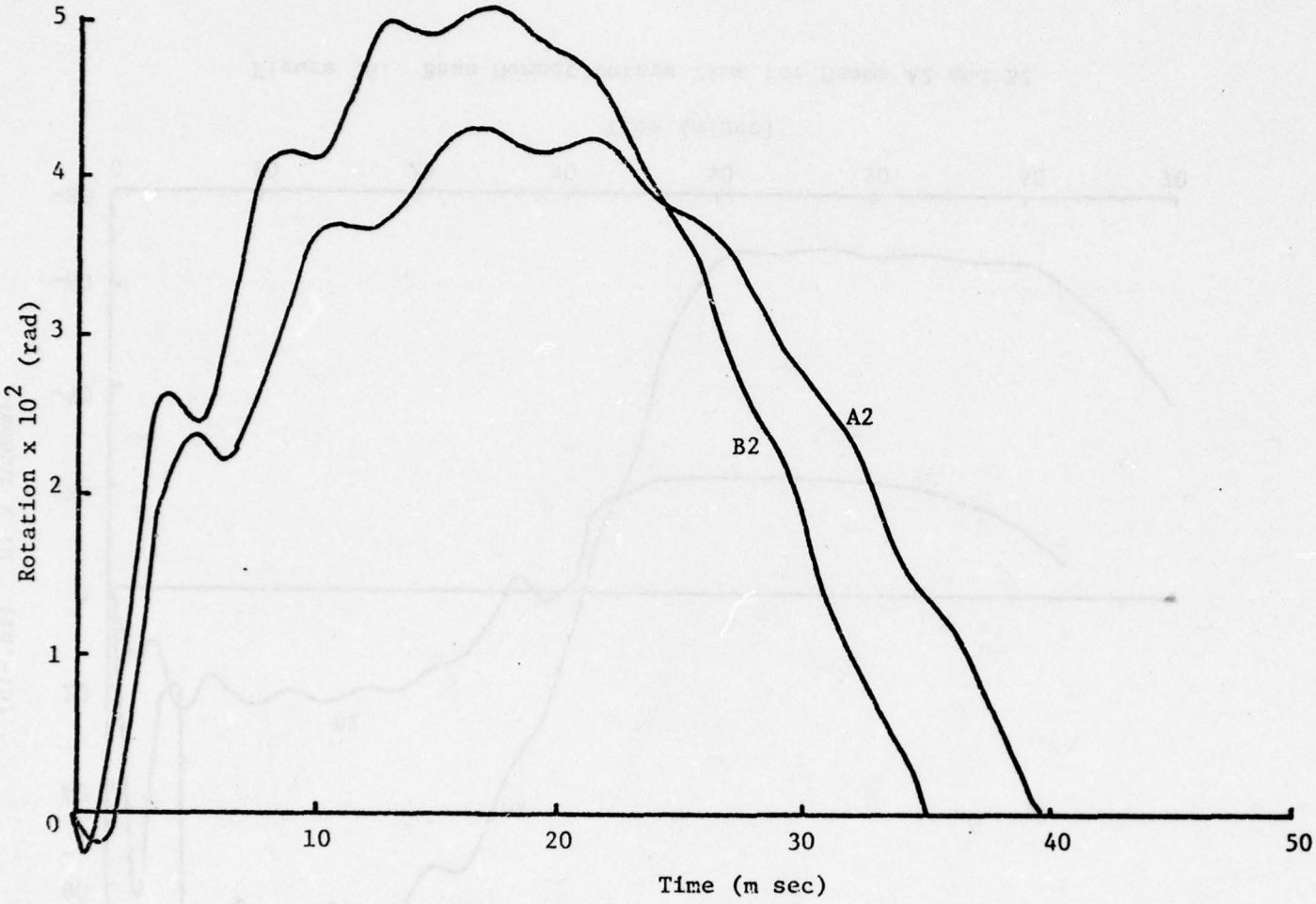

Figure 37. Tip Rotation versus Time for Beams A2 and B2

CHAPTER 5

SUMMARY AND CONCLUSIONS

5.1 Summary

A finite difference computer method for analyzing the dynamic response of cantilever beams having any applied velocity or acceleration function at the base is developed and checked with experimental data. Viscoplastic effects are included through the use of a constitutive equation suggested by Malvern (10). The program is then used to investigate a set of beams with hollow circular cross sections, designed by an empirical method based on a variety of tests on cantilever beams. The beams are designed to achieve a specified amount of deformation. The results are then compared.

5.2 Conclusions

The method of analysis developed is shown to be adequate in predicting the response of beams under the impact of any input loading function. Agreement with experimental and analytical data presented in Chapter 3 verifies the equations and methods used in this analysis and lend credibility to the data presented in Chapter 4.

The constitutive equation is shown to be adequate in determining the beam deformation but needs improvement in order to accurately predict the internal loads. It does produce similar trends and approximate magnitudes but more work is needed in order to calculate the internal loads properly.

The design method presented in Chapter 4 was adequate in predicting a shock spectrum based on dynamic yielding. The beams

designed by this method achieved plastic deformation well beyond the yield point as expected. The effect of reflected waves was pronounced on the base curvature of the beam causing an initial set early in the beam response. This was due primarily to the small rise time from the base velocity input used on all of the beams.

Finally, the responses of beam sets designed with 1-1/2 inch pipe and 2-1/2 inch pipe were remarkably similar for the same design value of penetration. Only small frequency effects were evident in the comparison of beam deformations.

5.3 Suggestions for Further Research

Certainly more work is needed in the development of a constitutive equation that accurately determines internal loads. This must come from basic research in the phenomenon of viscoplasticity. Until that time the constitutive equation used in this study is accurate in predicting displacements, slopes and curvatures, and gives quantitative values for internal loads.

The test outlined theoretically in Chapter 4 should be carried out in order to determine shock damage of piping networks. Two sets of pipe are analyzed in order to allow flexibility in determining an acceptable test arrangement.

Finally, work should begin toward a finite element type viscoplastic program to analyze any structure--similar to those used in elastic analysis today. Most programs to date have simply analyzed single element structures (i.e., straight beams, single shells, rings, or plates). None have combined these elements to form models of a

realistic structure. The task indeed is formidable, however, the direction of viscoplastic analysis must be toward this goal.

BIBLIOGRAPHY

1. Bodner, S. R., and Symonds, P. S., "Experimental and Theoretical Investigation of the Plastic Deformation of Cantilever Beams Subjected to Impulsive Loading," Transactions ASME, Journal of Applied Mechanics, Volume 29, pp. 719-728, 1962.

2. Brown, W. G., Dynamic Properties of Beams of Cold Rolled Steel, Masters Thesis, Department of Engineering Mechanics, The Pennsylvania State University, September 1967.

3. Butt, L. T., Short, R. D., and Thornton, E. A., "Shock Damage Mechanism of a Simple Structure," Research and Development Report No. 2197, Department of the Navy, Structural Mechanics Laboratory, Underwater Explosions Research Division, March 1967.

4. Chen, Tu-Tsai, "Some Basic Problems in Viscoplasticity," Doctoral Thesis, Department of Engineering Mechanics, The Pennsylvania State University, June 1968.

5. Conroy, M. F., "Plastic-Rigid Analysis of Long Beams Under Transverse Impact Loading," Transactions ASME, Journal of Applied Mechanics, Volume 74, Part 2, pp. 465-470, 1952.

6. Duwez, P. E., Clark, D. S., and Bohnenblust, H. F., "The Behavior of Long Beams Under Impact Loading," Transactions ASME, Journal of Applied Mechanics, Volume 17, pp. 27-34, 1950.

7. Frick, T. M., and Neubert, V. H., "An Experimental Study of the Viscoplastic Bending of Copper-Nickel and Steel Tubing," Office of Naval Research, Contract No. N00014-67-A-0385-0010, Progress Report No. 4, June 1973.

8. Jones, Norman, "Influence of Strain-Hardening and Strain-Rate Sensitivity on the Permanent Deformation of Impulsively Loaded Rigid-Plastic Beams," International Journal of Mechanical Sciences, Volume 9, pp. 777-796, 1967.

9. Lee, E. H., and Symonds, P. S., "Large Plastic Deformations of Beams Under Transverse Impact," Transactions ASME, Journal of Applied Mechanics, Volume 74, pp. 308-314, 1952.

10. Malvern, L. E., "The Propagation of Longitudinal Waves of Plastic Deformation in a Bar of Material Exhibiting a Strain-Rate Effect," Transactions ASME, Journal of Applied Mechanics, June 1951, Volume 73, pp. 203-207.

11. Mentel, T. J., "The Plastic Deformation due to Impact of a Cantilever Beam with an Attached Tip Mass," Transactions ASME, Journal of Applied Mechanics, Volume 80, Part 2, pp. 515-524, 1958.

12. Neubert, V. H., "Dynamic Response of Viscoplastic Beams," Office of Naval Research, Contract No. N00014-67-A-0385-0010, Progress Report No. 3, August 1972.

13. Neubert, V. H., "Stiffness Matrix for a Viscoplastic Beam Element," Shock Analysis of Structural Systems, Office of Naval Research, Interim Report No. 9, February 1970.

14. Neubert, V. H., "Time Delay for Elastic-Viscoplastic Materials," Shock Analysis of Viscoplastic Beams, Office of Naval Research, Contract No. N00014-75-C-0759, Progress Report No. 1, December 1975.

15. Perrone, Nicholas, "On a Simplified Method for Solving Impulsively Loaded Structures of Rate-Sensitive Materials," Transactions ASME, Journal of Applied Mechanics, Vol. 87, pp. 489-492, 1965.

16. Plass, H. J., "Theory of Plastic Sending Waves in a Bar of Strain-Rate Material," Proceedings Second Midwest Conference on Solid Mechanics, Purdue University, pp. 109-134, 1955.

17. Shieh, R. C., "Large Displacement Matrix Analysis of Elastic/Viscoplastic, Plane Frame Structures," Publication ASME, Paper No. 75-DET-37, 1975.

18. Stanovsky, J. J., The Shock Response of Beams with Non-Linear Material Properties, Doctoral Thesis, Department of Engineering Mechanics, The Pennsylvania State University, August 1966.

19. Structural Alloys Handbook, Mechanical Properties Data Center, Wrought Steel, Volume I, 1976.

20. Symonds, P. S., and Jones, Norman, "Impulsice Loading of Fully Clamped Beams with Finite Plastic Deflections and Strain-Rate Sensitivity," International Journal of Mechanical Sciences, Volume 14, pp. 49-69, 1972.

21. Ting, Thomas C. T., "The Plastic Deformation of a Cantilever Beam with Strain-Rate Sensitivity Under Impulsive Loading," Transactions ASME, Journal of Applied Mechanics, Vol. 31, pp. 38-42, 1964.

22. Vogel, W. H., The Dynamic Response of a Viscoplastic Beam, Doctoral Thesis, Department of Engineering Mechanics, The Pennsylvania State University, June 1971.

23. Weiss, R. S., Theoretical Dynamic Response of an Electric-Viscoplastic Cantilever Beam, Doctoral Thesis, Department of Engineering Mechanics, The Pennsylvania State University, March 1974.

24. Witmer, E. A., Balmer, H. A., Leech, J. W., and Pian, T. H., "Large Dynamic Deformations of Beams, Rings, Plates, and Shells," American Institute of Aeronautics and Astronautics, Volume 1, No. i, pp. 1848-1857, 1963.

25. Witmer, E. A., Wu, R. W. H., and Merlis, F., "Experimental Transient and Permanent Deformation Studies of Impulsively-Loaded Rings and Cylindrical Panels, Both Stiffened and Unstiffened," Army Materials and Mechanics Research Center, Interim Report, Contract No. DAAG46-72-C-0212, April 1974.

26. Yim, S. J., and Neubert, V. H., "Shock Analysis of Viscoplastic Beams," Office of Naval Research, Contract No. N00014-75-6-0759, Progress Report No. 1, December 1975.

27. Yim, S. J., "A Theoretical Study of Viscoplastic Bending of Rectangular and Box Beam Cross-Sections, Masters Thesis, Department of Engineering Mechanics, The Pennsylvania State University, June 1974.

28. Gatchel, Stanley G., "A Theoretical Study of the Dynamic Response of Viscoplastic Beams with Hollow Circular Cross Sections," Master of Science Thesis, Department of Engineering Science and Mechanics, The Pennsylvania State University, November, 1976.

APPENDIX A

STATIC MOMENT

A.1 Introduction

One of the problems that makes analysis of viscoplastic structures so formidable is that deformation depends not only on the instantaneous conditions of the beam, but also on the previous loading or "loading history" of the beam. In this study such information is included through determination of the internal static moment.

A.2 Problem Formulation

The problem of determining the internal static moment at any station, i, along the beam and for any time, t, during the loading cycle may be divided into four parts:

1. A test for loading and unloading,
2. Finding the static moment from the original curve with origins at zero,
3. A means of retaining the essential information of the loading history of the beam, and
4. Using the above data to find the static moment at any time.

A.3 Effect of Loading on Static Moment Curvature Curve

The moment-curvature curve can be thought of initially as an upper curve and a lower curve symmetrical about the origin as shown in Figure 38. The location of the origins of these curves is K_{UO} and K_{LO}; both initially zero. If loading continues beyond the proportional limit, P, to some point C', then a permanent curvature, K_O, exists in the beam and a new value for yield curvature K_y^U is set

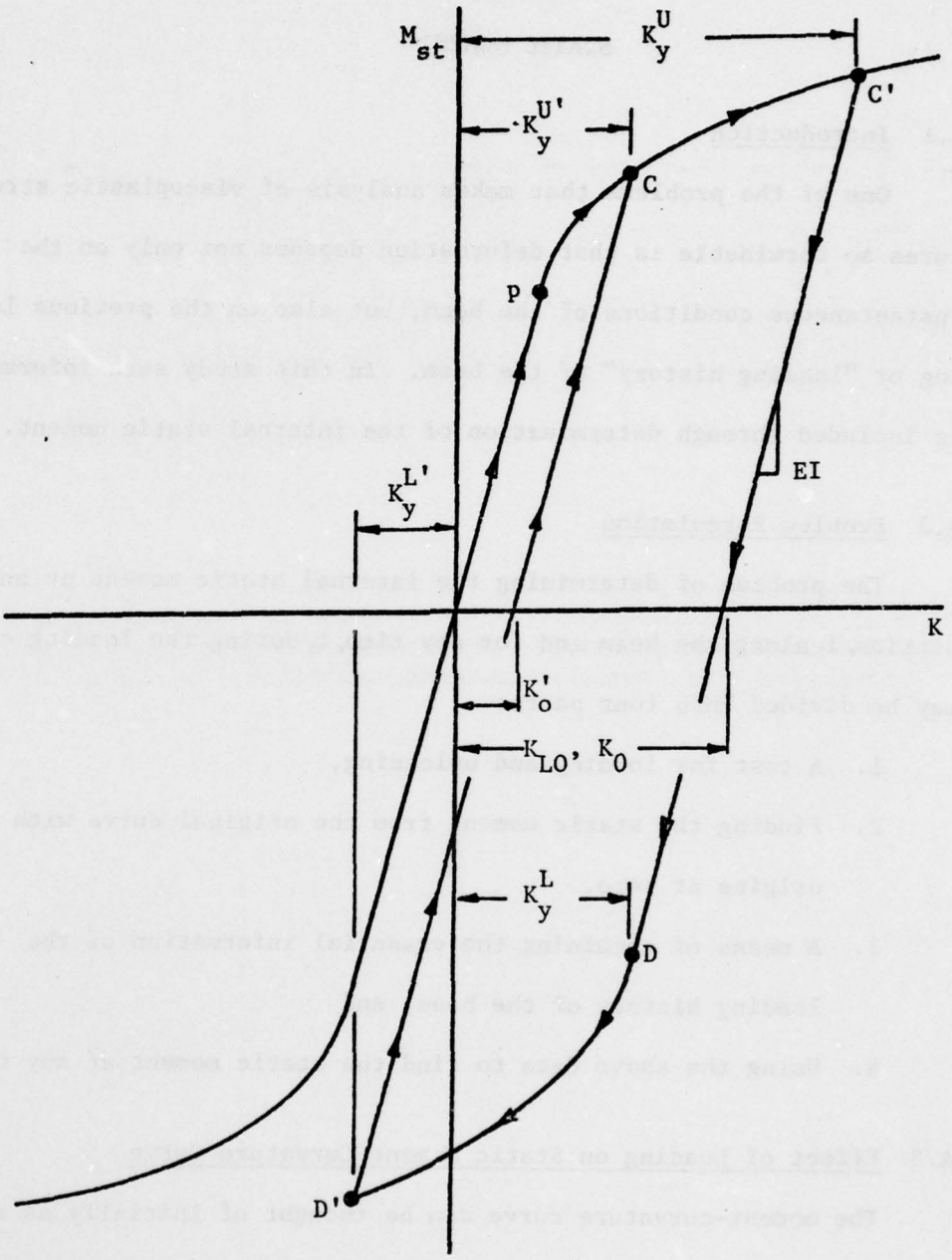

Figure 38. A Loading Cycle Near the Origin

for the upper curve. As the beam is unloaded from point C', the moment curvature relation is a straight line with slope EI and bounded by the lower and upper yield curvatures: K_y^L and K_y^U. The origin of the lower curve is shifted to the right by K_{LO} which is also K_0 in this instance.

If the loading continues past the yield point on the lower curves (point D) to some point D', the permanent curvature is reduced to a new value of K_0'. In addition, a new lower yield point of $K_y^{L'}$ is set and the value of K_y^U is reduced to correspond with point C. The justification for this is as long as a permanent curvature exists, the material will show some strain hardening effects.

A similar shift in the upper curve occurs if the permanent curvature K_0 becomes negative and new yield curvatures K_y^L and K_y^U are set as shown in Figure 39. Notice the lower curve does not

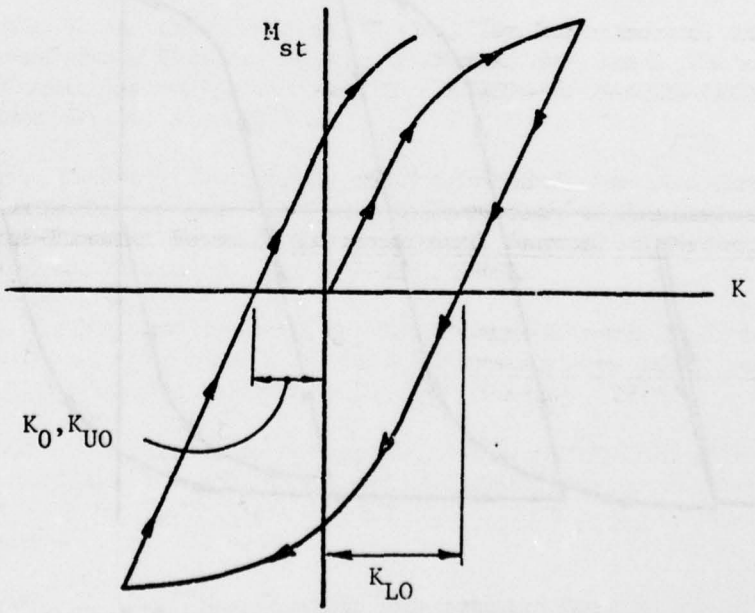

Figure 39. Shift in Upper Curve

change its position when the upper curve is shifted. The origins of the upper and lower curves tend to remain at the extreme values of K_0 achieved during a loading cycle.

$$K_{UO}(t) = \min (K_0) \tag{A.1}$$

$$K_{LO}(t) = \max (K_0) \tag{A.2}$$

Curves presented by Witmer, Wu, and Merlis (25) seem to alter this assumption somewhat. In Figure 40, a schematic of an experimental stress strain relation obtained from repeated loading of a plate shows that the upper and lower curves shift to the current value of K_0. No data were present, however, that show repeated loading around the coordinate origin.

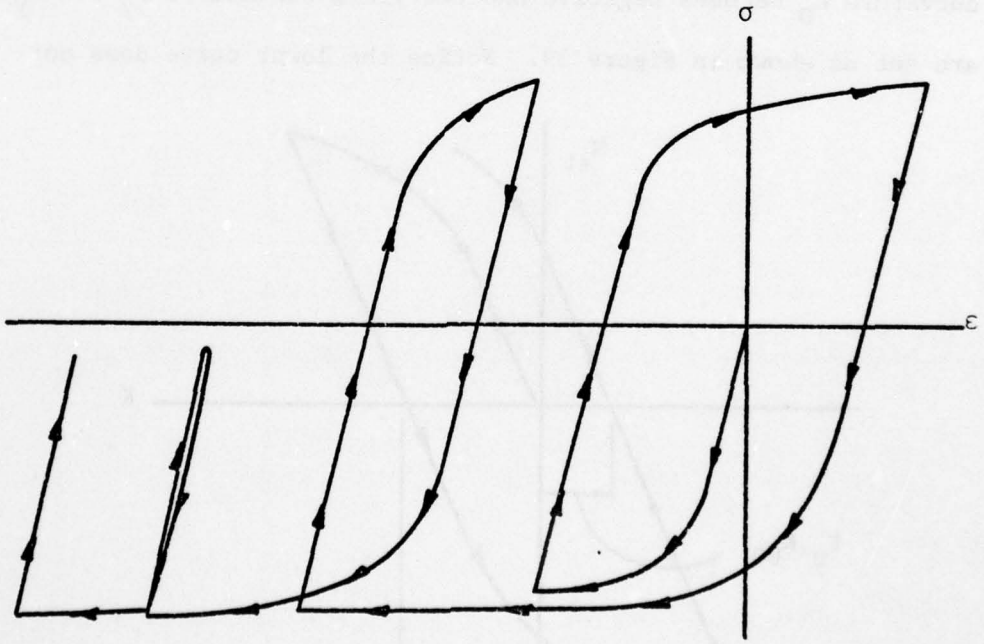

Figure 40. Schematic of Experimental Stress-Strain Loading Cycle

It should be mentioned that this scheme of shifting origins for determining the internal static moment is only an approximate one. Obviously, the Bauschinger effect is neglected along with any low cycle fatigue properties. The results presented by Vogel, however, show good correlation using a similar method for one cycle or less in the elastic-plastic region.

A.4 A Test for Loading

A condition of loading occurs at a point when the magnitude of the internal moment is increased. Since the internal moment is what we seek to find, the curvatures must be used to determine a condition of loading or unloading. Such determination is made through the use of a loading function p(t), defined as

$$p(t) = \frac{K(t) - K_0}{K(t) - K(t - \Delta t)} \qquad (A.3)$$

The sign of the loading function determines the state of a point on the beam.

$$\text{Loading:} \quad p(t) > 0 \qquad (A.4)$$

$$\text{Unloading:} \quad p(t) < 0 \qquad (A.5)$$

The numerator indicates which curve--(+) upper or (-) lower--on which loading occurs and the denominator indicates increasing or decreasing curvature.

For example, consider a condition of loading on the lower curve as shown in Figure 41. The value of curvature is numerically decreasing, i.e.,

$$K(t) - K(t - \Delta t) < 0 \qquad (A.6)$$

and loading occurs on the lower curve where

$$K(t) - K_0 < 0 \qquad (A.7)$$

The test function is therefore positive, indicating the beam is loading.

A.5 Initial Moment Curvature Relation

Because the moment curvature relation only shifts origins during loading, it is useful to define a function g(K) which represents the initial curve. A typical moment curvature curve, shown in Figure 42, can be divided into three parts: a linear (elastic) range, a non-linear (elastic-plastic) range and a linear (elastic-plastic) range.

In order to use this information in a computer program VPBA, a curve fit of m points on the actual curve is necessary. Note, the first point is at the end of region 1 while the last two points are at the beginning and end of region 3.

Regions 1 and 3 are simply linear relations as follows:

$$\text{Region 1:} \quad g(K) = A_1 K \qquad (A.8)$$

where

$$A_1 = EI \qquad (A.9)$$

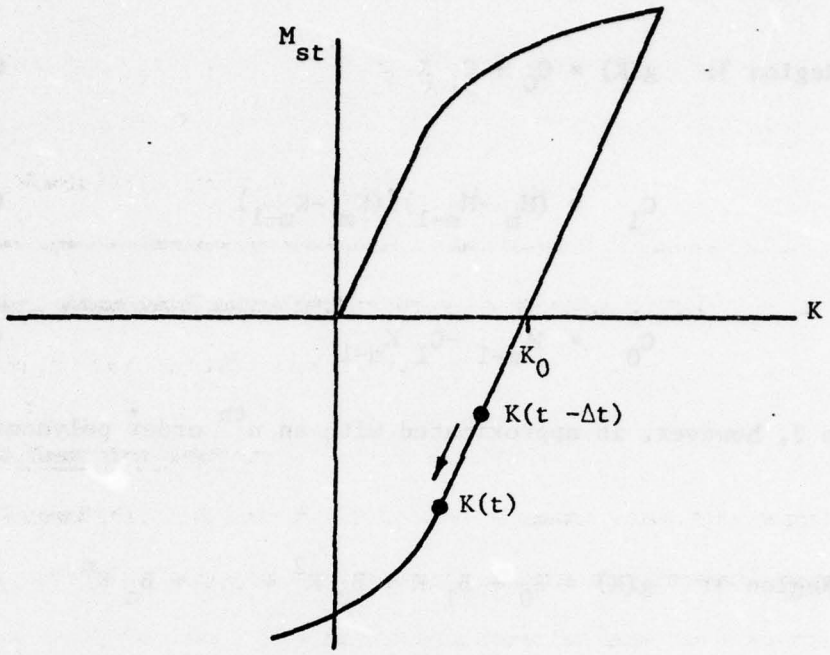

Figure 41. Determination of Loading Function

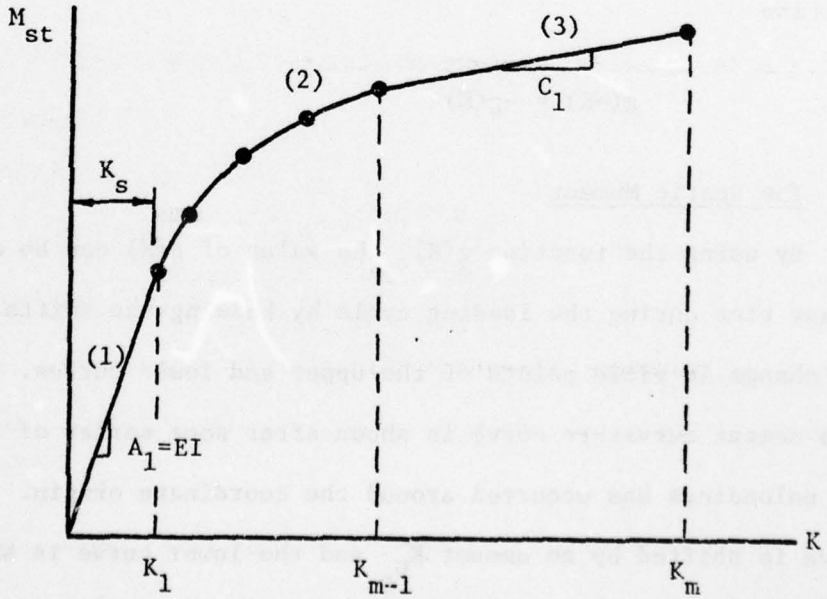

Figure 42. Initial Moment Curvature Curve

$$\text{Region 3:} \quad g(K) = C_0 + C_1 K \tag{A.10}$$

where

$$C_1 = (M_m - M_{m-1})/(K_m - K_{m-1}) \tag{A.11}$$

and

$$C_0 = M_{m-1} - C_1 K_{m-1} \tag{A.12}$$

Region 2, however, is approximated with an n^{th} order polynomial curve fit

$$\text{Region 3:} \quad g(K) = B_0 + B_1 K + B_2 K^2 + \ldots + B_n K^n \tag{A.13}$$

The coefficients B_0, B_1, ..., B_n are determined by the method of least squares.

The complete function g(K) is then given by Equations A.8, A.10, and A.13. For negative values, g(K) is considered an odd function

$$g(-K) = -g(K) \tag{A.14}$$

A.6 The Static Moment

By using the function g(K), the value of g(K) can be obtained at any time during the loading cycle by knowing the shifts in origins and change in yield points of the upper and lower curves. In Figure 43 a moment curvature curve is shown after some series of loadings and unloadings has occurred around the coordinate origin. The upper curve is shifted by an amount K_{U_0} and the lower curve is shifted by K_{L_0}. The elastic line, or line of unloading, is located at K_0 from the coordinate origin.

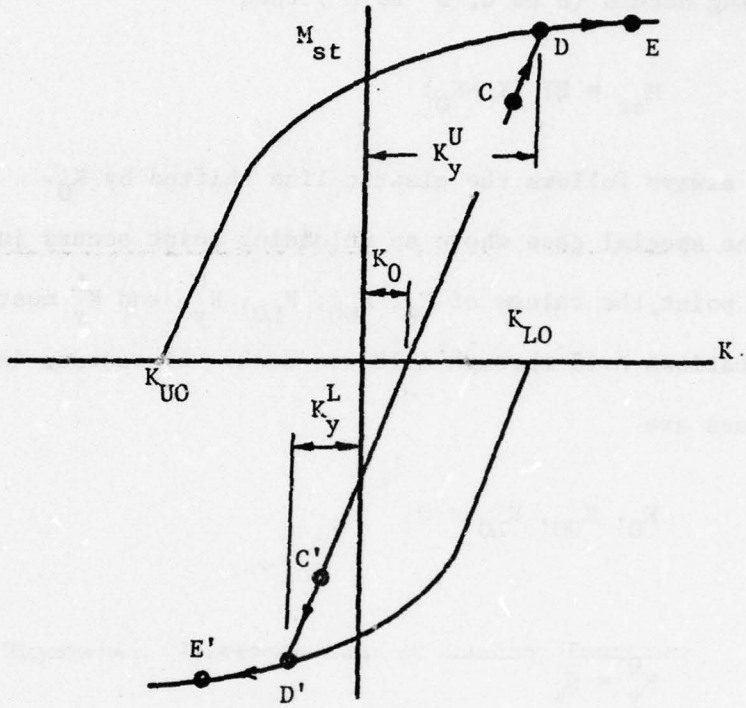

Figure 43. Calculating the Static Moment

First, consider loading in each of the following cases:

(1) The elastic region (C to D, or C' to D')

$$M_{st} = EI\ (K - K_0) \tag{A.15}$$

(2) The upper plastic region (D to E)

$$M_{st} = g(K - K_{UO}) \tag{A.16}$$

(3) The lower plastic region (D' to E')

$$M_{st} = g(K - K_{LO}) \tag{A.17}$$

AD-A053 185 PENNSYLVANIA STATE UNIV UNIVERSITY PARK DEPT OF ENGI--ETC F/G 13/13
SHOCK ANALYSIS OF TUBULAR VISCOPLASTIC BEAMS.(U)
JUL 77 S G GATCHEL, V H NEUBERT N00014-75-C-0759

UNCLASSIFIED NL

2 OF 2
AD
A053185

END
DATE
FILMED
6-78
DDC

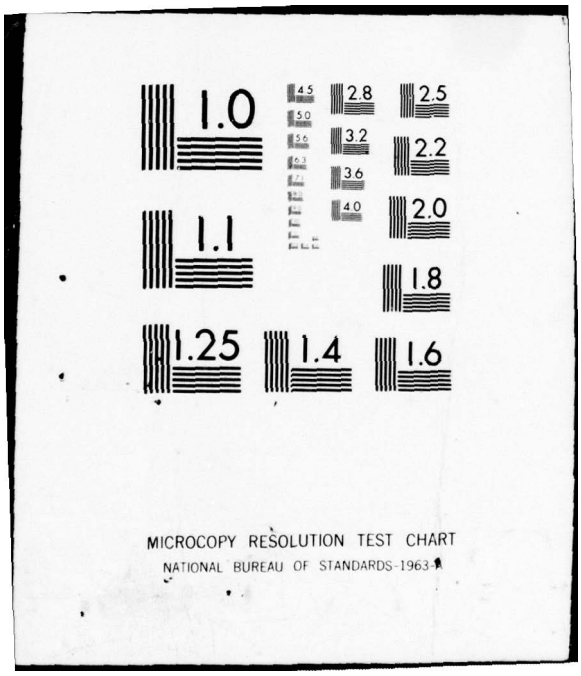
1.0
1.1
1.25
1.4
1.6
1.8
2.0
2.2
2.5
2.8
3.2
3.6
4.0
4.5
5.0
5.6
6.3
MICROCOPY RESOLUTION TEST CHART
NATIONAL BUREAU OF STANDARDS-1963-A

If unloading occurs (D to C, D' to C') then

$$M_{st} = EI\ (K - K_0) \tag{A.18}$$

Unloading always follows the elastic line shifted by K_0.

In the special case where an unloading point occurs just after a loading point, the values of K_0, K_{UO}, K_{LO}, K_y^U, and K_y^L must be reset before Equations A.15 through A.18 are used. Of course, initially these values are

$$K_0,\ K_{UO},\ K_{LO} = 0 \tag{A.19}$$

and

$$K_y^U = K_s \tag{A.20}$$

$$K_y^L = K_s \tag{A.21}$$

where K_s is the initial yield curvature shown in Figure 42.

If unloading begins from the upper plastic region (D to C), the upper yield point is set equal to the last value of curvature. The same is true for unloading from the negative plastic region (D' to C'). From Figure 44, K_0 can be found geometrically from the slope of the elastic line.

$$EI = \frac{g(K_y^U - K_{UO})}{(K_y^U - K_0)} \tag{A.22}$$

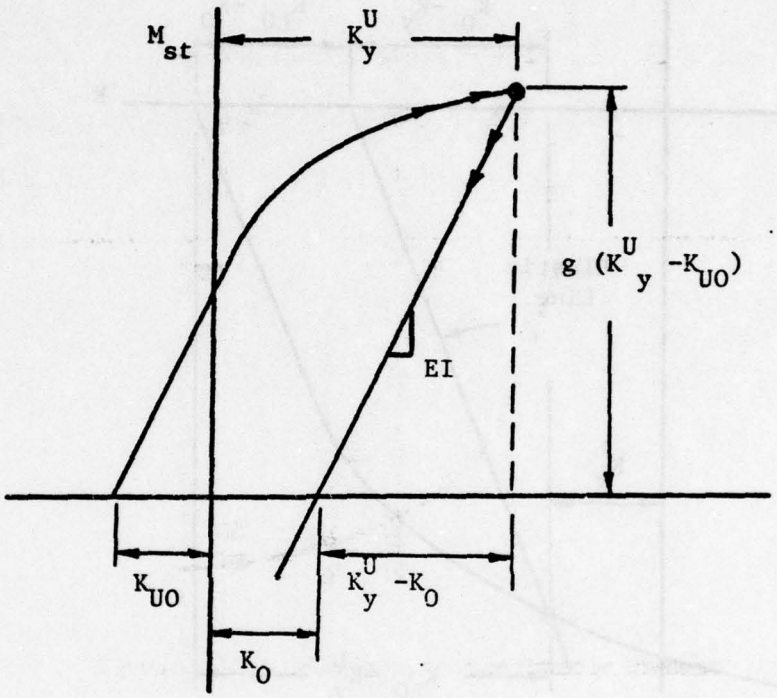

Figure 44. Unloading from the Upper Plastic Region

Solving for K_O

$$K_O = K_y^U - \frac{g(K_y^U - K_{UO})}{EI} \qquad (A.23)$$

When the upper yield point shifts, the lower yield point also changes. K_y^L is found by determining the intersection of the elastic line with the lower curve, as shown in Figure 45. At the intersection the value of M_{st} can be found two ways: from the elastic line

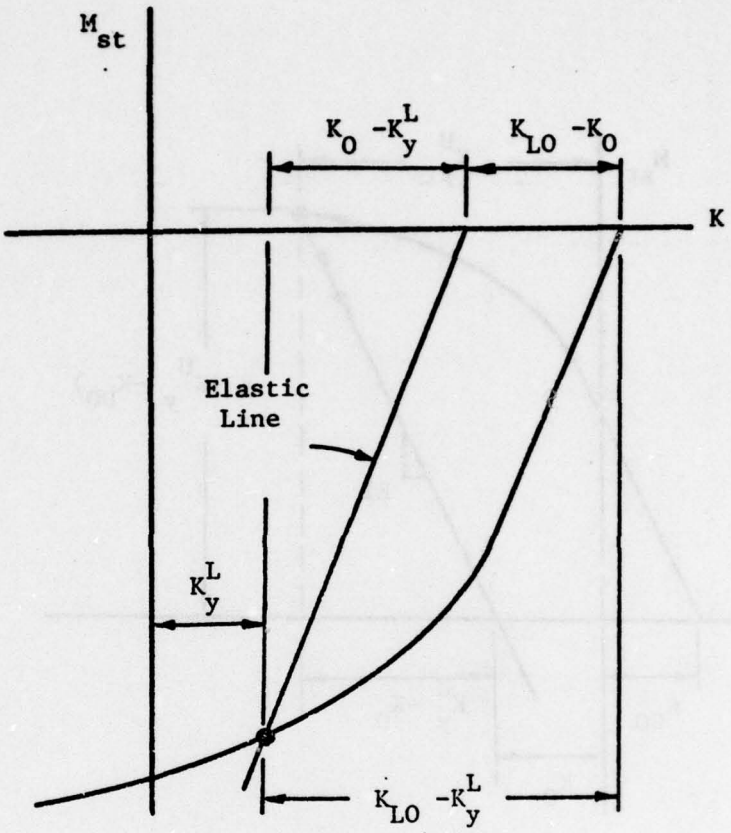

Figure 45. Lower Yield Point

$$M_{st} = (K_0 - K_y^L)\ EI \tag{A.24}$$

and from the function g(K)

$$M_{st} = g(K_{LO} - K_y^L) \tag{A.25}$$

Equating these and solving for

$$K_y^L = K_0 - \frac{g(K_{LO} - K_y^L)}{EI} \tag{A.26}$$

This transcendental equation must be solved iteratively by guessing an initial value for K_y^L. The best initial value is $-K_s$ which is the exact solution during the first cycle. Experience has shown that convergence within one percent of the solution occurs in less than ten iterations.

Equations A.23 and A.26 are concerned with unloading from the upper plastic region. However, if unloading first occurs from the negative plastic region a shift in the upper curve is required. A similar procedure is followed as outlined above, namely, the lower yield point is set equal to the last value of curvature and

$$K_0 = K_y^L - \frac{g(K_y^L - K_{LO})}{EI} \tag{A.27}$$

In Figure 46, the intersection of the elastic line with the upper plastic region is somewhat different. The value of the static moment at K_y^U can be written as

$$M_{st} = (K_y^U - K_0)\ EI \tag{A.28}$$

and

$$M_{st} = g(K_y^U - K_{UO}) \tag{A.29}$$

Equating and solving for K_y^U

$$K_y^U = \frac{g(K_y^U - K_{UO})}{EI} + K_0 \tag{A.30}$$

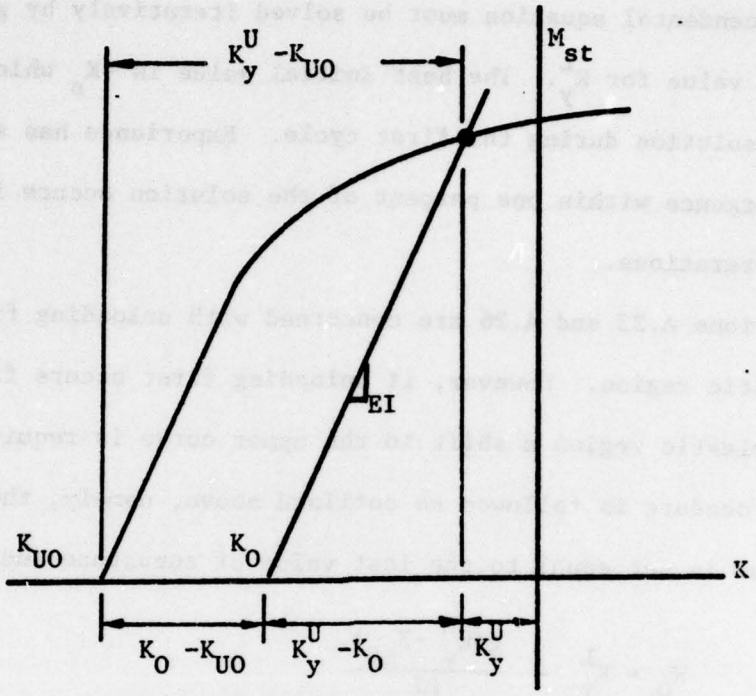

Figure 46. Upper Yield Point

The procedure described above is used in the subroutine MFIND of VPBA. It returns a value of $M_{st_i}(t)$ given a $K_i(t)$ by directing the program to use one of the four equations (A.15, A.16, A.17, or A.18) based on the knowledge of the loading function and the region (elastic, upper plastic, or lower plastic) in which the value of $K_i(t)$ falls. If $K_i(t)$ is an unloading point followed by a loading point, the internal subroutine SHIFT is called to determine new values of K_{UO}, K_{LO}, K_O, K_y^U, and K_y^L before the solution continues. The curve fit described in section A.5 is done before the solution is started in subroutine LEAST. The function g(K) is stored as the subroutine MSTO.

APPENDIX B

MOMENT OF TIP MASS

The rigid element at the tip of the beam necessitates finding the internal moment differently than those in the flexible portion of the beam. The end moment M_n can be written in terms of the internal moments M_{n-1} and M_{n-2} which are known from Equation 2.23 in Chapter 2. A force diagram of the last two elements of the beam are shown in Figure 47. Five equations of motion are written as follows in terms of the s-u coordinate system:

$$V_{n-1} - V_{n-2} = m_{n-1} \ddot{u}_{n-1} \tag{B.1}$$

$$M_{n-2} - M_{n-1} - V_{n-2} \Delta S_{n-2} \cong 0 \tag{B.2}$$

$$M_n - M_{n-1} + V_{n-1} \Delta S_{n-1} \cong 0 \tag{B.3}$$

$$V_{n-1} = -m_n \ddot{u}_n \tag{B.4}$$

$$M_n = -J\ddot{\theta}_n \tag{B.5}$$

The assumptions used for these equations are those outlined in section 2.2 with the addition that the rotational acceleration of the s-u coordinate system is small.

Further kinematical relations can be written as a result of the rigid element.

$$\ddot{\theta}_{n-1} = \ddot{\theta}_n \tag{B.6}$$

and

$$\ddot{u}_n = \ddot{u}_{n-1} + \Delta S_{n-1} \ddot{\theta}_{n-1} \tag{B.7}$$

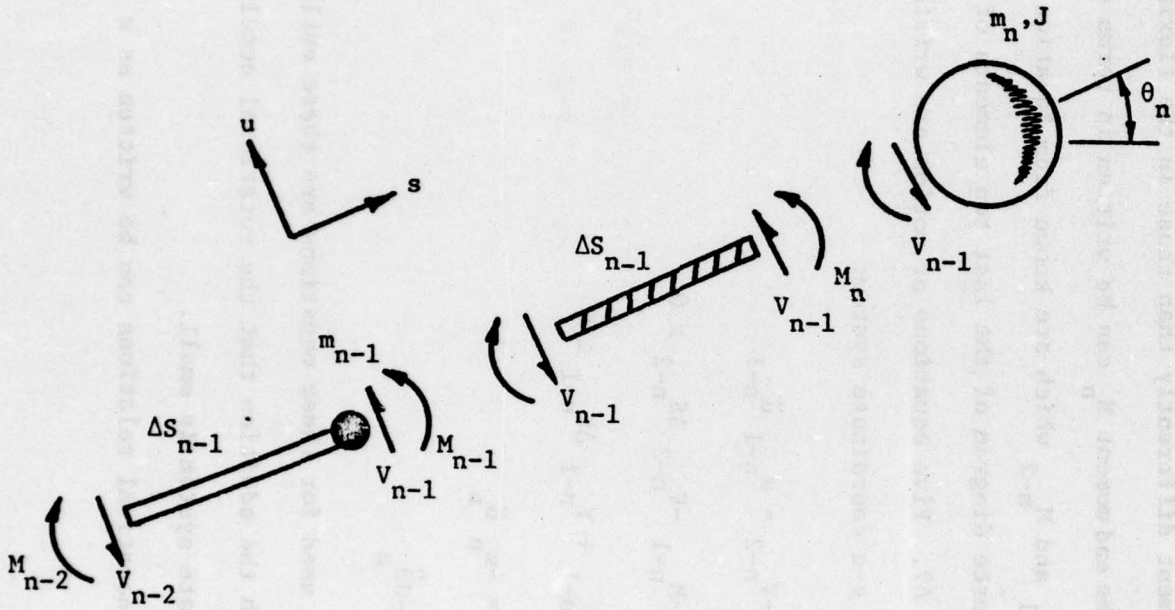

Figure 47. Force Diagram of Beam Tip

combining these,

$$\ddot{u}_n = \ddot{u}_{n-1} + \Delta S_{n-1} \ddot{\theta}_n \tag{B.8}$$

Equations B.1, B.3, B.4, B.5, and B.8 form a set of linear independent equations in terms of the unknowns, V_{n-1}, $\ddot{u}_{n-1}$, M_n, $\ddot{u}_n$, and $\ddot{\theta}_n$, which can be solved for M_n.

First, combine Equations B.5 and B.8 and substitute the result into Equation B.4. Solving this for $\ddot{u}_{n-1}$ gives,

$$\ddot{u}_{n-1} = \Delta S_{n-1} \frac{M_n}{J} - \frac{V_{n-1}}{m_n} \tag{B.9}$$

Substituting Equation B.9 into Equation B.1 and recalling from Equation B.2 that

$$V_{n-2} = \frac{M_{n-2} - M_{n-1}}{\Delta S_{n-2}} \tag{B.10}$$

the following expression for V_{n-1} is obtained.

$$V_{n-1} = \left(1 + \frac{m_{n-1}}{m_n}\right)^{-1} \left(\frac{m_{n-1} \Delta S_{n-1}}{J} M_n + \frac{M_{n-2} - M_{n-1}}{\Delta S_{n-2}}\right) \tag{B.11}$$

Finally, Equations B.11 and B.3 are combined to yield an expression in the unknown moment M_n.

$$M_n = \frac{\left(1 + \frac{m_{n-1}}{m_n} + \frac{\Delta S_{n-1}}{\Delta S_{n-2}}\right) M_{n-1} - \left(\frac{\Delta S_{n-1}}{\Delta S_{n-2}}\right) M_{n-2}}{\left(1 + \frac{m_{n-1}}{m_n} \frac{J_e}{J}\right)} \tag{B.12}$$

where

$$J_e = J + m_n \Delta S_{n-1}^2 \qquad \text{(B-13)}$$

Thus M_n is shown to be a linear combination of the moments at two stations inward from the tip.

APPENDIX C

MOMENT CURVATURE FUNCTION FOR HOLLOW CIRCULAR CROSS SECTIONS

The hollow circular cross section is among an entire class of cross sections having a single discontinuity in geometry and at least one plane of symmetry. Such sections as I-beams, U-channels, box beam, and T-sections are all similar in these respects.

The internal bending moment is determined by assuming plane sections remain plane during plastic deformation and by using the familiar equation,

$$M = \int_A y\, \sigma(y)\, dA \qquad (C.1)$$

Some difficulty occurs in trying to evaluate this integral if the plastic deformation is present because the stress function adds another discontinuity--the proportional limit or yield point. Furthermore, the location of this discontinuity is not stationary on the cross section, but changes with the beam curvature. For this reason, the use of numerical integration is desirable. The computer program MCURVE does this, given the stress-strain function and the dimensions of the cross section.

The stress-strain relation is represented by three separate curves as shown in Figure 48. Regions 1 and 3 are straight lines with slopes E and E', respectively, while region 2 is represented by an n^{th} order polynomial curve fit.

$$\sigma(\varepsilon) = a_0 + a_2\varepsilon + a_3 + \ldots, a_n\varepsilon^n \qquad (C.2)$$

for $\varepsilon_1 < \varepsilon < \varepsilon_{n-1}$

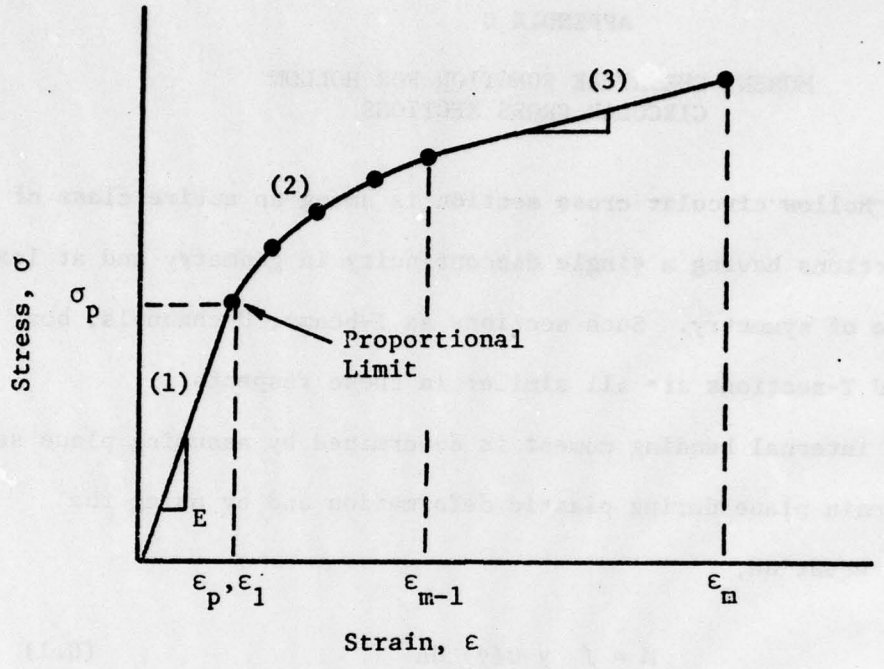

Figure 48. Curve Fit of Stress-Strain Relation

For stress-strain relations that are elastic/perfectly plastic, region 2 is omitted and E' = 0.

The moment on the cross section for a given curvature is found by including in Equation C.1 the geometry of the cross section and the stress-strain function above. Assume the on-set of plastic deformation occurs at some location C above the midplane of the cross section as shown in Figure 49. Because these sections have thick walls to prevent an instability, it is also assumed that no deformation of the cross section occurs, i.e., the ring remains circular. This is verified by Frick's (7) specimens that had less than 1/10 percent eccentricity at the maximum curvature of the beam.

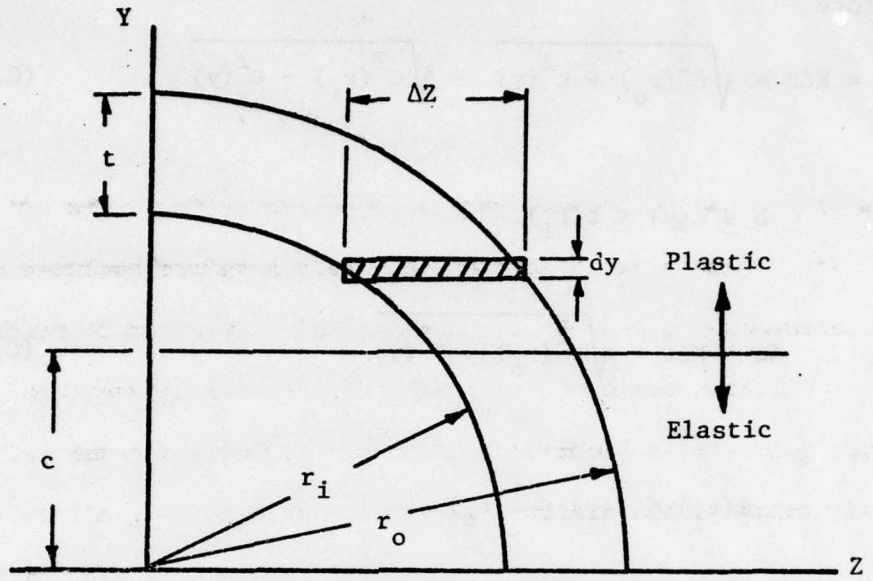

Figure 49. Hollow Circular Cross Section

Substituting for dA, Equation C.1 becomes

$$M = r \int_{A/4} \sigma(\varepsilon)\, y\, \Delta Z\, dy \qquad (C.3)$$

However

$$\Delta Z = \sqrt{r_o^2 - y^2} \quad - \sqrt{r_i^2 - y^2}, \; o \leq y \leq r_i \qquad (C.4)$$

and

$$\Delta Z = \sqrt{r_o^2 - y^2}, \quad r_i < y \leq r_o \qquad (C.5)$$

These relations are made non-dimensional in terms of strain by recalling

$$\varepsilon(y) = K_y \qquad (C.6)$$

Therefore

$$\Delta z = K\Delta Z = \sqrt{\varepsilon^2(r_o) - \varepsilon^2(y)} - \sqrt{\varepsilon^2(r_i) - \varepsilon^2(y)} \qquad (C.7)$$

for

$$o \leq \varepsilon(y) \leq \varepsilon(r_i)$$

and

$$\Delta z = K\Delta Z = \sqrt{\varepsilon^2(r_o) - \varepsilon^2(y)} \qquad (C.8)$$

for

$$\varepsilon(r_i) < \varepsilon(y) \leq \varepsilon(r_o)$$

Substituing these into Equation C.3, and expressing the remaining factors in terms of

$$M = \frac{4\sigma_p}{K^3} \int_o^{\varepsilon(r_o)} \varepsilon\sigma^* (\varepsilon)\, \Delta z\, d\varepsilon \qquad (C.9)$$

where

$$\sigma^* = \frac{\sigma(\varepsilon)}{\sigma_p} \qquad (C.10)$$

The integral can be thought of as a shape factor, Λ, multiplying the constant $4\ \sigma_p/K^3$

$$M = 4\ \sigma_p \frac{\Lambda(\varepsilon)}{K^3} \qquad (C.11)$$

where

$$\Lambda(\varepsilon) = \int_0^{\varepsilon(r_o)} \varepsilon\sigma^* \, (\varepsilon) \, \Delta z \, d\varepsilon \qquad (C.12)$$

The functions Δz and σ^* have discontinuities at $\varepsilon(r_i)$ and $\varepsilon(c)$, respectively.

The location of the yield point on the cross section is determined from the curvature.

$$C = \varepsilon(c)/K = \varepsilon_p/K \qquad (C.13)$$

The cross section first experiences plastic deformation when $c = r_o$. The corresponding curvature is

$$K_o = \varepsilon_p/r_o \qquad (C.14)$$

and

$$M_o = EI \, K_o \qquad (C.15)$$

The computer program MCURVE sweeps the value of curvature beginning with K_0, finds the shape factor Λ, and determines the value of M from Equation C.9. The integral is only separated for the discontinuity at $\varepsilon(r_i)$ because other cross sections such as I-beams offer a "jump-type" discontinuity in the Δz function as shown in Figure 50, causing numerical problems in the integration.

$$\Delta z = \begin{cases} Kdw & \text{for } 0 \leq \varepsilon(y) \leq \varepsilon(r_i) \\ Kdf & \text{for } \varepsilon(r_i) < \varepsilon(y) \leq \varepsilon(r_o) \end{cases} \qquad (C.16)$$

The discontinuity in the stress function is merely integrated through using Simpson's Rule.

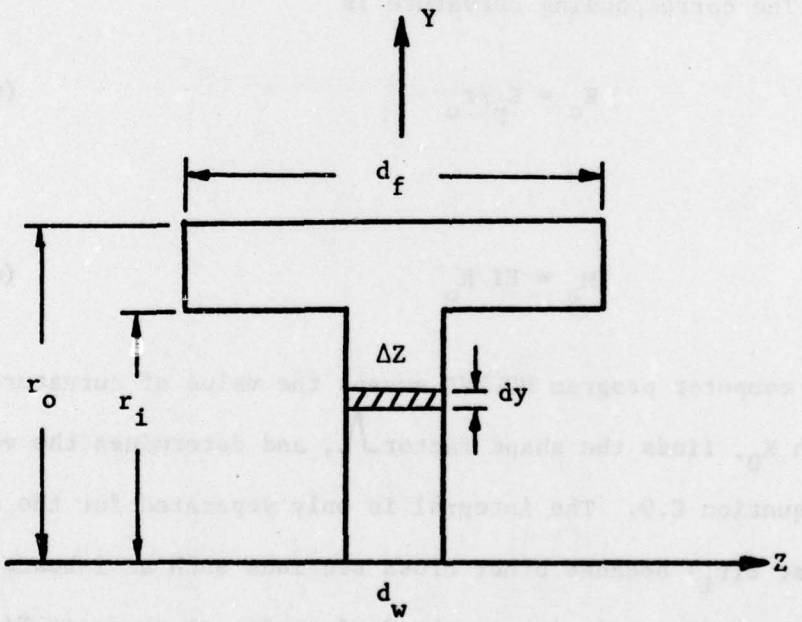

Figure 50. I-Beam Cross Section

Appendix D, Computer Listings are given in reference [28], but are not included in this report.

Distribution List

	Copies
Director Defense Nuclear Agency Attn: SPSS, Dr. E. Sevin Attn: SPSS, Lt. R. Wade Washington, D.C. 20305	1
Commander Naval Ship Engineering Center Code 6105D, Attn: J. Sullivan Washington, D.C. 20360	5
Director Naval Research Laboratory Attn: Code 8400 Code 8404 Code 8406 Code 8440 Code 2627 Washington, D.C. 20375	 1 10 1 2 2
Chief of Naval Research Attn: Code 102IP Department of the Navy Arlington, VA 22217	2
Office of Naval Research Resident Representative Carnegie-Mellon University Room 407, Margaret Morrison Bldg. Pittsburgh, Pennsylvania 15213	2
Defense Documentation Center Cameron Station Alexandria, Virginia 22314 Attn: TIDPR TC	 2 2
Commander Naval Sea Systems Command Code 0351 Code 0372 Department of the Navy Washington, D.C. 20362	2
Chief of Naval Research Attn: Code 222 (Dr. A. Sykes) Code 474 (Dr. N. Perrone) Department of the Navy Arlington, VA 22200	1

	Copies
National Science Foundation 1800 G Street Washington, D.C. 20036	1
Commander Naval Ship Research and Development Center Attn: Code 17 Code 172 Code 174 Bethesda, Maryland 20034	1 1 1 1
Commanding Officer Naval Ship Research and Development Center Attn: Dr. Y. Wang Annapolis, Maryland 21402	1
Officer in Charge Naval Ship Research and Development Center Attn: Dr. E. Palmer Underwater Explosions Research Div. Portsmouth, Virginia 23709	2
Commander Naval Ocean Systems Center San Diego, California 92152	1
Commander Naval Surface Weapons Center Wite Oak Silver Spring, Maryland 20910	1
Commander Naval Sea Systems Command Headquarters Attn: Code 08, R. Cook Department of the Navy Washington, D.C. 20362	1
National Aeronautics and Space Administration Goddard Space Flight Center Attn: F. On Washington, D.C. 20771	1

Distribution List

	Copies
Supervisor of Shipbuilding Conversion and Repair, USN Third Naval District Third Avenue and 29th Street Brooklyn, New York 11232	5
General Dynamics Corporation Electric Boat Division Attn: Dr. L. H. Chen Groton, Connecticut 06304	1
NKF Engineering Associates, Inc. Attn: Dr. R. O. Belsheim 8720 Georgia Avenue Silver Spring, MD 20910	1